Politecnico di Torino

Corso di Laurea Magistrale in Ingegneria Aerospaziale

A.a. 2024/2025

Tesi di Laurea Magistrale

Numerical implementation of Lower Body Negative Pressure in a multiscale mathematical model of the cardiovascular system

Supervisor
Stefania Scarsoglio

Student
Beatrice Sicca 312067

Co-Supervisors
Luca Ridolfi
Francesco Tripoli

Contents

Introduction

A transition from the Earth's gravity to the extraterrestrial microgravity environment causes direct and significant changes to human cardiovascular hemodynamics. Due to the absence of the gravitational pull, a redistribution of body fluids occurs between the upper and lower body. The fluid shift is linked with the changes of cardiovascular functions, for example, reductions in arterial pressure, variations in vascular volumes, and remodeling of carotid baroreflex system. These adaptations may lead to discomfort and even diseases, such as orthostatic intolerance, impaired vision, and intracranial hypertension, during space missions and upon reentry to Earth.

The study of all these challenges related to the manned spaceflight brought to the development of new scientific disciplines known as space medicine and bioastronautics. The main objective of such branches of life sciences is to ensure human survival and well-being during and after missions into space, putting in place a set of pre-flight, in-flight and post-flight countermeasures to fight and prevent from major risks connected to human permanence in the space environment. Among these countermeasures, one of the most extensively studied is the Lower Body Negative Pressure (LBNP), a device that induces blood pooling in the legs and reduces venous return to the heart by causing a depression in the lower parts of the body.

Earth-based experiments, including parabolic flights, prolonged bed rest, or head-down tilt tests, have been performed to better understand the physiology and effective countermeasures. These tests, however, are typically expensive and need long-term involvements of human subjects. Computer models, built upon physiological data, can serve as a cost-effective and non-invasive alternative approach to investigate the dynamic responses of human physiological mechanisms and provide insights to unforeseen health problems related to microgravity in space.

In this thesis, we propose a novel multiscale, 1D-0D closed-loop mathematical model of the human circulation, encompassing the large arteries of the arterial tree departing and branching out from the human aorta, down to downstream arterioles, capillary and venules representing the peripheral microcirculation, including also large veins and venae cavae of the venous return circuit. In addition, the model accounts for a mathematical description of the four contractile cardiac chambers, the arterial and venous pulmonary circulation, a specific and detailed scheme of the cerebrovascular circulation, and the ocular compartment. The model is then integrated with autonomic regulation control mechanisms, such as a baroreflex control, a cardiopulmonary reflex control, and a cerebral autoregulation mechanism for the maintenance of the overall homeostasis of the system under a number of different working conditions (i.e., changes in posture, altered gravity).

The aim of this study is to integrate the effect of the Lower Body Negative Pressure in this numerical model of the cardiovascular system. The contents of the thesis are organized as follows.

Chapter 1 is devoted to introducing the human cardiovascular physiology and functioning, providing a brief summary of the most important cardiovascular system functions, components and roles. Chapter 2 investigates the main effects of the gravity on the human cardiovascular physiology. Then, Chapter 3 presents the mathematical model built to simulate the response of the cardiovascular system to change of posture and of gravitational environment. Following, Chapter 4 explains how the Lower Body Negative Pressure device works, focusing on the main effects that it causes on the human hemodynamics and on the numerical implementation of the device inside the mathematical model. Chapters 5 is devoted to explain which numerical tests have been performed to select the best numerical strategy. Chapter 6 presents the results of the numerical investigations, compares them to other studies and to the body response to a HUT test. Finally Chapter 6.2.4 presents the conclusions of this study.
As the use of computer models presents opportunities to investigate the interaction of a multitude of responses and to vary physiological properties and operating conditions in a strictly controlled manner, this thesis aims to extend the well validated 0D-1D mathematical model to encompass the effects of the LBNP, in order to push further the limit of computational development in the space medicine field.

Chapter 1

Fundamentals of cardiovascular system physiology

The cardiovascular system could be thought as an hydraulic system, consisting of a pump, which is the heart, several distributing and collecting tubes, i.e. the blood vessels, a medium that flows inside those vessels, the blood, and a dense net of small ducts that reach every cells of our tissues, the capillaries. This hydraulic system has also a regulation mechanism that ensures the correct level of blood pressure and the normal distribution of blood flow, fluids and hormones.
The primary objective of this complex system is to deliver oxygen and nutrients to and remove wastes from body cells. In particular, oxygen and nutrients need to be transported to tissues by the blood, while carbon dioxide must be removed. To accomplish this task, two different circulations depart from the heart: the systemic and pulmonary circuits. Each of them consists of a venous system and an arterial system.
In this opening chapter, we will present the main actors of this complex system and their functioning principles, in order to understand the mechanism of blood motion through blood vessels and how it is regulated under different working conditions and stimuli.

1.1 Heart and cardiac cycle

The driving force behind the intricate cardiovascular system is the heart, which functions as a pump by contracting to propel blood through the vessels. Beating approximately 100,000 times per day, it plays a pivotal role in maintaining hemodynamic stability.
Structurally, the heart resembles a pinecone, being relatively broad at its superior surface, referred to as the base, and tapering toward its inferior point, known as the apex. Anatomically, it is divided into two sides (Fig. 1.1), left and right, separated by a septum. Each side consists of two chambers: an atrium and a ventricle, amounting to a total of four cardiac chambers. The upper chambers, the right and left atria, primarily function as receiving chambers, subsequently directing blood into the lower chambers, the right and left ventricles. The ventricles, in turn, serve as the principal pumping chambers, driving blood either to the lungs or to the systemic circulation.

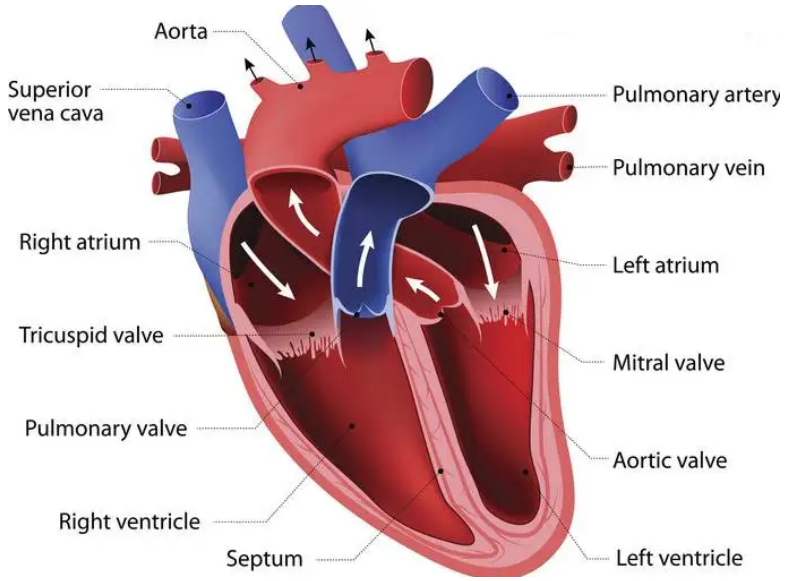

Figure 1.1: Heart anatomy

The heart wall consists of three layers of varying thickness. The contraction of the middle layer, the myocardium—which is the thickest—facilitates the pumping of blood through the heart and into the major arteries.

The interatrial septum separates the two atria (Fig. 1.1), while the atrioventricular septum lies between the atria and the ventricles. The atrioventricular septum features four openings, allowing blood to pass from the atria to the ventricles and from the ventricles to the pulmonary trunk and aorta. Each of these openings contains a valve, a specialized structure ensuring unidirectional blood flow. The valves situated between the atria and ventricles are collectively referred to as atrioventricular valves. In contrast, the valves located at the openings leading to the pulmonary trunk and aorta are known as semilunar valves. Specifically, the mitral valve, positioned between the left atrium (LA) and the left ventricle (LV), is a bicuspid valve with two overlapping leaflets. The tricuspid valve, located between the right atrium (RA) and the right ventricle (RV), has three leaflets. The semilunar valves consist of the aortic valve, situated between the left ventricle and the aorta, and the pulmonary valve, positioned between the right ventricle and the pulmonary artery. Each valve's leaflets (two in the mitral valve, three in the others) overlap during closure to prevent retrograde blood flow. The operation of these valves is entirely governed by fluid dynamics. When the pressure in the upstream chamber exceeds the pressure in the downstream chamber or vessel, the valve opens to allow blood flow; otherwise, it remains closed.

As mentioned above, the function of the heart is to pump blood inside the vessel. To accomplish this task, the heart alternately contracts and relaxes throughout the lifetime of an individual. The period of time that begins with contraction of the atria and ends with ventricular relaxation is known as the cardiac cycle. The period of contraction that the heart undergoes while it pumps blood into circulation is called systole. The period of relaxation that occurs as the chambers fill with blood is called diastole. Both the atria and the ventricles undergo systole and diastole, and it is essential that these components are carefully regulated and coordinated to ensure that blood is efficiently pumped into the body.

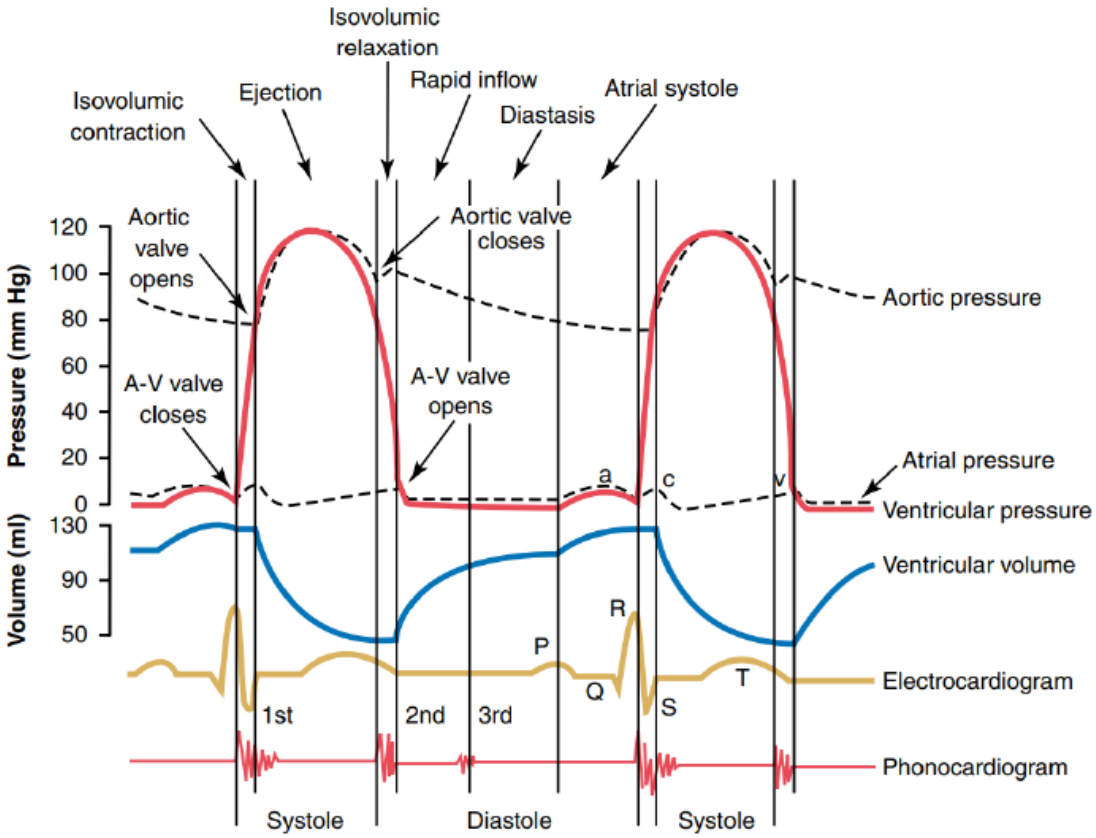

Figure 1.2: Wiggers diagram [1].

For the sake of simplicity we focus now on the left part of the heart, remembering that the right one works in the same way. At the beginning of the systole, both the mitral and the aortic valve are closed making the left ventricle isolated and filled with blood. The first part of the systole consists of an isovolumic contraction, where blood volume contained doesn't change and LV pressure rises due to the contraction of the chamber. Just prior to ventricular contraction, the ventricles contain approximately 130 ml blood in a resting adult in a standing position. This volume is known as the end diastolic volume (V_{lved}) or preload and is maintained over the phase of isovolumic contraction.. When the pressure in the left ventricle exceeds the level in the aortic root, the second part of the systole begins with the opening of the aortic valve and the ejection of the blood into the aorta. Pressure in the ventricle keeps rising for the initial phase of the ejection, and than it decreases due to the chamber emptying. Both ventricles pump the same amount of blood. This quantity is referred to as stroke volume. Stroke volume will normally be in the range of 70–80 ml. Since ventricular systole began with an V_{lved} of approximately 130 ml of blood, this means that there is still 50–60 ml of blood remaining in the ventricle following contraction. This volume of blood is known as the end systolic volume (V_{lves}). When pressure in LV falls below the level in aorta, aortic valve closes to prevent blood from flowing backward. The closing of the aortic valve represents the end of systole and the beginning of diastole. Also the diastole is divided in two phases, the first one is an isovolumic relaxation followed by the filling of the left ventricle. During isovolumic relaxation, both mitral and aortic valve are

closed, ventricle is isolated and contains less blood compared to the beginning of systole due to ejection. During this phase, LV volume doesn't change, while the chamber relaxes, lowering the pressure inside. When the pressure in the LV falls below the level of the left atrium, the second phase of diastole begins with the opening of the mitral valve and the filling of the left ventricle. During filling, pressure inside left ventricle is lower than that in the right atrium, promoting fluid dynamic filling of ventricle. Approximately 70–80% of ventricular filling occurs by this method. The remaining 20–30% of filling is due to atrial contraction, also referred to as the "atrial kick". As the atrial muscles contract from the superior portion of the atria toward the atrioventricular septum, pressure rises within the atria and blood is pumped into the ventricles through the open mitral valve. Atrial systole lasts approximately 100 ms and ends prior to ventricular systole, as the atrial muscle returns to diastole. When the ventricle is filled, its pressure becomes lightly higher than that in the atrium and so mitral valve closes ending diastole. Now the cycle can restart with the isovolumic contraction of the systole.
In Fig.1.2 we can see a graph representing left ventricular pressure, aortic pressure and left atrium pressure. The atrial kick is also clearly visible, represented by an increase in atrial pressure during the filling phase (denoted by the letter "a"). In the lower part of the diagram, blood volume inside left ventricle is reported. This illustration is called Wiggers diagram and reports how pressure and volume change during a cardiac cycle.

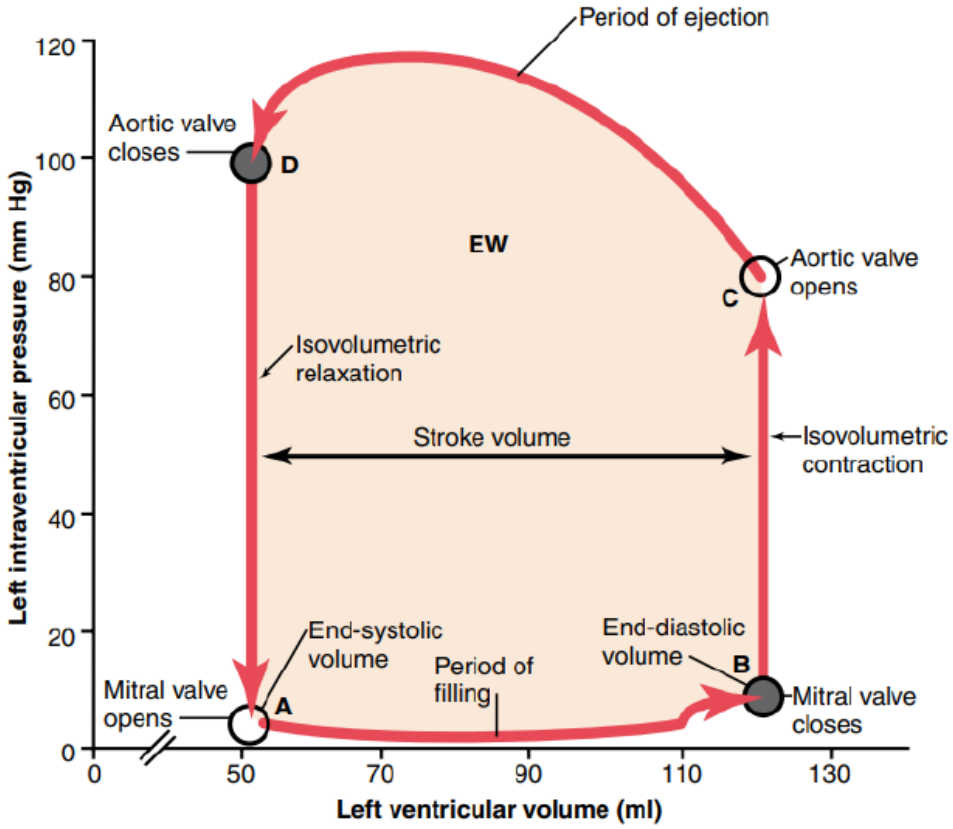

Figure 1.3: PV loop [1]

Another significant representation of the cardiac cycle is the so-called PV loop (Fig. 1.3). This diagram plots the volume of blood in the left ventricle on the x-axis and the pressure on the y-axis. Starting from the onset of systole, the loop begins at the lower right corner (point B). At this point, both the mitral and aortic valves are closed. Along the segment B-C, isovolumetric contraction occurs, increasing the pressure in the left ventricle to approximately 80 mmHg. This is followed by the opening of the aortic valve and the ejection phase (C-D). During this phase, the ventricular volume decreases from approximately 120–130 ml to 50 ml. Subsequently, diastole begins with the valves closed, characterized by isovolumetric relaxation (D-A), which is followed by the filling phase (A-B).
To quantitatively describe the events occurring during a cardiac cycle, several key variables have been defined:

1. **Heart rate (HR)**: The number of cardiac cycles occurring in one minute, expressed in beats per minute (bpm).

2. **Stroke volume (SV)**: The difference between the end-diastolic volume (V_{LVED}) and the end-systolic volume (V_{LVES}), representing the amount of blood ejected during a single heartbeat [ml/beat]:
$$SV = V_{LVED} - V_{LVES} \tag{1.1}$$

3. **Cardiac output (CO)**: The product of stroke volume and heart rate, defined as:
$$CO = SV \cdot HR \tag{1.2}$$
This represents the blood flow output from the heart, expressed in liters per minute.

4. **Ejection fraction (EF)**: An index of cardiac efficiency, defined as the ratio of the blood ejected per beat (SV) to the total potentially ejectable volume (V_{LVED}):
$$EF = \frac{SV}{V_{LVED}} \tag{1.3}$$
A lower value indicates higher cardiac efficiency.

5. **External (stroke) work (EW)**: The work performed by the heart during each beat. Measured in Joules, it is calculated as the area enclosed by the PV loop:
$$EW = \oint_{\mathcal{C}} P\,dV \tag{1.4}$$

For a healthy young adult at rest, reference values are typically HR = 75 bpm, SV = 70-80 ml/beat, CO = 5-6 l/min, EF = 50-65%, and EW = 0.5-1.5 J.
Another important hemodynamic parameter related to the heart functioning is the elastance E. It is defined as the ratio between the pressure inside a cardiac chamber ΔP and the volume contained ΔV. It represents the contractility of the heart, its stiffness.

1.2 Systemic and pulmonary circulations

Blood is carried through the body via blood vessels which can be of two different types: artery and vein. An artery is a blood vessel that carries blood away from the heart, where it branches into ever-smaller vessels. Eventually, the smallest arteries, vessels called arterioles, further branch into tiny capillaries, where nutrients and wastes are exchanged with the cells of the tissues, and then combine with other vessels that exit capillaries to form venules, small blood vessels that carry blood to a vein, a larger blood vessel that returns blood to the heart.
Arteries and veins transport blood in two distinct circuits (Fig. 1.4): the systemic circuit and the pulmonary circuit. Systemic arteries provide blood rich in oxygen to the tissues of the body. At the cell tissues level an important exchange takes place: the oxygen, carried by the emoglobine in the blood, is released to the tissue, while the latter yields to deoxygenated blood the waist of the cellular activity. The blood that returns to the heart through systemic veins has less oxygen, since much of the oxygen carried by the arteries has been delivered to the cells. In contrast, in the pulmonary circuit, arteries carry blood low in oxygen exclusively to the lungs for the reverse gas exchange. Oxygen flows towards the intra-vascular space, while carbon dioxide is transferred outside and then expelled by expiration. New oxygenated blood flows then through pulmonary veins back to the left part of the heart to be pumped back into systemic circulation, providing thus the energy supply for the entire organisms.
To summarise, the systemic circulation departs from the left part of the heart with the aorta, brings nutrients and removes toxins from cells even far away from the heart, closing the circulation at the right part of the heart via the venae cavae. On the other hand, the pulmonary circuit is limited to the region around the heart and is devoted to expel the carbon dioxide and recharge the blood with clean oxygen. It departs from the right part of the heart via pulmonary artery, and ends in the left one, via pulmonary vein.
The difference in the dimensions of the two circuits is the cause of the different distribution of blood: only 9% in the pulmonary circulation (also called the lesser circulation) against 84% in the systemic one (also called the greater circulation). Systemic veins and venules, instead, contain up to 64% of total blood volume, as venous vessels are considered to be good blood reservoirs thank to their highly compliant properties. Another point of difference is the pressure: the systemic circulation requires higher level of pressure to reach all the peripheral districts (80 mmHg to 120 mmHg), whereas the lesser circulation needs less push (10 mmHg to 30 mmHg) to deliver blood to the nearer lungs.

1.3 Arterial and venous systems

As previously mentioned, the arterial and venous systems are both integral components of the cardiovascular hydraulic system, but they perform distinct functions: the former delivers blood to the tissues, while the latter returns blood to the heart and serves as a reservoir for large volumes of fluid. Given the differing roles of these two systems, the mechanical properties of their vessels are likewise distinct.

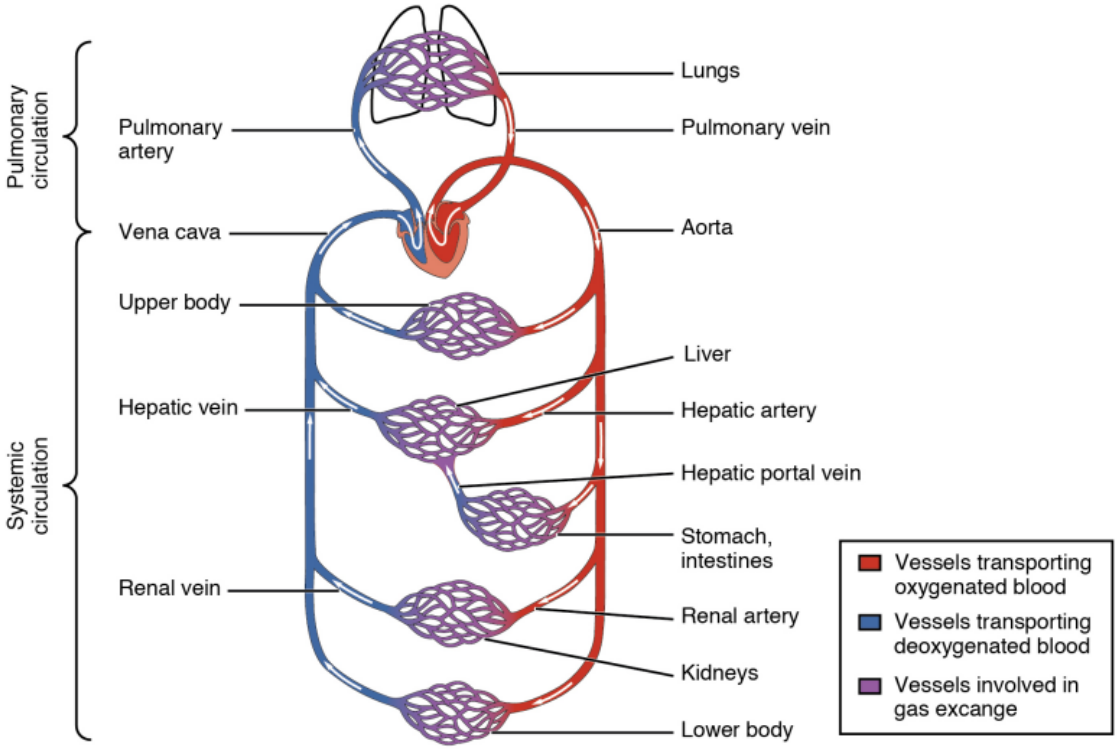

Figure 1.4: Cardiovascular Circulation: the pulmonary circuit moves blood from the right side of the heart to the lungs and back to the heart. The systemic circuit moves blood from the left side of the heart to the head and body and returns it to the right side of the heart to repeat the cycle. The arrows indicate the direction of blood flow, and the colors show the relative levels of oxygen concentration [2].

1.3.1 Arterial system

The arterial system consists of large arteries, followed by smaller arteries, which branch into arterioles and ultimately into capillaries. These capillaries reach the cells of various tissues for systemic circulation and envelop the pulmonary alveoli at the level of pulmonary circulation. The pressure within these vessels varies depending on the type of circulation — systemic circulation is characterized by higher pressures compared to pulmonary circulation, as it must propel blood to peripheral regions of the body — and the distance of the vessel from the heart. The heart, in fact, pumps blood cyclically, generating a pulsatile driving pressure that varies over time. In arteries close to the heart, such as the aorta or the pulmonary artery, internal pressure is highly pulsatile, fluctuating between a maximum (systolic pressure, which reflects arterial pressure resulting from blood ejection) and a minimum (diastolic pressure, which represents arterial pressure during ventricular relaxation) with each heartbeat. As blood moves toward the capillaries, the heart's pumping effect becomes less perceptible, and this pulsatility gradually diminishes. This transition to a continuous pressure is also associated with an important property of arterial vessels: resistance. Resistance is defined as the vessel's ability to oppose blood flow and is particularly high in small arteries and arterioles, leading to a significant drop in mean intraluminal pressure as well as the attenuation of pulsatility.

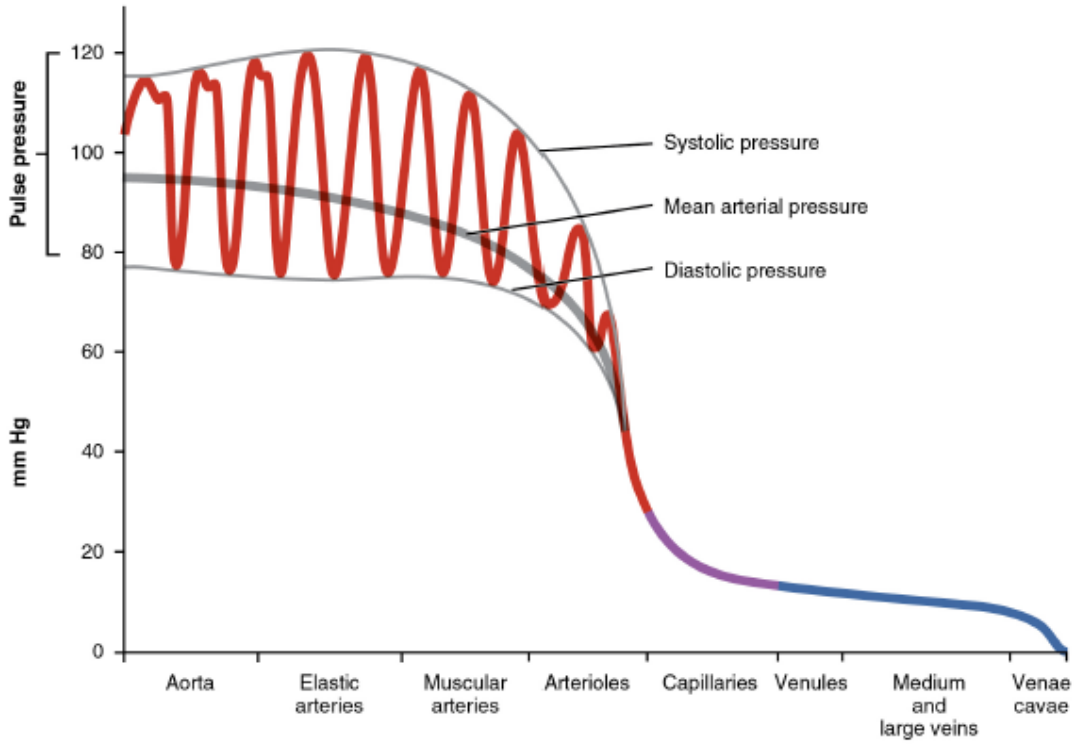

Figure 1.5: Intraluminal pressure along the systemic and pulmonary circulations [2].

Observing the pressure profile along the two circulatory systems (Fig. 1.5), it is evident that the mean driving pressure at the level of the aorta and large arteries is approximately 100 mmHg, with pronounced pulsatility (80–120 mmHg). In the small arteries, and especially in the arterioles, there is a significant pressure drop due to the high resistance of these vessels, reaching 20–25 mmHg at the level of systemic capillaries. At this point, pulsatility is completely eliminated to ensure a slow and continuous blood flow, and thus nutrient delivery, to the tissues. In the pulmonary circulation, a similar pressure drop and elimination of pulsatility occur at the level of the arterioles. However, the pressures involved here are lower due to the reduced force required to reach the alveoli: pressure decreases from 10–30 mmHg in the pulmonary artery to approximately 10 mmHg in the capillaries.
The intraluminal pressure is the sum of three distinct contributions: the dynamic pressure generated by the pumping action of the heart, the viscoelastic component associated with the mechanical properties of the vessel walls, and the hydrostatic component, which depends on the posture of the subject and the specific weight of the blood. The component related to the pulsation of the heart is the predominant one, which, as previously mentioned, results in large arteries exhibiting not only pulsatile pressure but also pulsatile flow rate and velocity. Regarding the velocity profile of blood in different vessels, it is strongly influenced by the flow regime, whether laminar or turbulent, stationary or pulsatile. Specifically, in large arteries, inertial effects dominate over viscous effects, resulting in a flat velocity profile and confining boundary layer effects to a thin region near the vessel wall. Conversely, starting from the arterioles, viscosity begins to counterbalance inertial forces, causing the velocity profile to adopt the characteristic parabolic shape described by the law of Poiseuille. Through this law, it is

possible to mathematically define resistance (R) as the ratio between flow rate (Q) and the pressure drop across the vessel segment considered (ΔP).

$$R = \frac{\Delta P}{Q} = \frac{8\mu L}{\pi r_i^4} \tag{1.5}$$

where L is the length of the vessel, μ is the dynamic viscosity and r_i the internal radius of the conduit.
By examining this equation, you can see that since the radius can be changed rapidly by vasoconstriction and vasodilation, thus small changes in the radius will greatly affect the property of the vessel (resistance) and the flow.

1.3.2 Venous system

The venous system receives blood (deoxygenated in the systemic circulation and oxygenated in the pulmonary circulation) from tissues or alveoli at the level of venules, the smallest vessels, which then converge to form larger vessels, the veins. These veins merge into increasingly larger veins, culminating in the superior and inferior vena cava for the systemic circulation, which drain into the right atrium, and the pulmonary veins for the pulmonary circulation, which carry oxygenated blood to the left atrium.
The venous system holds approximately 65–70% of the total blood volume, thereby functioning as a reservoir. To efficiently fulfill this role, venules and veins are characterized by high compliance. This property is defined as the ability of any compartment to expand to accommodate increased content. The greater the compliance of a vessel, the more effectively it can expand to accommodate surges in blood flow without significantly increasing resistance or blood pressure [2]. Veins exhibit greater compliance than arteries and are capable of expanding to hold larger volumes of blood.
From a mathematical perspective, compliance C is defined as the ratio between the volume accommodated by the vessel ΔV and the internal pressure ΔP [ml/mmHg] (as opposed to cardiac elastance E):

$$C = \frac{\Delta V}{\Delta P} \tag{1.6}$$

In general, the relationship between pressure and volume is not constant (non-linear compliance). A vessel with high compliance can thus accommodate a large amount of blood, maintaining almost constant internal pressure.
Veins are characterized by high distensibility and low resistance, which results in low pressure, absence of pulsatility (except in the vena cava due to retrograde pulsatility from the heart), and a very small pressure drop from the peripheral regions to the atrium. However, a pressure gradient is still necessary to facilitate venous return, even in an upright position, where the hydrostatic gradient tends to discourage return. This is made possible by the low pressure in the atrium (close to zero during diastole) and a slightly higher pressure along the veins (5-10 mmHg). Furthermore, two additional factors are crucial in ensuring unidirectional blood flow from the periphery to the heart: the presence of unidirectional valves in the arms and legs and the action of leg muscles on the adjacent veins [2].
Venous valves are unidirectional structures that prevent the backflow of blood. Their function is purely fluid-dynamic: when the upstream compartment has a higher pressure than the

downstream one, the valve opens, allowing blood flow. When the upstream pressure drops below that of the downstream compartment, the valve flaps close, isolating the compartment and preventing backflow. The closure of a valve interrupts the hydrostatic column, thereby reducing blood pressure in the downstream vascular bed.
The action of leg muscles, which is triggered during walking, exerts pressure against the walls of the veins, compressing them and causing the opening of the proximal valve, thus facilitating venous return. Conversely, when stationary, the veins in the legs accommodate between 300 and 800 ml of blood, leading to a significant increase in internal pressure within the vessels at the level of the feet, which rises from approximately 25-30 mmHg during walking to 80-90 mmHg when standing.
Another important aspect to consider when discussing veins is collapse. Collapse occurs when, due to the low transmural pressure levels in veins, the cross-sectional area of the vessel is reduced, leading to zero the pressure difference between the external environment and the intraluminal zone, thereby interrupting the hydrostatic column. This phenomenon affects the jugular veins in the upright position, where, due to the hydrostatic gradient, a negative transmural pressure is experienced, leading to vessel collapse. This collapse ensures controlled blood flow from the brain to the heart.
To highlight the main differences between the arterial and the venous system the following figure (Fig. 1.6) is reported. Diameters, wall thickness and mechanical properties are organized by vascular districts.

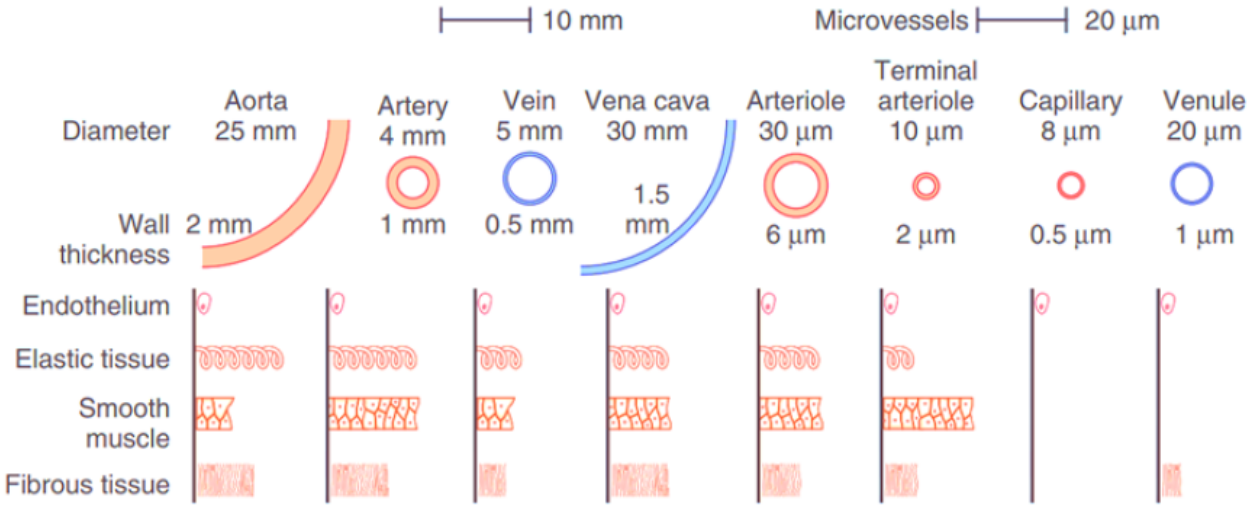

Figure 1.6: Characteristics of arterial and venous systems [3].

1.4 Cardiovascular regulation

To ensure the proper functioning of the cardiovascular system under conditions different from the optimal ones (supine posture), such as when the body is exposed to gravitational acceleration higher than 1G or to prolonged spaceflight, but also during a stand up movement from

supine to standing posture, short and/or long term regulation mechanisms are activated. The former operates within the initial seconds to minutes, while the latter — encompassing renal and hormonal mechanisms to regulate water and sodium balance, and consequently blood pressure — becomes effective over a period ranging from minutes to days.
We will focus on the short term mechanisms, in particular on three important controls which ensure the maintenance of a correct level of arterial and venous mean blood pressure and an adequate flow of blood towards the head. The control on arterial and venous pressure is accomplished by baroreflex and cardiopulmonary reflex, while the perfusion of the cerebral region is managed by cerebral autoregulation.

1.4.1 Baroreflex and cardiopulmony reflex

Arterial baroreceptors originating in the carotid artery and aorta play a pivotal role in the rapid reflex adjustments that accompany acute cardiovascular stressors. The carotid and aortic baroreflexes are comprised of unencapsulated free nerve endings located in the carotid sinus bifurcation and aortic arch. These mechanoreceptors function as high pressure sensors in a negative feedback control system that responds to beat-to-beat changes in arterial pressure by reflexively modifying the sympathetic and parasympathetic activity of the central nervous system in order to send signals to the efferent organs involved in the regulation. In particular, baroreflex activate changes in heart rate HR (chronotropic effect), cardiac contractility E (inotropic effect) and vascular tone (venous and arterial compliance C, total peripheral resistance TPR and unstressed volumes V^{un}) with the aim of returning the pressure to its original set point value [4].
The cardiopulmonary reflex receptors work in a similar way, but on the low pressure side of the cardiovascular system. They are located in heart (atria), great veins and blood vessels of the lungs and sense changes in central blood pressure CVP (low pressure sensors). Elevations in central pressure increase vagal afferent nerve firing reflexively decreasing sympathetic nerve activity (SNA), while reductions in central pressure evoke profound increases in SNA. Cardiopulmonary reflex works similarly to arterial baroreflex, controlling mainly arterial and arteriolar vasodilation/constriction and venous/venae cavae tone.
If the blood pressure falls below the set point level, these two control loop act increasing HR, maximum cardiac contractility E_{max} and peripheral resistance R, while reducing compliance C and unstressed volumes V^{un}. Conversely, when blood pressure rises above the set point, the opposite adjustments are implemented.

1.4.2 Cerebral autoregulation

Autoregulation of blood flow denotes the intrinsic ability of an organ or a vascular bed to maintain a constant perfusion in the face of blood pressure changes. In the cerebrovascular field, the process of cerebral autoregulation maintains a relatively constant cerebral blood flow during changes in perfusion pressure, like during posture or gravity changes. This is accomplished by active vasodilatation of the cerebral microvasculature during hypotensive stimuli and by vasoconstriction during increases in blood pressure. Cerebral autoregulation is generally effective within a mean arterial pressure range of 80 to 150 mmHg [5].

Chapter 2

Physiology alterations related to spaceflight

In space the human body is exposed to an altered and unfamiliar environment. The new set of stimuli imposes challenges on cardiovascular, muscle-skeletal and neuro-vestibular systems. These systems are less strained in weightlessness than on Earth and this leads to deconditioning during longer periods spent in space. As far as current experience has shown, this process continues throughout the stay in microgravity and poses severe challenges to astronauts returning to Earth. Understanding these changes and their severity is important in order to evaluate the feasibility of manned missions and ensuring a safe return to a gravitational field [6].
To study the consequences of long-term stay in microgravity, extensive physiological experiments during spaceflight are needed, but several practical considerations limit their feasibility. The reason why physiology tests are limited during space missions are the high cost of these tests, the reduced equipment available onboard, the limited time astronauts can address to physiological experiments, but also the small number of available subjects.
In light of these difficulties, different terrestrial experiments have been developed in order to bridge the gap between large volumes of required data and limited measuring opportunities in space. These experiments simulate weightlessness and include bed-rest and immersion studies, both aiming to remove the head to toe gravity vector acting on the body on Earth, but also parabolic flights, which are capable of reproducing short intervals of weightlessness. These experiments provide a wide amount of data and aim to simulate microgravity in order to predict and support the data collected during spaceflight missions.

2.1 Terrestrial experiments

2.1.1 Bed-rest studies

During bed rest, subjects spend hours (at least 12) to months exclusively in a supine position, in which they must perform all daily tasks including eating, drinking, washing and exercising. The keeping of this posture significantly decreases muscular efforts and reduces stress on the cardiovascular system [6]. When lying down, subjects no longer experience the gravity vector acting from head to toe and pulling fluids into the legs and feet. The horizontal position almost fully removes the hydrostatic pressures within the body so that the fluid redistributes

more evenly throughout the body, this also occurs in space.

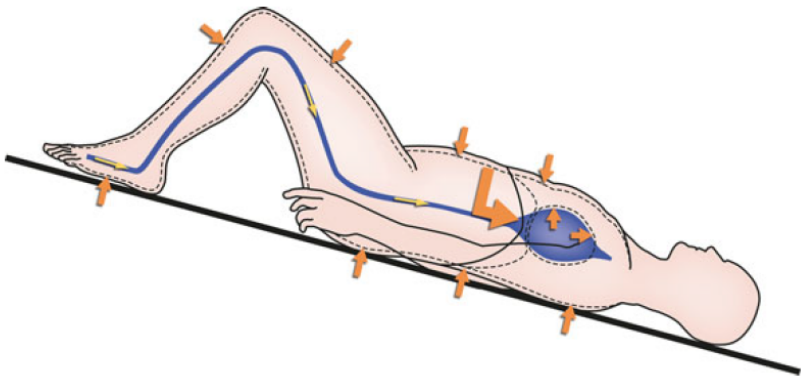

Figure 2.1: The schematic setup of a head-down tilt bed rest [6].

More specifically, a head-down tilt of $-6\,^\circ$ (Fig. 2.1) is used to induce a similar cephalic fluid shift as it occurs in space. Immediately after taking this position, subjects show a marked central shift of intravascular and interstitial fluid. Consequently, venous pressure, cardiac output, and stroke volume increase significantly. Subjects that persist in longer bed-rest studies experience changes that show a reduction in plasma volume within the first week, a dilatation and a relaxation in leg arteries within 50 days and a dysfunction of baroreceptors which are continuously exposed to pressure and therefore become less sensitive and responsive. All of these are indicators of cardiovascular adaptations to the level of extreme disuse.
A few hours of head-down bed rest are sufficient in triggering dizziness when regaining an upright posture, a state known as orthostatic intolerance. This is the reason why subjects are usually moved to a vertical position after bed rest with the help of a tilt table. This movement could be used to reproduce space reentry: the sudden reintroduction of head to toe gravity leads to an elevated heart rate, decreased central venous pressure, stroke volume, and cardiac output in response to the fluid movement to periphery.
Bed-rest experiments simulate not only the stay in microgravity (tilt angle of $-6\,^\circ$), but also the reentry phase (Head Up tilt test) and other different gravitational environments. For example, tilt of $9.5\,^\circ$ and $22.5\,^\circ$ can simulate Lunar and Martian gravity, respectively.
The drawbacks of this powerful terrestrial analogue are the maintenance of the hydrostatic pressure gradient present in the transverse plane (chest to back direction), which is absent in microgravity, and the continuous contact with the bed, that leads to an abnormal skin mechanoreceptors stimulation.

2.1.2 Water immersion studies

Water immersion (Fig. 2.2) leads to support unloading and a removal of gravity-induced pressure gradients in the body using the hydrostatic pressure of the water [6]. The two predominant forms of immersion are head out of water ('wet') immersion and dry immersion where the subject is enclosed by a waterproof lining. Wet immersion cannot exceed 6–12 h so that those

studies focus on short-term adjustments. The dry immersion method allows for long-term immersion (longest experiment lasted 56 days). Both forms of immersion have three main effects: they create supportlessness because forces act equally from all sides, they induce extensive physical inactivity and they cause hydrostatic compression of the superficial tissues and vessels. The third effect causes fluid movement from the interstitial to the intravascular space, as opposed to what happens during spaceflight where fluids move from blood vessels into tissues.

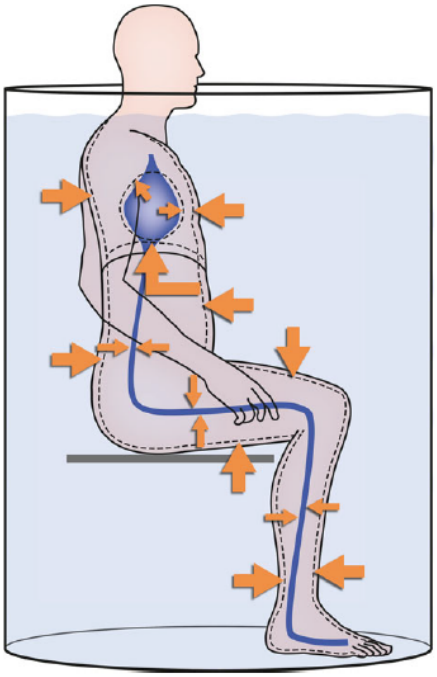

Figure 2.2: Schematic setup of head out of water immersion experiments. The body of subjects is fully immersed in water while the head remains above the water [6].

The pressure exerted on the legs by the water decreases the peripheral vascular capacity and leads to a redistribution of fluid from the lower extremities to the upper body with an increase in central blood volume, CO, SV and CVP.

2.1.3 Parabolic flight

The only way to have matter floating in weightlessness on Earth is during free fall from a drop tower, in sounding rockets or in aircraft parabolic flights. The latter is the only feasible option to combine with human experiments, making parabolic flights the only way to investigate the true influences of microgravity on the cardiovascular system without travelling to space.
Parabolas are flown in an airbus. The traiectory (Fig. 2.3) of the aircraft begins with horizontal flight and climbs to an angle of 47 ° during a pull-up phase, before creating a free-fall interval of 20–25 s. Thereafter, the aircraft dives back down to a horizontal flight mode and reiterates the process 30 times during one session. This creates subsequent periods of 1, 0, and 2 g levels allowing the study of transient phenomena occurring during the change from high to low gravitational fields and back again.

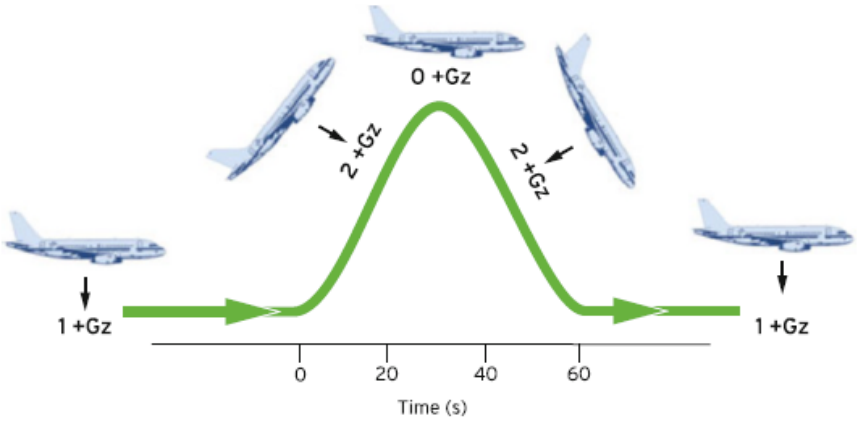

Figure 2.3: Single sequence flown by an airbus to create weightlessness inside the aircraft [6].

In general, parabolic flights have provided a better understanding of orthostatic intolerance, decreased peripheral blood flow and variation of heart size. As parabolic flights completely remove the density vector in the body, they achieve the same acute effect on the cardiovascular system as spaceflight: CO increases, HR decreases, regulation response is altered. However, the intervals of weightlessness do not exceed 30 s, so that only short-term adaptations can be observed and long-term changes remain speculations. Furthermore, the continuous transition from high to low gravity prevents variables from reaching a steady state.

2.2 Cardiovascular deconditioning

Following the brief review of terrestrial analogues, it can be concluded that none of them can entirely simulate a complete space mission. Parabolic flights are reliable experimental methods but provide data only for the initial seconds of spaceflight. Bed rest and water immersion both lead to an increase in central blood volume, resembling the effects induced by microgravity. However, these two conditions involve different primary mechanisms through which this shift occurs. Consequently, while some results are comparable and ground-based simulations serve as valuable analogues for spaceflight, they cannot fully substitute for experiments conducted in space. This highlights the necessity of conducting experiments during spaceflight to obtain the most accurate data for understanding human physiological adaptation to space environment.
A substantial body of research and experiments has been conducted in space in recent years. Regarding the cardiovascular system, the observed responses and results in space can be categorized into short-term changes (ranging from immediate responses to the first week in space) and long-term changes (spanning from one week to several months). Based on this classification, the following section will outline the most significant hemodynamic changes and the corresponding adaptations to the microgravity environment, compared to the conditions experienced under 1g on Earth.

2.2.1 Acute adaptation to microgravity

Among the main physiological changes experienced by astronauts during the initial stages of exposure to microgravity is the fluid shift from the lower extremities toward the compliant thoracic area. This phenomenon occurs due to the absence of gravity, which equalizes pressures at different sites along the body. The removal of hydrostatic pressure gradients results in increased pressure in the thoracic and head regions and decreased pressure in the lower extremities [6]. Conversely, the difference between the two regions of blood circulation, venous and arterial, is independent of gravity and persists in space.
The fluid shift lasts approximately 6 to 10 hours, during which about 2 liters of fluid are redistributed. This leads astronauts to experience a sensation of fullness in the head, nasal congestion, and increased intraocular pressure, in addition to the so-called "puffy face" syndrome, characterized by the enlargement of superficial veins in the head and neck. Conversely, the legs undergo a reduction in volume (approximately 1 liter per leg), leading to the so-called "chicken leg" syndrome, marked by a 30% decrease in leg circumference.
Another significant change is the onset of blood volume reduction as a response to the perceived blood overload. At least 17% of plasma volume is reduced during the first day of spaceflight, accompanied by increased urination due to a heightened diuretic stimulus, while the sensation of thirst diminishes [7].
Regarding mean arterial pressure (MAP), no clear trend has yet been identified. It appears to be variable and unstable, with no consensus among the results of different studies [6]. Some studies report an increase, others a decrease, while some indicate no significant change. This substantial variability in MAP may be related to the general instability of blood pressure during the initial phases of spaceflight and the anatomical differences in vascular structures. The cardiovascular system is actively seeking a new steady state under altered conditions, where oscillations in physiological parameters such as MAP represent a compensatory response to these challenges.
Considering the lower-pressure counterpart of the systemic circulation, the results obtained deviate from initial expectations. Central venous pressure (CVP), which rises during pre-flight procedures (2-3 hours before launch), surprisingly falls below normal values in the early stages of spaceflight. This may be due to a rapid increase in thoracic vessel compliance, allowing them to accommodate the fluid shift at a lower pressure.
Stroke volume (SV) and cardiac output (CO) are two additional cardiovascular variables immediately affected by fluid redistribution. With the disappearance of hydrostatic effects, the volume of blood within the heart nearly doubles, increasing cardiac preload and resulting in a greater volume of blood ejected per beat. Consequently, stroke volume increases, and since heart rate remains constant, cardiac output also rises. The concurrent increase in CO and decrease in CVP suggest a reduction in peripheral arterial resistance, likely due to arterial vasodilation, reaching values comparable to those observed in a seated position on Earth. This indicates that the cardiovascular system begins to relax within just one week of spaceflight.
Heart rate (HR) presents conflicting results but generally remains stable or shows a slight reduction. This is because the increase in SV enhances the efficiency of each heartbeat, reducing the need for higher contraction frequencies to maintain adequate blood supply. This decrease in HR is particularly evident during sleep phases, where it falls below terrestrial levels.

2.2.2 Long-term adaptation to microgravity

Immediate mechanical changes in the body are followed by a cascade of physiological mechanisms through which the body responds to these alterations. Subsequently, the body begins to adapt to the new stimuli by establishing a long-term steady-state set point. Within six weeks, the organism is able to reach this new equilibrium in microgravity, and during missions lasting up to a year, no further decrease is observed beyond this threshold. What occurs beyond this timeframe remains unknown. However, it is well established that the return to gravity becomes increasingly challenging following prolonged exposure and adaptation of the cardiovascular system to weightlessness.

The equalization of pressure across different regions of the body leads to the inactivation of baroreceptors and cardiopulmonary receptors, which are no longer subjected to pressure variations. On Earth, these receptors are continuously stimulated by changes in posture, but in microgravity, the absence of such fluctuations causes them to become almost dormant, contributing to cardiovascular deconditioning.

The most dominant long-term physiological adaptation, which affects various aspects of the cardiovascular system and beyond, is a reduction in fluid volume. The body perceives an excess of fluid due to increased thoracic filling, even though total body water and blood volume remain within normal terrestrial ranges. Consequently, a compensatory reduction in blood volume occurs. While this is an appropriate response to microgravity, it results in a fluid volume that would be classified as hypovolemic under Earth-based conditions. This adaptation involves a decrease in plasma volume by approximately 22%, leading to a 9–15% reduction in total red blood cell mass, a phenomenon referred to as "space anemia". The overall outcome is a 10–12% decrease in total blood volume [7]. The primary mechanisms driving this reduction include increased renal fluid excretion (diuresis), interstitial fluid redistribution, and reduced thirst leading to lower fluid intake. Within one week of spaceflight, a body mass loss of 2–3 kg is typically observed.

Direct measurements of cardiac output and stroke volume variations throughout long-duration spaceflight remain limited. Moreover, available data on stroke volume in microgravity present conflicting results, potentially due to differences in baseline conditions (e.g., upright, seated, supine) across studies. To resolve these inconsistencies, further research campaigns focusing on long-term cardiac adaptations in spaceflight are necessary.

As previously mentioned, during the initial phase of spaceflight, cardiac preload and stroke volume (SV) increase, leading to an expansion in heart volume. Over the long term, however, heart volume and size gradually decrease due to fluid loss, the absence of gravitational load on the heart, and reduced physical activity. This results in a 10–15% reduction in cardiac muscle mass, a condition known as cardiac atrophy.

Heart rate (HR) increases by approximately 10–15% compared to pre-flight seated or supine conditions, whereas arterial pressure exhibits a greater reduction in the absence of countermeasures, particularly when measured against pre-flight upright or seated values [7]. Various types of serious cardiac arrhythmias have been documented in space. However, it remains challenging to determine whether these are directly related to weightlessness or influenced by other flight-related factors, such as electrolyte imbalances, high stress levels, or sleep deprivation.

2.2.3 Orthostatic intolerance

The biggest challenge for the cardiovascular system arises upon return to Earth, as the deconditioned system is unable to efficiently adapt to the reintroduction of gravitational forces. This condition results in dizziness, sweating, pre-syncope, and a heightened tendency to faint, all of which are indicative of orthostatic intolerance (OI) [7].
Astronauts experiencing OI typically report an increased heart rate, decreased arterial pressure, and an elevated propensity to faint. The primary causes of orthostatic intolerance are directly linked to cardiovascular deconditioning during spaceflight. Among these, reduced blood volume (hypovolemia) is considered the most significant and observable factor, manifesting through decreased body weight and increased thirst. Furthermore, venous pooling in the lower extremities due to diminished blood volume leads to orthostatic hypotension and syncope.
Another crucial factor is the impaired ability of both arterial and venous vasoconstriction and vasodilation, which exacerbates venous pooling in the legs. Additionally, cardiac atrophy—characterized by a reduction in both the mass and size of the heart—further impairs cardiovascular function. The autonomic nervous system also undergoes dysfunction, resulting in a diminished or delayed baroreceptor response. Collectively, these physiological changes contribute to the onset and severity of orthostatic intolerance.
Not all astronauts experience OI to the same degree. Notably, female astronauts exhibit greater susceptibility than their male counterparts. Following short-duration spaceflights, all female astronauts have been observed to experience syncope, whereas only 20% of male astronauts display similar symptoms. Given that the primary causes of this condition stem from hypovolemia and blood redistribution towards the lower extremities, countermeasures aimed at increasing blood volume and enhancing vasoconstriction are expected to be the most effective in preventing OI-related symptoms. This is the reason why crew members typically undergo pre-reentry interventions such as saline solution administration to expand plasma volume and the use of lower body negative pressure devices to redistribute blood flow.

2.3 Muscle-skeletal and neurovestibular deconditioning

The cardiovascular system is not the only one affected by deconditioning during spaceflight; the muscle-skeletal and neurovestibular systems also undergo significant changes.
Among the different muscles of our body, we can find the the skeletal muscles, which can be categorized into postural (antigravity) muscles, responsible for maintaining posture and stability, and phasic muscles, which facilitate movement. Skeletal muscles account for approximately 40–45% of total body mass and are among the most affected by spaceflight. In particular, postural muscles in the lower body experience the highest degree of atrophy, as they play a crucial role in maintaining posture on Earth but are significantly impacted by weightlessness. Additionally, the increased use of the upper limbs during spaceflight further reduces the mechanical load on the legs.
Muscle strength and contractility decline in parallel with muscle mass due to unloading and prolonged confinement in a limited space. Furthermore, skeletal muscles become more susceptible to contraction-induced damage, which contributes to muscle weakness and soreness. Implementing daily exercise and countermeasures during missions is essential to mitigate the effects of muscle atrophy.

Moving on to the skeletal system, the primary concern in space-related pathology is bone health. Bone serves two essential functions: providing the rigid structural framework necessary for movement and physical activity, and acting as a reservoir for calcium within the body. Two fundamental cell types, osteoblasts and osteoclasts, continuously remodel bone within a complex regulatory network to maintain bone integrity, respond to changes in skeletal loading conditions, and ensure stable blood calcium levels. As a result, bone density naturally varies with age. During long-duration spaceflight, this equilibrium is disrupted. Factors such as low light exposure, elevated ambient CO_2 concentrations, and minimal mechanical loading promote bone resorption. Bone loss in microgravity occurs at a rate of approximately 1–2% per month and continues for several months after returning to Earth. In a weightless environment, certain skeletal regions experience significant unloading, predisposing bones to osteoporotic-like conditions. The calcium released from bone resorption accumulates in various tissues, including the kidneys, leading to a 60–70% increase in urinary calcium excretion within just a few days [8]. These significant variations in the skeletal system raise open questions regarding the feasibility of long-term missions. Some of the major critical issues include the acceleration of osteoporosis associated with aging, the lack of calcium recovery during extended missions, and the challenges of performing activities in different gravitational environments—such as Mars—following prolonged exposure to microgravity. It is therefore crucial to identify appropriate countermeasures to minimize bone loss.

Finally, let us discuss the neurovestibular system and the modifications it undergoes in the absence of gravity. This complex system comprises the five senses, the vestibular labyrinth, and all the reflexes that enable posture maintenance, coordinated movement, and balance. The vestibular labyrinth allows individuals to perceive their motion in space through two otolith organs and three semicircular canals. Spaceflight significantly impacts this system: in a microgravity environment, otoliths are no longer stimulated by head tilts, leading the brain to interpret head inclinations and translations in the same way. As a result, astronauts experience severe disorientation upon returning to Earth's gravitational environment. Vestibular reflexes are also profoundly affected by spaceflight. Upon returning from missions, most astronauts fail posturography tests, indicating an impaired ability to perceive their movement relative to their surroundings and disrupted vestibular input processing.

The neurovestibular system also encompasses the five senses, each of which is affected to varying degrees by microgravity. However, vision is the most impacted due to Spaceflight Associated Neuro-Ocular Syndrome (SANS), formerly known as Visual Impairment and Intracranial Pressure (VIIP). This condition is among the most concerning for long-duration spaceflight, and its underlying causes remain under investigation. Observed signs of SANS include optic disc edema, globe flattening and swelling, choroidal and retinal folds, hyperopic shifts, nerve fiber layer infarcts, brain upward shift, and increased brain ventricular volume. Astronauts have reported symptoms such as decreased near-visual acuity, visual scotomas, headaches, and deterioration of distance acuity. The prevailing hypothesis regarding the etiology of SANS suggests that it results from a slow but chronic increase in cerebral and ocular fluid and pressure, caused by the systemic cephalad fluid shift in weightlessness. This is theorized to lead to increased intracranial pressure (ICP) [9]. In microgravity, not only blood but also cerebrospinal fluid (CSF) is redistributed, shifting toward the head and contributing to elevated ICP. On Earth, intracranial pressure varies with changes in posture (e.g., from supine to sitting or standing). In microgravity, however, ICP remains consistently elevated at a level similar to the supine

position on Earth, exerting continuous stress on the eye. Another factor to consider is the potential link between ocular deformation and the differential between intraocular pressure (IOP) and intracranical pressure (ICP) [9], which appears to increase in microgravity, potentially contributing to globe flattening.
The primary challenge in fully understanding the cause of this condition lies in the invasive nature of ICP measurements, making them nearly impossible to perform during spaceflight. A comprehensive understanding of this phenomenon is essential to developing effective countermeasure protocols. If fluid shift toward the head is indeed the primary mechanism underlying SANS, any countermeasure capable of redirecting blood toward the lower body could help mitigate its effects. This would be critical in ensuring the feasibility of increasingly long-duration space missions.

2.4 Countermeasures

This section concludes the adaptation of the cardiovascular system to the absence of gravity by presenting various countermeasures that are currently in use or under development for future implementation. These countermeasures are categorized into those that require the active participation of the individual, such as physical exercise, and passive methods, including lower body negative pressure and specialized compression garments known as penguin suits.

2.4.1 Exercise

Physical exercise is one of the most effective countermeasures to prevent orthostatic instability upon return to Earth, primarily due to its beneficial effects on the cardiovascular system. Future astronauts undergo structured exercise programs on Earth to maintain physical fitness and prepare for spaceflight. While the microgravity environment itself does not present significant physical challenges, a high level of fitness is advantageous during liftoff, potential emergency evacuations, and extravehicular activities. However, the most critical physical exercise sessions take place during spaceflight. In fact, exercise is an essential component of the daily routine of an astronaut in orbit. The crew aboard the International Space Station (ISS) dedicates between two and three hours per day to physical training. To counteract the effects of weightlessness, astronauts utilize specialized exercise equipment, including a harness-secured treadmill that floats independently within the station, an ergometer, and a resistive exercise device designed to mitigate muscle atrophy caused by prolonged inactivity in microgravity.
The primary objective of in-flight exercise is to maintain mechanical loading on the musculoskeletal system, thereby reducing bone demineralization and calcium loss. Additionally, these sessions provide significant cardiovascular benefits. Exercise strengthens the heart and increases blood flow to the lower extremities, which experience reduced circulation in space. Studies have shown that performing acute maximal exercise during spaceflight can decrease orthostatic intolerance upon return, as well as restore blood volume and baroreflex function [6].
Despite the rigorous exercise routines followed during space missions, they are not sufficient to completely counteract the physiological deconditioning caused by microgravity. As a result, astronauts continue with physical rehabilitation and training upon returning to Earth.

2.4.2 Gravity Suits

Gravity suits are wearable devices designed to influence fluid distribution within the body and artificially generate gravity-like mechanical strain. An example of such a countermeasure is compression garments, including thigh compression cuffs used by Russian cosmonauts, which aim to reduce the fluid shift that occurs in microgravity.

Figure 2.4: Penguin suit: the anti-zero-G suit looks like standard Russian in-flight suit, but had additional elastic band and pulleys that created a force against which the body need to work [6].

Another Russian initiative in this field is the development of the Penguin suit (Fig. 2.4), a wearable system designed to impose gravitational-like strain on the body. The original anti-zero-G suit, first tested in 1975, resembled a standard blue in-flight suit but incorporated elastic bands and pulleys that generated resistance, requiring the wearer to exert effort against them [6]. More recent research efforts have focused on the development of advanced skinsuits made from lightweight, elastic materials that more effectively simulate gravitational forces while improving comfort. These suits apply pressure around the abdomen and lower extremities in a manner similar to the effects of gravity on Earth.
Developing a functional wearable system capable of counteracting physiological adaptations to microgravity and mitigating postflight complications would represent a significant advancement for human spaceflight. Such a technology could reduce the need for extensive in-flight exercise, allowing astronauts to allocate more time to critical mission activities, such as conducting scientific experiments.

2.4.3 Artificial gravity

Artificial gravity could be created by short radius centrifugation (Fig. 2.5). Astronauts could spend certain intervals during the day in an onboard centrifuge and hence be exposed to an apparent gravity vector. The magnitude of this force depends on the square of the angular velocity of the centrifuge and its radius. Artificial gravity has been shown to mitigate orthostatic

intolerance and reduce central blood volume redistribution. However, it also induces motion sickness, including nausea and vomiting, particularly when the head moves out of the plane of rotation [7].

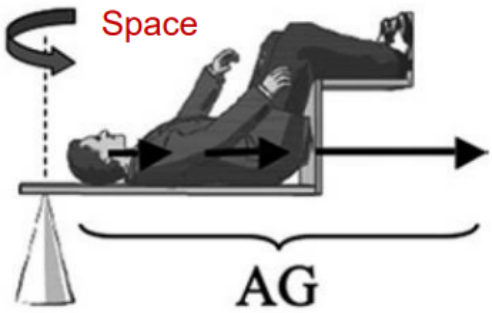

Figure 2.5: Short radius centrifugation and the gravity force vector [7].

Despite its potential benefits, the optimal combination of centrifuge size, rotational speed, and session duration required to counteract the physiological deconditioning of multiple systems has yet to be determined.
An alternative approach to onboard centrifuges is the concept of rotating an entire space station to generate artificial gravity. If a cylindrical space station were to spin around its central axis, centrifugal force would create the sensation of gravity, pulling objects and occupants toward the outer walls. However, implementing artificial gravity at the scale of an entire space station remains purely theoretical due to the immense energy demands required to sustain continuous rotation.

2.4.4 Lower Body Negative Pressure

The Lower Body Negative Pressure (LBNP) device (Fig. 2.6) is designed to redistribute blood from the upper body to the lower regions, including the pelvis and legs, thereby reducing central venous pressure and venous return. This technique involves placing the subject inside a cylindrical, airtight chamber that is sealed at the level of the iliac crests. A vacuum pump

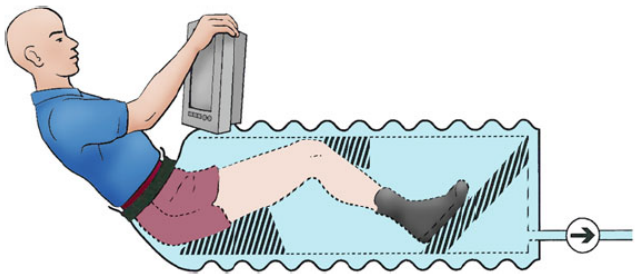

Figure 2.6: Lower body negative pressure: the setup is such that the lower body is fitted inside an airtight tube-like box, in which negative pressure is achieved with the help of a vacuum pump [6].

generates subatmospheric pressure within the chamber, which can be adjusted to modulate venous return. When LBNP is applied at a pressure of -40 to -50 mmHg, it induces physiological effects similar to those experienced during orthostatic stress on Earth, such as a decrease in blood pressure compensated by an increase in heart rate to maintain circulation to the upper body and head, as well as a fluid shift toward the lower extremities [7].
Integrating LBNP with exercise equipment, such as a treadmill, is a promising approach since the combination of negative pressure and weight-bearing activity simulates gravity-like conditions. The ultimate goal is to enable astronauts to perform exercise routines in space that closely replicate those on Earth, thereby preventing cardiovascular deconditioning and reducing health risks upon return.

Chapter 3

Mathematical modeling of the cardiovascular system

This chapter is dedicated to the description of the 0D-1D multiscale model of the cardiovascular system, which has been extended within the scope of this thesis. The original model was derived from the doctoral thesis of M. Fois [10] and C. Gallo [11] and has been expanded to incorporate the effects of Lower Body Negative Pressure on systemic hemodynamics. The original mathematical model will be described here, while the modifications introduced will be presented in Section 4.4.

The model consists of a one-dimensional representation of the arterial tree (from the aorta to the small arteries), coupled with a lumped-parameter representation of the remaining systemic arterial circulation (arterioles, capillaries) and the venous return (venules, veins, and venae cavae). The model is arranged in a closed-loop layout and includes 0D representations of the cardiac chambers, pulmonary circulation, coronary circulation, and cerebral circulation (from the Circle of Willis to the deep circulation). Additionally, a lumped-parameter model of the ocular globe architecture is also included. In Fig. 3.1, a detailed scheme of the multiscale model is provided.

The cardiovascular system (CVS) model is calibrated for a healthy male individual aged 28 years, with a weight of 75 kg and a height of 175 cm. Gravity is incorporated into the CVS model equations to account for posture-induced effects by considering the angle between the longitudinal body axis and the horizontal reference within a simulated tilt-table framework.

The one-dimensional component of the model will first be described, followed by its zero-dimensional counterpart.

3.1 1D model of the arterial system

The arterial network is composed of 63 large arteries (49 systemic plus 14 coronary arteries), starting from the aorta and extending towards all the body periphery via successive bifuractions, branching and gradual cross-section tapering. Fig. 3.2 rapresents the arterial tree, while table in Appendix A.1 gives arterial tree geometry and features. Blood is treated as an incompressible fluid. Therefore, the 1D axisymmetric incompressible form of Navier-Stokes (NS) equation for mass and momentum balance can be applied to describe blood motion. After some

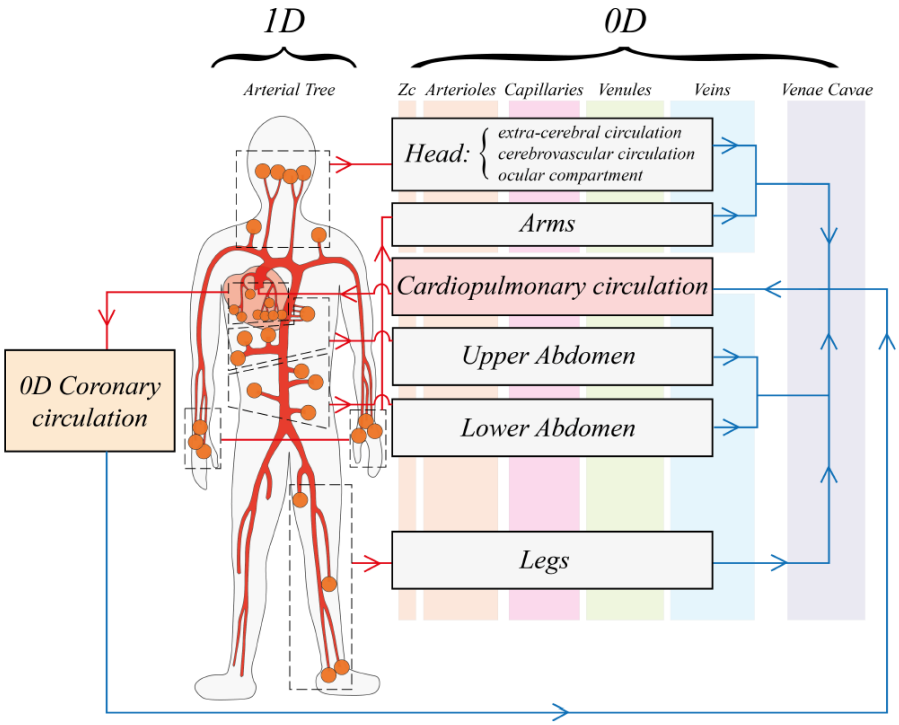

Figure 3.1: Illustration of the global multiscale cardiovascular model. The 1D arterial tree is sketched in red, red arrow indicate the arterial blood pathway, whereas blue arrows denote venous return blood pathway. Orange circles denote 1D terminal arteries linked to the downstream 0D compartments, grouped into regions from head to legs. Vertical rectangles (orange, pink, green and blue, from left to right) divide the 0D peripheral circulation into arteriolar, capillary, venular, venous and venae cavae compartments. Zc are arteriolar characteristic impedances [10].

manipulations, NS reads like:

$$\begin{cases} \dfrac{\partial A}{\partial t} + \dfrac{\partial Q}{\partial x} = 0, \\ \dfrac{\partial Q}{\partial t} + \dfrac{\partial}{\partial x}\left(\beta \dfrac{Q^2}{A}\right) + A\dfrac{1}{\rho}\dfrac{\partial p}{\partial x} - N_4 \dfrac{Q}{A} - Ag\sin\gamma\sin\alpha = 0. \end{cases} \tag{3.1}$$

where $A(x,t)$ and $Q(x,t)$ are vessel cross-section area and blood flow rate, respectively, t is time and x the vessel axial coordinate. Blood is modeled as a Newtonian fluid with constant density $\rho = 1050\ kg/m^3$ and dynamic viscosity $\mu = 0.004$ Pa s. The Coriolis coefficient β and the viscous coefficient N_4 are computed assuming a flat-parabolic velocity profile over each vessel cross-section area. Gravity is introduced in equations 3.1 through the term $g\sin\gamma\sin\alpha$, where g is gravity acceleration magnitude, γ is the vessel orientation with respect to the frontal transverse body axis and α is the vessel inclination with respect to the horizontal reference (i.e. the tilt angle).
The mass and momentum balance equations 3.1 govern three dependent variables that describe blood hemodynamics: the local vessel cross-sectional area A(x,t), the blood flow rate $Q(x,t)$, and the blood pressure $p(x,t)$. Consequently, an additional equation is required to close the

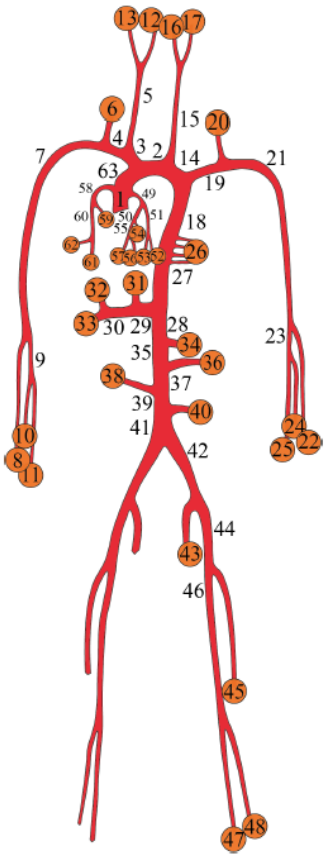

Figure 3.2: Illustration of the 1D arterial tree, with black numbers identifying each of the 63 large arteries. Orange circles denote 1D terminal arteries at 1D-0D arteriolar interfaces [10].

mathematical system, specifically a constitutive equation that characterizes the interaction between blood and vessel walls based on the mechanical properties of the local vasculature. This equation establishes an algebraic relationship between blood pressure $p(x,t)$ and the local cross-sectional area $A(x,t)$, accounting for the elastic and viscoelastic properties of arterial walls. It is important to note that the considered pressure is the transmural pressure, which coincides with the intraluminal pressure when the external pressure is negligible. However, if an external pressure is applied, such as in the case of Lower Body Negative Pressure (LBNP), the constitutive relation must also incorporate the contribution of the external environment:

$$p^t = p - p_{ext} = B_1 + B_2 A + B_3 A^2 + B_4 A^3 - B_5 \frac{1}{\sqrt{A}} \frac{\partial Q}{\partial x} - \hat{E} I \left(\left(\frac{A_b}{A} \right)^m - 1 \right) + p_b \qquad (3.2)$$

where p^t represents the transmural pressure, p denotes the intraluminal pressure, and p_{ext} is the external pressure. The terms $B_1 + ... + B_4 A^3$ correspond to the elastic component of the pressure, while $B_5 \frac{1}{\sqrt{A}} \frac{\partial Q}{\partial x}$ represents the viscoelastic component of the pressure, which is associated with the mechanical properties of the vessel walls. Additionally, $\hat{E} I \left(\left(\frac{A_b}{A} \right)^m - 1 \right) + p_b$ denotes the hyperbolic partial collapse model which applies to carotid and vertebral arteries numbered as 6, 12, 13, 16, 17 and 20. This constitutive relation is substituted into the momentum equation of system 3.1, thereby closing the problem.

3.1.1 Boundary conditions

Since the arterial tree consists of conduits arranged both in series and in parallel, it is essential to define appropriate boundary conditions at the interfaces between parent and daughter vessels at bifurcations, as well as at the 0D-1D interfaces. These interfaces include the inlet section of the aorta, which originates from the aortic valve and, consequently, from the cardiopulmonary circulation, and the outlet of small arteries leading to the 0D compartments of the peripheral microcirculation. The interface between small arteries and the microcirculation is characterized by a set of lumped characteristic impedances Z_c, which contribute to the definition of the boundary conditions.
Since the system of partial differential equations 3.1 involves two independent variables, namely the arterial cross, sectional area $A(x,t)$ and the blood flow rate $Q(x,t)$, an equal number of boundary conditions must be imposed at each interface, ensuring one condition for each dependent variable. Moreover, the boundary conditions for the 1D arterial problem must satisfy a dual nature: (i) physical boundary conditions must be imposed and respected, accounting for the effect of adjacent CVS components (0D disctricts or 1D arterial vessels of a given bifurcation) from which they are determined; (ii) compatibility conditions, extracted from the current vessel 1D internal domain through the method of characteristics.
Indeed, at each arterial 1D boundary, one physical condition coming from the external domain should be imposed in combination with one compatibility condition coming from the internal domain of the considered 1D vessel. Fig. 3.3 displays physical and compatibility boundary conditions for each types of interface.

Physical boundary conditions

Let us analyze the physical boundary conditions at the three types of interfaces.

- Aortic entrance: the initial arterial segment of the arterial tree, specifically the aortic root, is connected upstream to the zero-dimensional (0D) model of the aortic valve. This 0D valve model determines the aortic blood flow, Q_{ao}, which subsequently enters the aorta through the aortic root. Consequently, the time-dependent flow rate, $Q_{ao}(t)$, is applied as an external physical boundary condition at the aortic entrance.

- Terminal branches: as previously stated, the coupling between the one-dimensional (1D) distal branches and the subsequent zero-dimensional (0D) arteriolar compartments is achieved through a set of characteristic impedances, Z_c, connected to each 1D aortic terminal branch. These local characteristic impedances are defined to minimize wave reflections at the terminal boundaries of the 1D model, and their formulation is given by:

$$Z_c = \frac{\rho}{cA} \tag{3.3}$$

  where A is the local cross-sectional area and c the local wave velocity. Given the generic terminal branch, blood flow drained from the 1D terminal artery can be determined as

$$Q_{art1D} = Q_{art0D} = \frac{p_{out1D} - p_{art0D}}{Z_c} \tag{3.4}$$

  where p_{art0D} is 0D arteriolar compartment pressure, while p_{out1D} is obtained from A_{out1D} through the corresponding compatibility boundary condition.

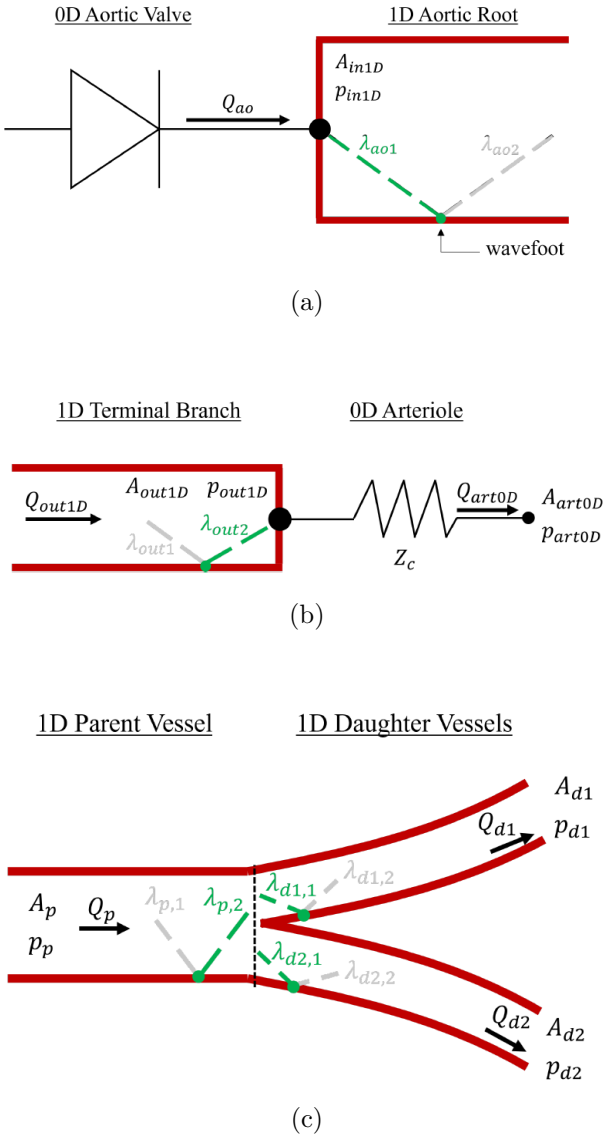

Figure 3.3: Physical and compatibility boundary conditions: a) aorta entrance, b) terminal branch and c) bifurcation [10].

- Arterial bifurcations: at junctions between arterial parent e subsequent daughter vessels physical boundary conditions are determined via mass and total pressure conservation across the single bifurcation

$$\begin{cases} Q_p = Q_{d1} + Q_{d2} + \dots, \\ p_p + \frac{1}{2}\rho\left(\frac{Q_p}{A_p}\right)^2 = p_{d1} + \frac{1}{2}\rho\left(\frac{Q_{d1}}{A_{d1}}\right)^2 = p_{d2} + \frac{1}{2}\rho\left(\frac{Q_{d2}}{A_{d2}}\right)^2 = \dots. \end{cases} \tag{3.5}$$

  Therefore, in a standard bifurcation consisting of a parent vessel (p) and two daughter vessels ($d1$ and $d2$), the boundary value problem involves six unknowns (A_p, A_{d1}, A_{d2}, Q_p, Q_{d1} Q_{d2}). To determine such unknowns three equations are provided by the system

of physical boundary conditions (conservation of mass and total pressure eq. 3.5), while the remaining three are obtained from the corresponding compatibility equations.

Compatibility boundary conditions

The method of characteristics is applied to determine directions along which signals propagate within arterial vessels. Along these directions the corresponding characteristic variables are conservated. From the quasi-linear form of the mass and momentum balance equations 3.1 (to follow each mathematical step see [10] and [11]), one can compute the slope of left (subscript 1) and right (subscript 2) characteristic lines:

$$\lambda_{1,2} = \beta \frac{Q}{A} \pm c_\lambda \tag{3.6}$$

with c_λ being the local wave celerity (wave speed), defined as

$$c_\lambda = \sqrt{\frac{\beta(\beta-1)Q^2}{A^2} + \sum_{j=1}^{3} \frac{jA^j B_{j+1}}{\rho} + \frac{\hat{E}I}{\rho}\frac{mA_b^m}{A^m}} \tag{3.7}$$

Then, the characteristic variables are obtained as

$$\lambda_1 : Q^{n+1} = \lambda_2^n A^{n+1} + K_1, \quad \lambda_2 : Q^{n+1} = \lambda_1^n A^{n+1} + K_2 \tag{3.8}$$

respectively, linking dependent variables A and Q values on the corresponding boundary (left: subscript 1; right: subscript 2) at time t_{n+1} to their respective values at time t_n and at the wavefoot situated at distance $\lambda\Delta t$ from the corresponding boundary. For the definition of the terms K_1 and K_2, please refer to Appendix A.2.
Now, by combining equation 3.8 with the constitutive relation 3.2 and the system 3.5, it is possible to solve for the unknowns at each interface.

3.2 0D model

The 0D counterpart of the model is devoted to represent the remaining systemic arterial circulation (arterioles, capillaries), the venous return (venules, veins, and venae cavae), but also the cardiac chambers, the pulmonary circulation, the coronary circulation, the cerebral circulation (from the Circle of Willis to the deep circulation) and the ocular globe.

3.2.1 Systemic microcirculation and venous return

Starting from the 1D-0D interface at multiple distal arterial branches an arteriolar 0D circuital model is included for each 1D terminal artery, for a total of 24 arteriolar districts (Fig. 3.4). Arteriolar compartments are then grouped into five body macro-regions: head (H), arms (A), upper abdomen (UA), lower abdomen (LA) and legs (L). For each region, one capillary (cap), one venular (ven) and one venous (V) compartment are introduced. Three additional districts are included to represent superior (svc), inferior (ivc) and abdominal (avc) vena cava, collecting

Arteriolar #id	R [mmHg s/ml]	C [mmHg/ml]	L [mmHg s/ml]	V^{un} [ml]	V [ml]
Vertebral 6/20	25.88	0.013	0.019	4.2	4.72
Radial 8/22	17.03	0.014	0.018	3.6	4.16
Interosseous 10/24	393.70	0.0009	0.070	3.6	3.63
Ulnar II 11/25	19.69	0.014	0.018	3.6	4.16
Internal Carotid 12/16	23.60	0.015	0.017	4.2	4.8
External Carotid 13/17	21.85	0.015	0.017	4.2	4.8
Intercostals 26	5.61	0.054	0.009	6.9	9.06
Hepatic 31	16.24	0.021	0.015	30.6	31.44
Gastric 32	8.91	0.033	0.012	9.3	10.62
Splenic 33	21.33	0.014	0.018	11.6	12.16
Superior Mesenteric 34	3.85	0.081	0.007	15.9	19.14
Renal 36/38	4.31	0.068	0.008	5.9	8.62
Inferior Mesenteric 40	30.74	0.011	0.02	11.9	12.34
Inner Iliac 43	23.48	0.014	0.018	3.5	4.06
Deep Femoral 45	13.37	0.023	0.014	14.4	15.32
Anterior Tibial 47	14.03	0.023	0.014	14.4	15.32
Posterior Tibial 48	30.44	0.010	0.021	14.4	14.80

Figure 3.4: 0D arteriolar settings: R arteriolar resistance, C compliance, L inertance, V_{un} unstressed volume and V total blood volume [10].

blood from prior venous compartments (also belonging to different regions) and directly connected to the subsequent downstream cardiopulmonary circulation. The subdivision of the 0D systemic circulation into five distinct regions allows for evident distinction of the gravitational effects onto different body compartments, from head to feet, which is relevant for the present thesis, where it will be necessary to include the effect of LBNP solely on the leg compartment. Systemic distal circulation (arteriolar), microcirculation and venous return are represented as lumped parameter compartments according to an electric analogy and following the 3-element Windkessel approach [10]. Each vascular district (or compartment, that is arterioles, capillaries, veins or venae cavae) belonging to a given body region is composed of a 3-element RLC electrical circuit accounting for vessels hydraulic resistance (R), compliance (C) and blood inertia (L). Fig. 3.5 schematizes one generic region of the 0D systemic circulation. Equations

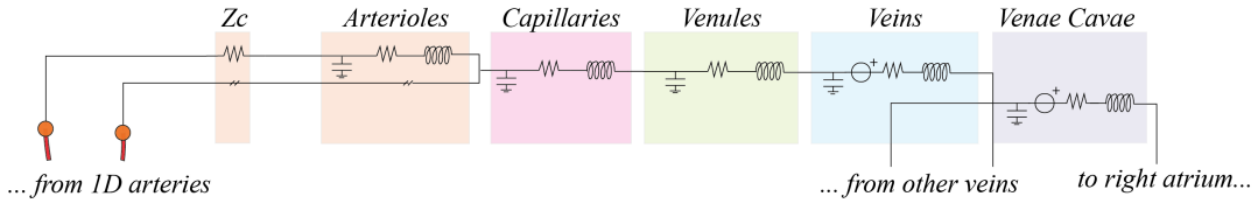

Figure 3.5: Generic region of the 0D systemic circulation. From left to right, past the characteristic impedance(s) connecting to the 1D counterpart, arteriolar, capillary, venular, venous and venae cavae compartments are represented [10].

governing blood motion in the (i, j)-th 0D compartment are

$$\frac{dV_{i,j}}{dt} = Q_{i,j-1} - Q_{i,j} \tag{3.9}$$

for mass balance, and

$$\frac{dQ_{i,j}}{dt} = \begin{cases} \frac{p_{i,j}+\Delta p^h_{i,j}-R_{i,j}Q_{i,j}-p_{i,j+1}}{L_{i,j}}, & \text{if } j \in \{v, \text{svc}, \text{ivc}, \text{avc}\} \\ \frac{p_{i,j}-R_{i,j}Q_{i,j}-p_{i,j+1}}{L_{i,j}}, & \text{if } j \in \{\text{art}, \text{cap}, \text{ven}\} \end{cases} \tag{3.10}$$

for momentum balance, where subscript i corresponds to the belonging body region (H, A, UA, LA, L), whereas j denotes the compartment (art, cap, ven, v, svc, ivc, avc). Intraluminal pressure of the (i,j)-th compartment is indicated with $p_{i,j}$, blood flow rate is denoted as $Q_{i,j}$, with $p_{i,j+1}$ and $Q_{i,j-1}$ being blood pressure and flow rate of the following and previous 0D compartments, respectively. $\Delta p^h_{i,j}$ is the hydrostatic pressure term and is expressed through the Stevino's law:

$$\Delta p^h_{i,j} = \rho g \Delta h_{i,j} sin\alpha, \tag{3.11}$$

where ρg is blood specific weight, $\Delta h_{i,j}$ is the hydrostatic height of the corresponding fluid column and α is the compartment orientation with respect to the horizontal reference (tilt angle). Blood column hydrostatic heights are associated with the anatomical length of the corresponding compartments projected along the longitudinal body axis. $V_{i,j}$ is the compartmental total blood volume, obtained as the summation of the corresponding unstressed blood volume $V^{un}_{i,j}$ and the stressed blood volume. This latter depends on the compartmental transmural pressure $p^t_{i,j} = p_{i,j} - p^{ext}_{i,j}$ and on the associated compliance $C_{i,j}$ according to the following constitutive law

$$V_{i,j} = V^{un}_{i,j} + p^t_{i,j} C_{i,j} = V^{un}_{i,j} + \left(p_{i,j} - p^{ext}_{i,j}\right) C_{i,j}, \tag{3.12}$$

where symbol $p^{ext}_{i,j}$ is extravascular pressure, corresponding to either intrathoracic, intracranial, intramyocardial or external (as in the LBNP application case) pressure according to the specific compartment (where no external pressure is specified, an external environmental relative pressure of 0 Pa is assumed). An additional relation can be derived for blood pressure $p(t)$ by combining equations 3.9 and 3.12:

$$\frac{dp_{i,j}}{dt} = \frac{Q_{i,j-1} - Q_{i,j}}{C_{i,j}}. \tag{3.13}$$

Equation 3.12 cannot be applied to the leg venous compartment due to its linear nature. In fact, this district is characterized by non-linear effects of distending veins volume where subject to high pressure level caused by gravitational stress. This non linear $p - V$ relation related to the leg veins compartment reads like:

$$V_{L,v} = V^{un}_{L,v} + \frac{2\Delta V_{max}}{\pi} arctan\left(\frac{\pi C_{L,v}}{2\Delta V_{max}} p^t_{L,v}\right) \tag{3.14}$$

in which ΔV_{max} is the maximum distending volume of leg veins $C_{L,v}$ is the leg venous compliance at zero transmural pressure $p^t_{L,v}$.

The 0D counterpart of the model encompasses also venous valves present in the veins. They ensure unidirectional flow in human veins, and thus preventing from venous blood backflow or reverse flow. These valves are introduced in the leg and arms venous compartment as non-ideal diodes. To a deeper insight in their mathematical modeling see [10].

3.2.2 Cardiopulmonary and coronary circulation

The 0D model of the cardiopulmonary circulation includes lumped models of the four cardiac chambers (left and right atrium and ventricle la, lv, ra, rv) and the pulmonary circulation. The cardiopulmonary circulation completes the closed-loop CVS global model by draining blood collected from superior and inferior venae cavae to be then ejected again into the 1D aorta. Cardiac chambers are governed by the following constitutive equation

$$p_{ch} = E_{ch}\,(V_{ch} - V_{ch}^{un}) + ITP, \tag{3.15}$$

where cardiac transmural pressure $p^t = p_{ch} - ITP$ is linked to the stressed volume $(V_{ch} - V_{ch}^{un})$, whereas the elastance E_{ch} is a function of time and is governed by the relation

$$E_{ch} = E_{ch,A} e_{ch} + E_{ch,B}. \tag{3.16}$$

$E_{ch,A}$ and $E_{ch,B}$ are the amplitude and baseline values, respectively, of the single-chamber's elastance, while $e_{ch}(t)$ is a shape function differently defined for atrium and ventricle [10].
Arterial and venous pulmonary circulations are described simply as RC lumped compartments, that is by including a lumped viscous resistance and a vascular compliance. Equations governing these compartments read

$$\frac{dp_j}{dt} = \frac{Q_{j-1} - Q_j}{C_j} + \frac{d(ITP)}{dt} \tag{3.17}$$

and

$$Q_j = \frac{p_j - p_{j+1}}{R_j} \tag{3.18}$$

where $j-1$ refers to pulmonary valve, $j+1$ to pulmonary veins when $j = pa$, whereas $j-1 = pa$ and $j+1 = lv$ when $j = pv$. ITP is the intrathoracic pressure which is expressed as a function of posture through tilt angle (α) and gravity acceleration g [10].
Specific 0D coronary microvascular districts are linked to each 1D large coronary artery outlet section to describe downstream vascular beds perfusing the myocardium. The coronary microvascular model is described in detail in [10].

3.2.3 Cerebrovascular and ocular hemodynamics

The model of the cerebrovascular circulation is a lumped representation of the main large cerebral arteries of the circle of Willis, departing from internal carotid and vertebral arteries of the global CVS model and branching into the right and left pial circulation and intracerebral arterioles (subdivided into anterior, middle and posterior distal compartments, communicating one another through cortical collateral vessels). The vessel compliances and hydraulic resistances of the pial circulation are controlled by the action of cerebral autoregulation (aimed at maintaining nearly-constant level of cerebral blood flow, CBF) and CO_2 reactivity.

In Fig. 3.6 a more detailed representation of the cerebrovascular circulation is illustrated, both encompassing cerebrovascular and extra-cerebral circulations and their circuital layout. The only difference with respect to the other 0D systemic compartments is that intracranial pressure ICP is applied as extravascular pressure onto head veins, so that equation 3.12 reads

$$V_{H,v} = V_{H,v}^{un} + (p_{H,v} - ICP)\,C_{H,v}. \tag{3.19}$$

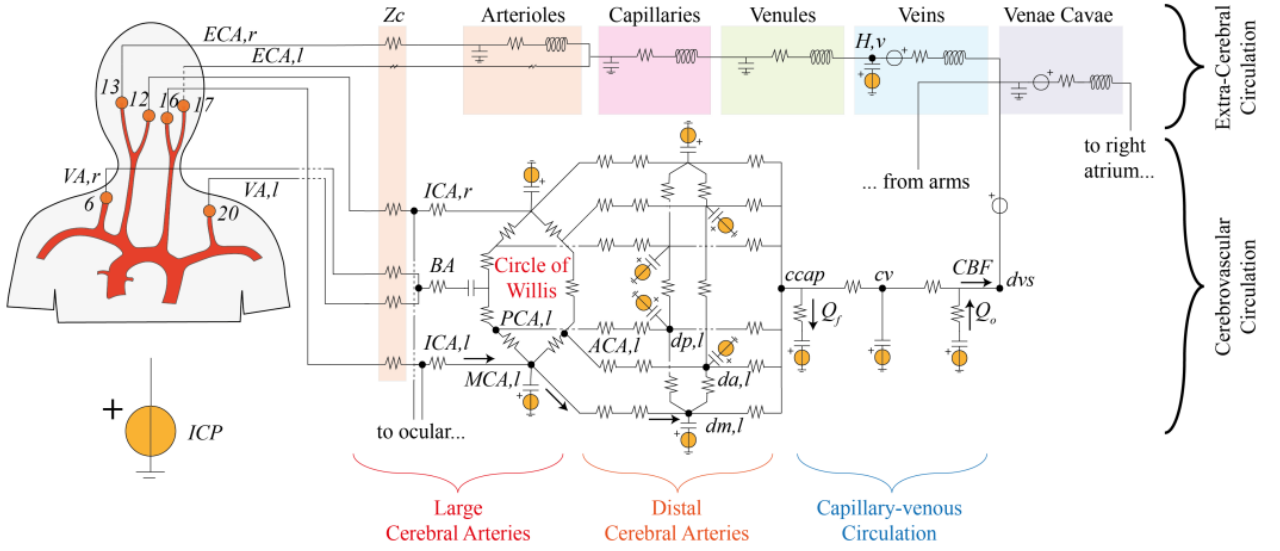

Figure 3.6: Illustrative scheme of the 0D cerebrovascular model architecture, connected from upstream to 1D internal carotid and vertebral arteries (No. 6, 12, 16, 20), while from downstream to 0D superior venae cavae [10].

A unique capillary-venous branch closes the cerebrovascular network connecting it to the superior vena cava of the global CVS model. The formation and outflow dynamics of the cerebrospinal fluid (CSF) and the hydrostatic contribution due to gravity regulate intracranial pressure (ICP) via a non-linear intracranial compliance. Equation at the base of this complex model are Kirchhoff's law at the nodes ($Q_{in} = Q_{out1} + Q_{out2}$) of the circuit, conservation of mass (Eq. 3.9), Ohm's law ($Q = \frac{\Delta p}{R}$) and the pressure constitutive equation 3.19. To analyze the full cerebrovascular model's set of equation please see [10].
The present CVS mathematical model includes also a lumped parameter model of the eye and ocular circulation to account for ocular-vascular dynamics and interactions in view of potential ocular anomalies and disorders triggered by not only posture and gravity changes, but also application of LBNP (for example SANS). The adopted ocular circulation model (Fig. 3.7) is plugged into the global CVS model at the level of internal carotid arteries and the outflow is then connected to the dural venous sinus, at the outlet section of the cerebrovascular model. The lumped-parameter model of the eye is composed of six compartments governing intraocular pressure (IOP) and ocular globe volume (V_g), using arterial and venous blood pressure at the level of the eye (named $p_{a,eye}$ and $p_{v,eye}$, respectively) as well as the intracranial pressure (ICP) coming from the cerebrovascular model, as inputs. IOP and V_g are modeled through the following governing equations:

$$\frac{dIOP}{dt} = \frac{1}{C_g}\left(C_{rg}\frac{dICP}{dt} + C_{ag}\frac{dp_{a,eye}}{dt} + C_{vg}\frac{dp_{v,eye}}{dt} + Q_{aq,in} + C_{tm}EVP - Q_{uv} - C_{tm}IOP\right) \tag{3.20}$$

and

$$\frac{dV_g}{dt} = C_{ag}\frac{d}{dt}\left(p_{a,eye} - IOP\right) + C_{vg}\frac{d}{dt}\left(p_{v,eye} - IOP\right) + Q_{aq,in} + C_{tm}\left(EVP - IOP\right) - Q_{uv} \tag{3.21}$$

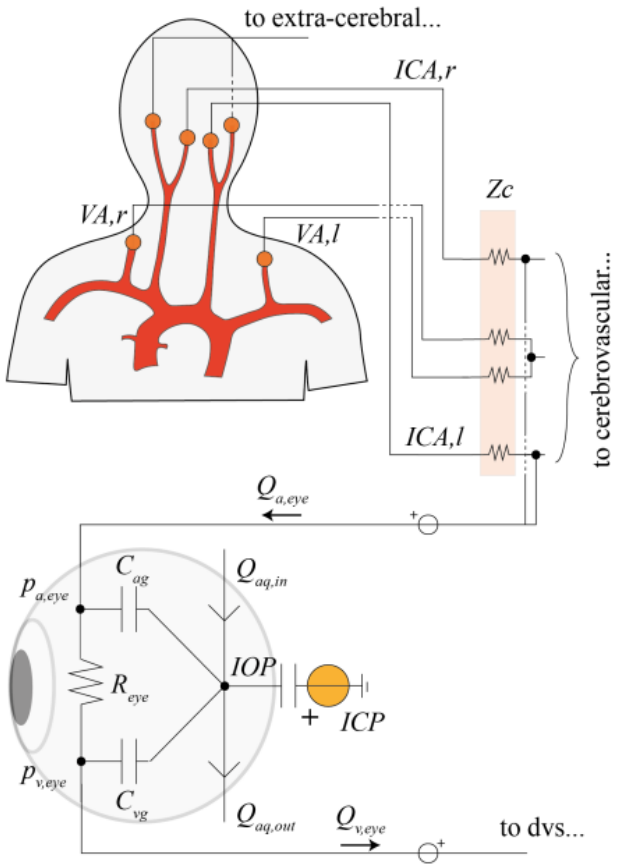

Figure 3.7: Illustration of the lumped ocular compartment, connected from upstream to internal carotid arteries prior to entering the cerebrovascular circulation, while from downstream to dural venous sinus at the outlet of the 0D cerebrovascular model [10].

where C_g is the globe compliance, C_{rg} is the retrobulbar subarachnoid space-to-globe compliance, C_{ag} is the arterial blood-to-globe compliance, C_{vg} is the venous blood-to-globe compliance, $Q_{aq,in}$ is the aqueous humor formation rate, C_{tm} is the aqueous outflow facility, Q_{uv} is the uveoscleral outflow rate and EVP is the episcleral venous pressure.
To integrate the ocular model with the global CVS model, arterial eye input ($Q_{a,eye}$) and venous eye output ($Q_{v,eye}$) flow rates shall be determined. These are obtained from the mass conservation and the pressure constitutive law 3.13 applied to the ocular arterial and venous blood compartments.

3.3 Short term regulation mechanisms

As previously explained (Chapter 1.4.1), the baroreflex and cardiopulmonary reflex play a crucial role in maintaining the correct levels of central arterial and venous pressure, respectively, while cerebral autoregulation is responsible for maintaining a physiological amount of blood flow to the head during changes in posture and gravitational environment. Fig. 3.8 illustrates the efferent organs controlled by each of the three short-term regulation mechanisms.

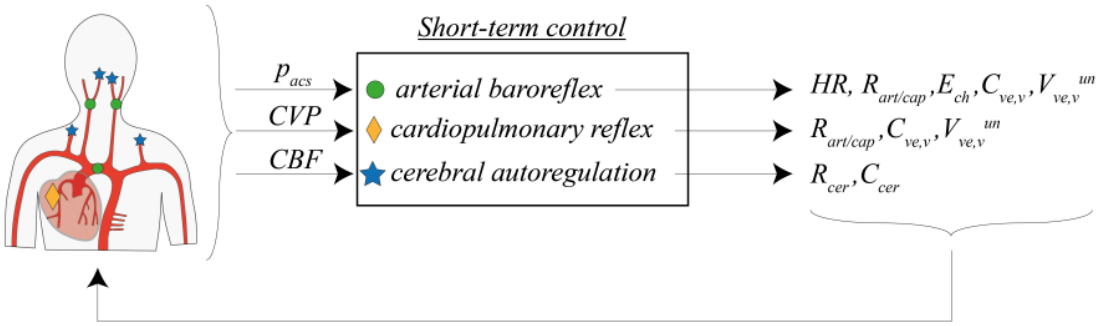

Figure 3.8: Schematic representation of short-term control mechanisms (baroreflex, cardiopulmonary reflex and cerebral autoregulation) functioning and operational flow [10].

Baroreflexes trigger different responses (variations in HR, E_{max}, $C_{ve/v}$, R_{art}, R_{cap}, $V_{ve/v}^{un}$) when they sense sensitive changes in the high-pressure side of the systemic circulation. To mathematically model this behavior, a control parameter has been defined based on the pressure signals sensed by the three baroreflex sensors. This control parameter is the mean aortic-carotid sinus pressure $\bar{p}_{acs}$ and is calculated by averaging the pressure signals from the three receptors located in the aortic arch $p_{aa}(t)$ and in right $(p_{cs,R}(t))$ and left $(p_{cs,L}(t))$ carotid sinus, over a cardiac period (RR)

$$\bar{p}_{\text{acs}} = \frac{1}{3RR}\int_{RR}\left(p_{\text{AA}}(t) + p_{\text{cs},R}(t) + p_{\text{cs},L}(t)\right)\,dt. \tag{3.22}$$

Then, sympathetic (n_s) and parasympathetic (n_p) activities are determined as

$$n_s(\bar{p}_{acs}) = \frac{1}{1+\left(\frac{\bar{p}_{acs}}{\bar{p}_{acs,tg}}\right)^{\nu}}, \qquad n_p(\bar{p}_{acs}) = \frac{1}{1+\left(\frac{\bar{p}_{acs}}{\bar{p}_{acs,tg}}\right)^{-\nu}} \tag{3.23}$$

where $\bar{p}_{acs,tg} = 89.01$ mmHg is the reference (target) value and $\nu = 7$ is the stepness of response. Being $y_m(t)$ the generic efferent organ controlled by arterial baroreflex, i.e. resistances $R_{i,art}$ $R_{i,cap}$, volumes $V_{i,v}^{un}$ $V_{i,ve}^{un}$, compliances $C_{i,v}$ $C_{i,ve}$, maximum cardiac elastance $E_{ch,max} = E_{ch,A} + E_{ch,B}$ and hart rate HR, with i denoting 0D body macro-region, its time evolution is given by

$$\frac{dy_m}{dt} = \frac{1}{\tau_m}\left(-y_m + \alpha_m n_s(\bar{p}_{acs}) - \beta_m n_p(\bar{p}_{acs}) + \gamma_m\right) \tag{3.24}$$

where α_m, β_m, γ_m and τ_m are saturation and time delay parameters reported in Table 3.1.

Cardiopulmonary reflex acts in a completely similar manner, but on the lower pressure side of the systemic circulation. Moreover, its responses encompass only peripheral resistances $(R_{art/cap})$ and venous tone $(V_{ve/v}^{un}$ and $C_{ve/v})$. Cardiopulmonary low-pressure receptors are located in the right atrium, so the pressure in this chamber, $p_{ra} = CVP$, averaged over a cardiac period, is used as the control parameter

$$\bar{p}_{cp} = \frac{1}{RR}\int_{RR} p_{ra}(t)dt \tag{3.25}$$

y_m	α_m	β_m	γ_m	τ_m
HR/HR^0	1	1	1	5
$E_{lv/rv,max}/E^0_{lv/rv,max}$	1	-	0.5	5
$R_{i,art/cap}/R^0_{i,art/cap}$	4	-	-1	10
$C_{i,ve/v}/C^0_{i,ve/v}$	-1	-	1.5	30
$V^{un}_{i,ve/v}/V^{un,0}_{i,ve/v}$	-1	-	1.5	30

Table 3.1: Baroreflex Parameters

y_m	$\alpha_{cp,m}$	$\beta_{cp,m}$	$\gamma_{cp,m}$	$\tau_{cp,m}$
$R_{cp,i,art/cap}/R^0_{cp,i,art/cap}$	2.5	-	-0.25	10
$C_{cp,i,ve/v}/C^0_{cp,i,ve/v}$	-0.8	-	1.4	30
$V^{un}_{cp,i,ve/v}/V^{un,0}_{cp,i,ve/v}$	-0.8	-	1.4	30

Table 3.2: Cardiopulmonary reflex parameters

where $\bar{p}_{cp}$ states for cardiopulmonary pressure. When $\bar{p}_{cp}$ falls below or raises above a target value, $\bar{p}_{cs,tg} = 7.02$ mmHg, sympathetic and parasympathetic activities are triggered. As for the baroreceptor model, these two activities are governed by:

$$n_{s,cp}(\bar{p}_{cp}) = \frac{1}{1 + \left(\frac{\bar{p}_{cp}}{\bar{p}_{cp,tg}}\right)^{\nu}} \qquad n_{p,cp}(\bar{p}_{cp}) = \frac{1}{1 + \left(\frac{\bar{p}_{cp}}{\bar{p}_{cp,tg}}\right)^{-\nu}} \tag{3.26}$$

where $\nu = 7$. Efferent organ control equation used in arterial baroreflex (eq. 3.24) applies also to cardiopulmonary reflex, but only for $R_{art/cap}$, $V^{un}_{ve/v}$ and $C_{ve/v}$. Table 3.2 reports parameters $\alpha_{cp,m}$, $\beta_{cp,m}$ and $\tau_{cp,m}$ for the cardiopulmonary reflex.

Cerebral autoregulation - ensuring constant cerebral blood flow (CBF) to the human brain via cerebral vessel vasoconstriction/dilation - is implemented into the cerebrovascular model. The scope of the model is to modify cerebral pial arteriolar compliances and resistances as non-linear function of the mismatch between the current local blood flow (fractions of the overall CBF) and a given reference values taken as target. For a more detailed discussion, see [10].

3.4 Numerical methods

In order to obtain time signals of all dependent unknowns at any point throughout the 1D domain (vessels cross section area $A(x,t)$, blood flow rate $Q(x,t)$, blood pressure $p(x,t)$) as well as in all 0D compartments ($Q(t)$, $p(t)$, but also blood volume $V(t)$), suitable numerical schemes shall be adopted to discretize partial (from 1D model) and ordinary (from 0D counterpart) derivative equations introduced, in order to obtain approximated numerical solutions.

Partial differential equations (PDE) 3.1 describing blood motion throughout the 1D arterial tree - including all 63 large 1D arteries - are discretized according to a Discontinuous Galerkin Finite Elements approach. Eq. 3.1 is written in the conservative form

$$\frac{\partial \mathbf{U}}{\partial t} + \frac{\partial \mathbf{F}}{\partial x} + \mathbf{S} = 0, \tag{3.27}$$

where $\mathbf{U} = (A, Q)^T$ is the vector of conservative variables, while $\mathbf{F} = \mathbf{F}(\mathbf{U})$ is the flux vector and $\mathbf{S}$ is the source term vector:

$$\mathbf{F} = \begin{pmatrix} Q \\ \beta \frac{Q^2}{A} + \sum_{j=2}^{4} \frac{(j-1)A^j B_j}{j\rho} - B_5 \sqrt{A} \frac{\partial Q}{\partial x} - \hat{E} I \frac{A}{\rho} \left(\frac{A_b^m}{A^m} - 1 \right) + \frac{A}{\rho} p_b \end{pmatrix} \tag{3.28}$$

$$\mathbf{S} = \begin{pmatrix} 0 \\ \sum_{j=1}^{4} \frac{dB_j}{dx} + \frac{B_5}{\rho\sqrt{A}} \frac{\partial A}{\partial x} \frac{\partial Q}{\partial x} + \frac{\hat{E} I}{\rho} \left(\frac{A_b^m}{A^m} - 1 \right) \frac{\partial A}{\partial x} - \frac{p_b}{\rho} \frac{\partial A}{\partial x} - N_4 \frac{Q}{A} - A_g \sin\gamma \sin\alpha \end{pmatrix} \tag{3.29}$$

Then, the weak formulation of the conservative equation 3.27 is written by introducing the test function $\psi(x)$

$$\left(\frac{\partial \mathbf{U}}{\partial t}, \psi \right)_\Omega + \left(\frac{\partial \mathbf{F}}{\partial x}, \psi \right)_\Omega + (\mathbf{S}, \psi)_\Omega = 0, \tag{3.30}$$

where with Ω the domain of integration has been denoted (i.e., each element of the spatial discretization). Then, integrating by parts

$$\int_\Omega \frac{\partial \mathbf{U}}{\partial t} \psi, d\Omega + [\mathbf{F}(\mathbf{U})\psi]_{\partial\Omega} - \int_\Omega \mathbf{F}(\mathbf{U}) \frac{d\psi}{dx} \, d\Omega + \int_\Omega \mathbf{S}\psi \, d\Omega = 0 \tag{3.31}$$

which will be integrated over each element of the spatial discretization (details on the spatial discretization of the 1D arterial network are reported in [10]) and where $\partial\Omega$ identifies the boundary of the domain Ω and $[\mathbf{F}(\mathbf{U})\psi]_{\partial\Omega}$ are evaluated on each element boundaries through Lax-Friedrichs approximation for internal boundaries between adjacent elements or via the method of characteristics for external boundaries.
A piece-wise linear representation (through lagrangian polynomials) is adopted, approximating thus $A \approx A_1\phi_1(\xi) + A_2\phi_2(\xi)$ and $Q \approx Q_1\phi_1(\xi) + Q_2\phi_2(\xi)$ et each element, with shape functions $\phi_1(\xi)$ and $\phi_2(\xi)$ defined as the lagrangia functions:

$$\phi_1(\xi) = \frac{1-\xi}{2}, \qquad \phi_2(\xi) = \frac{1+\xi}{2} \tag{3.32}$$

where ξ is the normalized coordinate of each single element of the piece-wise representation.
Taking then the test function $\psi = (\psi_1, \psi_2)$ as identical to the shape functions ϕ_1 and ϕ_2 defined above, form 3.31 can be re-arranged as

$$\frac{\partial \mathbf{Y}_{1D}}{\partial t} = \mathbf{M}\mathbf{G}, \tag{3.33}$$

where $\mathbf{Y}_{1D}$ is the matrix of area and flow rate weights at elements nodes, $\mathbf{M}$ is the mass matrix and $\mathbf{G}$ is the known term matrix. For the definitions of these matrices refer to [10].

System 3.33 together with all ordinary differential equations governing 0D model compartments and short-term regulation mechanisms are integrated in time according to a 2-step Runge-Kutta time marching scheme. That is, given $\mathbf{f}$ the generic state vector containing all time-marching variables (belonging to 1D, 0D and short-term control models), time integration is performed in two separate half-steps, according to the following scheme:

- first half-step, from $\mathbf{f}^n$ at time t^n to $\mathbf{f}^{n+\frac{1}{2}}$ at time $t^{n+\frac{1}{2}}$:

$$\mathbf{f}^{n+\frac{1}{2}} = \mathbf{f}^n + \frac{\Delta t}{2}\frac{d\mathbf{f}^n}{dt} \tag{3.34}$$

- second half-step, from $\mathbf{f}^n$ at time t^n to $\mathbf{f}^{n+1}$ at time t^{n+1}, exploiting the state vector $\mathbf{f}^{n+\frac{1}{2}}$ previously integrated at time $t^{n+\frac{1}{2}}$:

$$\mathbf{f}^{n+1} = \mathbf{f}^n + \Delta t\frac{d\mathbf{f}^{n+\frac{1}{2}}}{dt} \tag{3.35}$$

Chapter 4

Lower Body Negative Pressure: operation and modeling

In this chapter, we will provide a deeper insight in the Lower Body Negative Pressure (LBNP) device, its various fields of application and the related physiological effects. In the final section, we will focus on how this device has been incorporated into numerical models of the cardiovascular system.

4.1 Physiological effects induced by LBNP

Lower Body Negative Pressure decreases venous return to the heart by promoting blood pooling in the lower regions of the body, with the distinction between "upper" and "lower" body determined by the location of the seal. This induced central hypovolemia triggers a hypotensive activation of both arterial and cardiopulmonary baroreflexes, leading to neurohumoral responses that increase heart rate and promote vasoconstriction. These mechanisms work together in a compensatory effort to maintain arterial pressure and ensure sufficient cerebral perfusion. A summary of the mechanical and physiological effects of LBNP is presented in Fig. 4.1.
Conversely, the cessation of LBNP produces effects similar to those observed during a Valsalva maneuver: blood redistributes to the thorax, resulting in a transient rise in blood pressure and a subsequent reduction in heart rate [12]. We will now provide a more detailed description of the effects induced by LBNP on various physiological systems.

From a cardiovascular perspective, LBNP elicits two primary effects: (1) biophysical changes due to the reduction in central circulating blood volume, affecting pressure-flow dynamics, and (2) compensatory responses triggered by neuroendocrine reflex mechanisms. Regarding the first effect, chamber decompression shifts blood from the central circulation to the lower body, below the iliac crest, as evidenced by a proportional increase in leg volume. This redistribution leads to a decrease in cardiac filling pressure, a reduction in left ventricular end-diastolic volume ($LVED$), and subsequent declines in stroke volume and cardiac output. The reduction in mean arterial pressure caused by LBNP activates compensatory responses mediated by neuroendocrine reflex mechanisms. These responses are facilitated by both parasympathetic (cardiac vagal) and sympathetic nervous system activity. The drop in arterial blood pressure stimulates baroreceptors in the aorta and carotid arteries, initiating a vagal withdrawal to in-

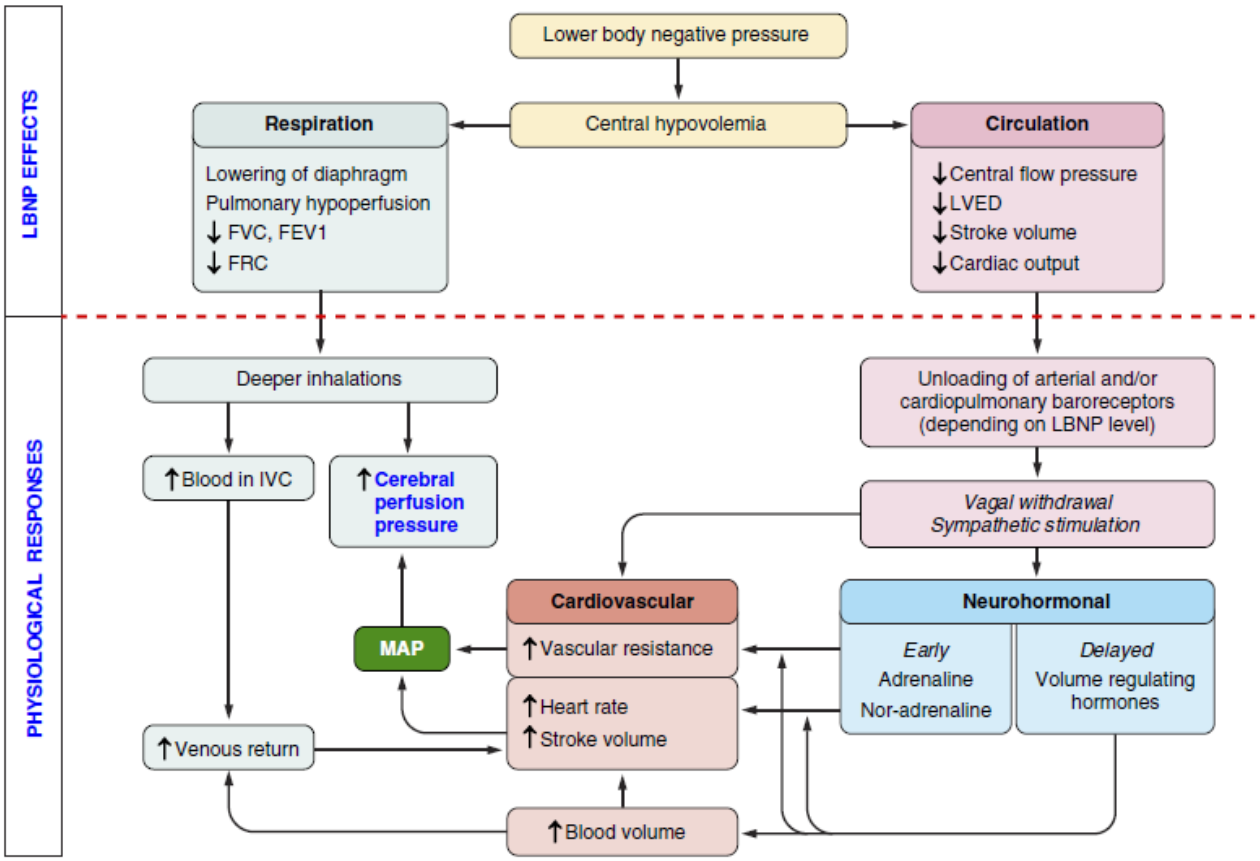

Figure 4.1: Overview of mechanical effects and physiological responses of lower body negative pressure (LBNP) [12]. FVC, forced vital capacity; $FEV_{1.0}$, forced expiratory volume in 1 s; FRC, functional residual capacity; LVED, left ventricular end-diastolic volume; IVC, inferior vena cava; MAP, mean arterial pressure.

crease heart rate.

In addition to the modest decrease in arterial blood pressure, reduced venous return during LBNP is reflected in a drop in central venous pressure (CVP). This lowered CVP has been shown to trigger sympathetic vasoconstriction. The activation of cardiopulmonary and carotid baroreceptors due to unloading is responsible for the increase in peripheral vascular resistance during LBNP exposure. This mechanism creates a feedback loop in blood pressure regulation: as blood pressure decreases, the receptors sense the change and activate both sympathetic and parasympathetic responses in order to counteract the changes. The synchronized oscillatory sympathetic control of blood pressure represents a protective compensatory mechanism, ensuring adequate oxygenation of the brain and peripheral tissues during prolonged LBNP. If this regulatory coupling is disrupted, the ability to maintain blood pressure is also compromised.

Regarding cerebral blood flow (CBF), measurements of middle cerebral artery blood velocity during progressive LBNP confirm the well-established observation [13] that LBNP leads to a reduction in CBF.

The application of LBNP also impacts pulmonary function [14]. It causes a downward shift of the diaphragm, leading to pulmonary hypoperfusion, while simultaneously increasing forced

vital capacity (FVC), forced expiratory volume in 1 second ($FEV_{1.0}$), and functional residual capacity, without affecting pulmonary compliance. These functional changes are attributed to a decrease in thoracic blood volume, resulting from the shift of fluid from the thoracic region to the lower body. This redistribution reduces the resistance caused by circulating pulmonary blood volume, allowing for faster air movement. Additionally, the deeper inhalations associated with increased tidal volume activate the "respiratory pump," which results in a more significant reduction in intrathoracic pressure (creating a stronger vacuum), thereby enhancing blood flow in the inferior vena cava and improving venous return.
Another important consideration when applying LBNP is its impact on blood coagulation [15]. Conditions that lead to increased bleeding, such as trauma or vessel rupture, are often linked to a rise in thrombosis, which in turn helps reduce the risk of exsanguination. LBNP-induced central hypovolemia leads to hemoconcentration, along with increases in plasma proteins and blood viscosity, all of which contribute to a prothrombotic state and enhanced coagulation.
Additionally, LBNP elicits a hormonal response to the central hypovolemia [12]. This includes a rapid rise in plasma levels of epinephrine and norepinephrine, followed by activation of the renin-angiotensin system after a delay of 10 to 20 minutes, leading to increased plasma renin activity, angiotensin II, and aldosterone levels.

4.2 Applications of LBNP

As previously mentioned, LBNP is utilized as a countermeasure during spaceflight to simulate gravitational stress, helping to mitigate certain pathologies associated with prolonged exposure to microgravity (0G), such as SANS and orthostatic intolerance prior to re-entry [9]. By replicating gravitational stress during extended periods of microgravity, LBNP helps maintain the body systems that have evolved under 1G and prevents maladaptive adaptations to microgravity, such as cerebral and ocular remodeling, which can occur upon return to Earth. Pathologies linked to fluid redistribution in 0G are particularly likely to be alleviated by regular exposure to simulated gravitational stress via LBNP. These include orthostatic intolerance, SANS, venous thrombosis, cardiovascular degradation, and musculoskeletal deconditioning.
Starting with SANS, as discussed in Chapter 2.3, one of the possible primary contributors is the slow, chronic cerebral and ocular fluid shift and pressure overload resulting from the systemic cephalad fluid shift in weightlessness. The efficacy of LBNP in mitigating SANS stems from its ability to counteract cephalad fluid shifts, which could help reduce increases in intracranial pressure (ICP), ocular pressure IOP/ICP mismatch, and/or cerebral remodeling [9]. However, we must not forget that the mechanism underlying SANS pathology has not yet been fully understood. In addition to the previously mentioned potential causes, Hall et al. [16] do not rule out a dependence on the increase in ocular perfusion pressure (OPP) under microgravity conditions, rather than on the difference between intraocular pressure and intracranial pressure (translaminar pressure gradient, $TLP = IOP - ICP$). In this study, it was shown that OPP is not significantly reduced by the application of LBNP, making the device ineffective against SANS if such a dependence were confirmed. Many questions about this pathology remain unanswered, which, moreover, represents one of the main obstacles to long-term stays in microgravity. The next steps in research must focus on identifying the cause of SANS; only then will it be possible to determine the most effective countermeasure.

Continuing with other spaceflight-related pathologies against which LBNP has demonstrated efficacy, studies [9] have shown that LBNP at low negative pressure (-10 mmHg) for one hour can help mitigate cardiovascular deconditioning. Specifically, LBNP has been found to reduce central venous pressure without significantly affecting blood pressure or heart rate. This suggests that LBNP can activate normal baroreceptor reflexes without causing excessive physiological stress on the cardiovascular system. Therefore, LBNP may help counteract venous pooling, reduce plasma loss, and activate the baroreflex response, thus mitigating orthostatic intolerance and limiting cardiovascular deconditioning.
In microgravity, crew members experience persistent cerebral venous congestion, which can lead to stagnant venous blood flow and increase the risk of thrombosis. By inducing a blood shift from the upper to the lower part of the body, LBNP can acutely improve blood flow in the jugular veins, restore normal venous hemodynamics, and reduce the risk of thrombosis [17].
Since LBNP effectively simulates gravity in a 0G environment, combining it with treadmill exercise has been proposed [18] to recreate gravity-like conditions, providing the necessary load for the musculoskeletal and cardiovascular systems and reducing musculoskeletal deconditioning.
What has been outlined so far represents only a part of the potential applications of LBNP. Lower Body Negative Pressure is also used for a wide range of cardiovascular and musculoskeletal applications on Earth. Goswami et al [12] reported a wide range of terrestrial applications of LBNP, including its use as a research tool, a training device, and clinical equipment. As a research tool, LBNP offers a noninvasive method to study hemodynamic responses associated with blood loss, making it particularly valuable in emergency and military medicine, where acute hemorrhagic shocks are a critical concern. Additionally, LBNP in seated subjects has been employed to examine the relative contributions of low and high pressure receptors to arginine vasopressin release, an insight relevant to understanding and managing heart failure. On Earth, LBNP combined with treadmill exercise has been used not only to protect against orthostatic deconditioning during head-down tilt bed rest but also to enhance muscle strength, spinal function, and bone metabolism. These effects suggest potential applications in orthopedic rehabilitation and in countering balance and postural changes caused by prolonged bedrest confinement. Furthermore, LBNP serves as a reliable tool for assessing lower limb venous compliance by measuring LBNP-induced changes in lower leg volume using specialized strain gauges placed around the calf muscle. As a training device, LBNP proves invaluable for various applications. For instance, it offers a less stressful alternative to centrifugation for screening pilots while still providing insights into physiological responses. It is also useful for studying the impact of environmental stressors, such as whole-body heating during LBNP sessions, which mimics the challenges faced by military personnel standing in hot climates.
We shall now consider some aspects regarding the application of LBNP. When discussing Lower Body Negative Pressure, it is crucial to specify the protocol used: the duration of device application, its intensity and the posture of the patient are all variables that play a significant role in determining the hemodynamic and neurohormonal responses. Another key aspect to consider is that the intensity of LBNP induces different patterns of blood redistribution within the body, leading to varying activation of baroreceptors and cardiopulmonary reflexes. Depending on the level of LBNP applied, different effects are observed on these receptors and thus different response are activated. Finally, it is important to note that the response of the body to LBNP is also influenced by the position of the device seal. Typically, this junction is positioned at

the iliac region, but it can also be placed higher, in the abdominal region. This placement affects the degree of central volume reduction and the associated variation in heart rate (HR). All these factors must be taken into account whenever a test involving Lower Body Negative Pressure is conducted.

4.3 Review of the numerical implementations of LBNP

Since the objective of this thesis is the numerical implementation of LBNP within a 0D-1D multiscale model, we will now review the strategies adopted in various studies. In Section 4.4 we will apply these modeling approaches to our cardiovascular model in order to numerically implement the device.

Heldt et al. [19] developed a zero-dimensional model of the cardiovascular system to investigate the short-term physiological response to the application of Lower Body Negative Pressure and a Head-Up Tilt test. The peripheral circulation was divided into the upper body, renal, splanchnic, and lower body regions. The inferior and superior venae cavae were modeled as separate compartments. This resulted in a model comprising 12 compartments, each represented using a hydraulic-electrical analogy. Specifically, linear resistances were used to model inflow and outflow resistances, while capacitors (linear, nonlinear, or time-varying) represented vessel compliance, reflecting their capacity to distend and accommodate blood pooling. Governing equations included the continuity equation, the momentum conservation equation, and a constitutive law linking intravascular pressure to the blood volume within a vessel. This constitutive relationship was nonlinear for the splanchnic, lower limb, and abdominal venous regions. The LBNP was implemented in the lower limb region by introducing a negative extravascular pressure equal to the LBNP-induced pressure into the definition of the transmural pressure in the fundamental equations. Observations showed that blood pooling occurred not only in the legs but also in the pelvic region. To account for this, a reduced extravascular pressure (lower than that applied to the legs) was added to the abdominal venous compartment. Moreover, the increased hydrostatic pressure gradient across the microcirculation in the lower body and abdominal venous compartments, due to the LBNP, leads to fluid absorption from the vascular to the interstitial space. The study also simulated this plasma reduction by introducing a volume variation dependent on the LBNP pressure and the duration of its application.

Similarly, Gerber et al. [20] utilized a zero-dimensional mathematical model of the cardiovascular system to analyze the short-term response to gravitational unloading. This lumped-parameter numerical model incorporated LBNP and interstitial fluid exchange. It consisted of 21 Windkessel units within a closed-loop system. Each unit comprised two elements: a resistor and a capacitor. In this analogy, pressure corresponded to voltage, and blood flow to electrical current. A constitutive pressure-volume relationship was necessary, which was linear for most arterial compartments but nonlinear for the venous compartments of the legs. Gravitational changes caused disturbances in intravascular hydrostatic pressure, triggering transcapillary fluid exchange, particularly in the upper and lower extremities. To capture this exchange, the electrical compartments for the arms and legs were modified by splitting the resistor into pre- and post-capillary components. LBNP was implemented in the model by introducing a step reduction in external and interstitial pressure to constant negative values across all leg vessels, including arterial, capillary and venous compartments.

Kappel et al. [21] focused on the interplay between various short-term responses triggered by receptors —such as systemic resistance variations, venous dead volumes, venous compliance, heart rate, and cardiac chamber contractility — when the body is subjected to orthostatic stress induced by LBNP. Their numerical model, also zero-dimensional, consisted of six vascular compartments and was formulated using a set of nonlinear ordinary differential equations, auxiliary equations, and an optimal control mechanism. Two cases of LBNP application were studied: one with the seal placed at the iliac level and the other at the rib level. The LBNP was incorporated into the continuity equations of the model as an additional pressure term applied to both arterial and venous compartments of the lower extremities. In the rib-level seal scenario, it was also applied to the splanchnic region compartments. Furthermore, the application of LBNP-induced pressure was gradual over time, following an increasing function within a specified time interval. The long-term reduction in blood volume caused by LBNP stress was modeled using an exponential decay law for total blood volume.
In contrast to the previously mentioned purely zero-dimensional studies, Peterson et al. [22] developed a multiscale zero- and one-dimensional model of the cardiovascular system. The arterial tree was modeled with 36 major arteries, some representing fifth-generation branches of large parent vessels, including eight pairs of symmetric arteries. These 1D vessels were simulated as tapered tubes of varying lengths, with unidirectional axial blood flow. Governing equations for this 1D part included the continuity equation, the momentum equation, and a nonlinear constitutive equation relating vessel cross-sectional area to transmural pressure. The system yielded three variables: vessel cross-section, intraluminal pressure, and flow along each vessel's axis. This 1D model spanned arteries from the upper body (e.g., carotids) to those in the legs (e.g., anterior and posterior tibial arteries). The zero-dimensional component was developed using the hydraulic-electrical analogy (as in the previously discussed studies), employing a lumped-parameter Windkessel model. Venous systemic circulation (divided into cranial, central, and caudal regions), pulmonary circulation, and the heart (right and left ventricles) were represented as electrical circuits with resistors to model arteriolar resistance and capacitors to capture total peripheral compliance. For venous regions, constant extravascular pressures independent of posture were introduced: 5 mmHg for cranial regions (intracranial pressure), 8 mmHg for central regions (simulating combined intrathoracic and abdominal expiratory pressures), and 10 mmHg for caudal regions (representing intramuscular pressure). Impedances linked the 1D and 0D components. Hydrostatic pressure was included along the head-to-foot axis in all areas except arteries, where low compliance precluded significant fluid shifts. The study aimed to analyze how intrathoracic and intraventricular hydrostatic pressures influence cardiac function under different configurations (supine, seated, launch at 0, 1, and 1.8 G). The effect of the LBNP on hemodynamic parameters was simulated to assess its efficacy in mitigating post-flight orthostatic stress. LBNP was implemented as a -40 mmHg extravascular pressure applied only to the caudal venous region.

4.4 LBNP mathematical modeling

The last multiscale model presented [22] closely resembles the one adopted and extended in this thesis. Our model, in fact, is also a 1D-0D multiscale model, characterized by several vessels (63 arteries) belonging to the arterial tree (1D) and 5 zero-dimensional macro-regions, namely

the legs, lower abdomen, upper abdomen, arms, and head, each of which is subdivided into arteriolar, capillary, venular, and venous compartments (Chapter 3). To implement the device within the model, we proceeded in a manner similar to what has been done in the literature. Regarding the one-dimensional part, the extravascular pressure term of the Lower Body Negative Pressure (p_{LBNP}) was included in the constitutive equation that relates the intraluminal pressure to the cross-sectional area of the vessel. We recall this equation

$$p^t = p = B_1 + B_2 A + B_3 A^2 + B_4 A^3 - B_5 \frac{1}{\sqrt{A}} \frac{\partial Q}{\partial x} - \hat{E} I \left(\left(\frac{A_b}{A} \right)^m - 1 \right) + p_b \tag{4.1}$$

where p represents the intraluminal pressure inside the vessel, while p^t represents the transmural pressure, which up to this point were the same due to the fact that the extravascular pressure was assumed to be zero. Now, the application of Lower Body Negative Pressure creates an extravascular depression on the legs, modifying equation (4.1) to become

$$p^t = p - p_{LBNP} = B_1 + B_2 A + B_3 A^2 + B_4 A^3 - B_5 \frac{1}{\sqrt{A}} \frac{\partial Q}{\partial x} - \hat{E} I \left(\left(\frac{A_b}{A} \right)^m - 1 \right) + p_b \tag{4.2}$$

or equivalently

$$p = B_1 + B_2 A + B_3 A^2 + B_4 A^3 - B_5 \frac{1}{\sqrt{A}} \frac{\partial Q}{\partial x} - \hat{E} I \left(\left(\frac{A_b}{A} \right)^m - 1 \right) + p_b + p_{LBNP} \tag{4.3}$$

This additional term is only present in the arteries of the legs, specifically from the common iliac artery (vessel 42) to the posterior tibial artery (vessel 48). These vessels are the ones that, if we wish to simulate the application of LBNP with a belt on the hips, are included in the LBNP chamber. The depression applied by the device follows a cosine wave over time ($p_{LBNP} = p_{LBNP}(t)$), gradually reaching a maximum depression value induced by the device over a time interval ($5\,s$). This maximum value is then held constant throughout the simulation. From a spatial point of view, the application of the external pressure follows a step function, meaning it is zero up to the abdominal aorta (vessel 41) and then increases to p_{LBNP} from the entrance to vessel 42 (common iliac artery). Thus, the function p_{LBNP} is a function of time only, and does not influence the celerity calculations for compatibility boundary conditions (Chapter 3.1.1 and Appendix A.2).
During the study and the evaluation of the best numerical strategy to adopt, the case where LBNP is applied only to a segment of the arterial tree of the lower limbs, specifically to the common iliac artery (vessel 42) and its two child vessels (vessels 43 and 44), was also analyzed. The motivations and results of this choice will be discussed extensively in Chapter 5; for now, let us focus on its numerical aspect. Indeed, unlike the case where the effect of the device impacts all the 1D vessels of the legs, here equation (4.3), which includes the p_{LBNP} term, is applied only to vessels 42, 43, and 44. Additionally, the external pressure value is reached gradually, not only over time (as in the previous case) but also spatially, with a spatial gradient of external pressure developing along the last section of the abdominal aorta (vessel 41) and the first section of the child vessels of artery 44, i.e., the 45 and 46 femoral arteries. The fact that the LBNP pressure is now also a function of space ($p_{LBNP} = p_{LBNP}(t, x)$) introduces this term into the definition of celerities (eq. 3.7), and thus into the compatibility boundary conditions.

We now shift our focus to the zero-dimensional component of the model. We recall the two fundamental conservation equations of mass

$$\frac{dV_{i,j}}{dt} = Q_{i,j-1} - Q_{i,j} \tag{4.4}$$

and momentum

$$\frac{dQ_{i,j}}{dt} = \begin{cases} \frac{p_{i,j}+\Delta p_{h,i,j}-R_{i,j}Q_{i,j}-p_{i,j+1}}{L_{i,j}}, & \text{if } j \in \{v, \text{svc}, \text{ivc}, \text{avc}\}, \\ \frac{p_{i,j}-R_{i,j}Q_{i,j}-p_{i,j+1}}{L_{i,j}}, & \text{if } j \in \{\text{art}, \text{cap}, \text{ven}\}. \end{cases} \tag{4.5}$$

where, as a reminder, the subscript i indicates the body region (*H, A, UA, LA, L*), while the subscript j refers to the type of compartment (arterioles, capillaries, venules, veins, superior vena cava, inferior vena cava, and abdominal vena cava). The intraluminal pressure of the (i,j)-th compartment is denoted by $p_{i,j}$, the flow rate by $Q_{i,j}$, while $R_{i,j}$ and $L_{i,j}$ are the hydraulic resistance and inertance, respectively. The constitutive relationship linking pressure and volume has been added to these equations, namely

$$V_{i,j} = V_{i,j}^{\text{un}} + p_{i,j}^{t} C_{i,j} = V_{i,j}^{\text{un}} + \left(p_{i,j} - p_{i,j}^{\text{ext}}\right) C_{i,j} \tag{4.6}$$

from which we can derive the equation for the intraluminal pressure of the (i,j)-th compartment

$$p_{i,j} = \frac{V_{i,j} - V_{i,j}^{\text{un}}}{C_{i,j}} + p^{\text{ext}} \tag{4.7}$$

In our case, the extravascular pressure in the compartments of the legs is exactly the pressure applied by the LBNP, i.e., $p_{i,j}^{\text{ext}} = p_{\text{LBNP}}$, which is a function of time following a cosine law, but not of space. The system that needs to be solved to find pressure, volume, and flow rate in the compartments of the leg region will therefore be

$$\begin{cases} \frac{dV_{i,j}}{dt} = Q_{i,j-1} - Q_{i,j}, \\ \frac{dQ_{i,j}}{dt} = \frac{p_{i,j}+\Delta p_{h,i,j}-R_{i,j}Q_{i,j}-p_{i,j+1}}{L_{i,j}}, \\ p_{i,j} = \frac{V_{i,j}-V_{i,j}^{\text{un}}}{C_{i,j}} + p_{\text{LBNP}}. \end{cases} \tag{4.8}$$

Alternatively, a second approach, quite analogous, can be followed, where the constitutive relationship is written in the form $V_{i,j} = V_{i,j}(p_{i,j})$ and the other two necessary equations are the time derivative of the flow rate and the pressure (which will also contain the derivative of p^{LBNP} as it depends on time)

$$\begin{cases} \frac{dp_{i,j}}{dt} &= \frac{1}{C_{i,j}}\left(Q_{i,j-1} - Q_{i,j}\right) + \frac{dp_{\text{LBNP}}}{dt}, \\ \frac{dQ_{i,j}}{dt} &= \frac{p_{i,j}+\Delta p_{h,i,j}-R_{i,j}Q_{i,j}-p_{i,j+1}}{L_{i,j}}, \\ V_{i,j} &= V_{i,j}^{\text{un}} + \left(p_{i,j} - p_{\text{LBNP}}\right) C_{i,j}. \end{cases} \tag{4.9}$$

Clearly, for the venous compartment of the legs (subscript L,v), the constitutive equation between pressure and volume remains nonlinear, as seen previously, and thus maintains the form

$$V_{L,v} = V_{L,v}^{\text{un}} + \frac{2\Delta V_{\max}}{\pi} \arctan\left(\frac{\pi C_{L,v}}{2\Delta V_{\max}}\left(p_{L,v} - p_{\text{LBNP}}\right)\right). \tag{4.10}$$

In conclusion, the introduction of LBNP in the 0D part of the model involves the addition of the p_{LBNP} term within the constitutive relation for all the compartments (arterioles, capillaries, venules, and veins) of the legs. The abdominal vena cava (and therefore also the inferior vena cava) was considered outside the zone of application of the device, and thus its corresponding extravascular pressure is zero. The results of the LBNP implementation on all zero-dimensional compartments of the legs will be discussed in Chapter 5, but we will also analyze the case where the action of the device is considered only on the venous compartment of the lower limbs.

Chapter 5

Numerical testing and model selection

After detailing the implementation of the LBNP within the multiscale model, we now proceed to analyze the response of the system by applying the device separately to different components of the model. The aim of this process is to identify the most effective numerical strategy for simulating the impact of Lower Body Negative Pressure on the cardiovascular system. In the following two sections, we will discuss the results obtained from various numerical configurations and subsequently determine the optimal strategy to adopt.

5.1 Numerical testing for the LBNP implementation

Six tests have been conducted to gain a clearer understanding of the most suitable numerical approach for modeling the effects associated with the LBNP device. In this context, the first two configurations analyzed involved applying the LBNP exclusively to the entire zero-dimensional model (1) — namely, all the vascular compartments of the leg region (arterioles, capillaries, venules, and veins), as described in Chapter 4.4 — and subsequently applying it exclusively to the one-dimensional model (2) (as described in Chapter 4.4). This comparison enables the distinction between the effects attributable to the 0D component of the model and those driven by its 1D counterpart.
Additionally, two further simulations were conducted, considering the effect of LBNP applied only to a section of the arterial tree in the legs (3), specifically to the common iliac artery (vessel 42) and its two daughter vessels (vessels 43 and 44). Considering that the various vessels in the legs are all in series with respect to the common iliac artery, as they are all its daughter of different orders, simulation (3) was conducted to assess the effect of involving a single 1D vessel on the subsequent ones. Furthermore, vessels 42 and 44 are, in our model, distant from the zero-dimensional terminations, making the comparison between this test and the one where the device is applied to all the leg arteries (2) valuable for understanding the effect of the interface between the 0D and 1D parts.
A second test was performed by applying the device solely to the venous compartment of the zero-dimensional leg model (4). This simulation was carried out considering that the veins are characterized by the highest distensibility and are therefore more sensitive to changes in extravascular pressure. Moreover, the other zero-dimensional compartments are arranged in series with respect to the veins, leading us to hypothesize that the effect on the veins would also be felt upstream (venules, capillaries, etc.) and downstream (abdominal vena cava).

These four configurations were then compared to the most comprehensive case (5), in which the extravascular pressure induced by the LBNP is applied to the entire arterial tree of the legs (vessels 42, 43, 44, 45, 46, 47, and 48) as well as to all the 0D compartments of the lower limbs (veins, venules, capillaries, and arterioles). This configuration is expected to be the closest to reality, where all major arterial and venous vessels, along with the microcirculation of the lower limbs, are exposed to the device chamber.
A final test was performed (6), considering the device acting on all the 1D vessels of the legs as well as on the 0D section, but this time limited to the venous compartment.
These six simulations were conducted under a depressure induced by LBNP, set to $p_{LBNP} = -40\,\text{mmHg}$, to observe the response of the system to significant stress. The subject is positioned supine, with the lower limbs placed inside the Lower Body Negative Pressure device up to the iliac region. Furthermore, the regulatory mechanisms, namely baroreceptors, cardiopulmonary reflex, and cerebral autoregulation, were deactivated. This approach aimed to isolate the purely hemodynamic effects and thereby identify the most appropriate modeling strategy. The characteristics of these simulations are summarized in the Table 5.1.

Posture	Supine
LBNP	-40 mmHg
$t_{i\,LBNP}$	50 s
$\Delta t_{transient}$	5 s
Regulatory mechanisms	off

Table 5.1: Simulation parameters for the LBNP application on the model. $t_{i\,LBNP}$ is the initial time for LBNP application, while $\Delta t_{transient}$ is the time interval needed to reach the maximum depression$p_{LBNP\,max} = -40\,\text{mmHg}$.

We now present some significant results obtained. We begin by examining the trends in mean pressures at the level of the aortic root (Fig. 5.1). It is important to recall that the regulatory mechanisms are deactivated; therefore, in the absence of the chronotropic effect, a reduction in central pressure is expected since the Lower Body Negative Pressure is applied.
The results reveal a decrease of about -30% in mean pressure for the cases where LBNP is applied exclusively to the zero-dimensional part of the model (both in the simulation involving only the venous compartment and in the case where all 0D compartments are included). Conversely, the test where the device is applied only to the one-dimensional counterpart shows that the pressure either remains steady or slightly increases (6%) when all the 1D vessels of the legs are involved. Simulations in which LBNP is applied to both the 0D and 1D components of the model (indicated by the blue and light blue curves) exhibit a reduction of about -27% in pressure, although to a lesser extent compared to the cases where only the 0D part is considered. This suggests that the reduction is predominantly driven by the zero-dimensional part of the model. This initial result highlights how the high compliance and deformability of the vessels in the 0D compartments make them more sensitive to the action of the device, leading to a reduction in central pressure when baroreceptors are deactivated.
We now turn our attention to the common iliac artery 42 (Fig. 5.2). Simulations involving actions solely on the 0D compartments (either on all compartments or exclusively on the veins) exhibit a mean pressure that decreases from 91 mmHg under pre-LBNP conditions to approximately 62 mmHg following the application of the device. This value closely aligns with

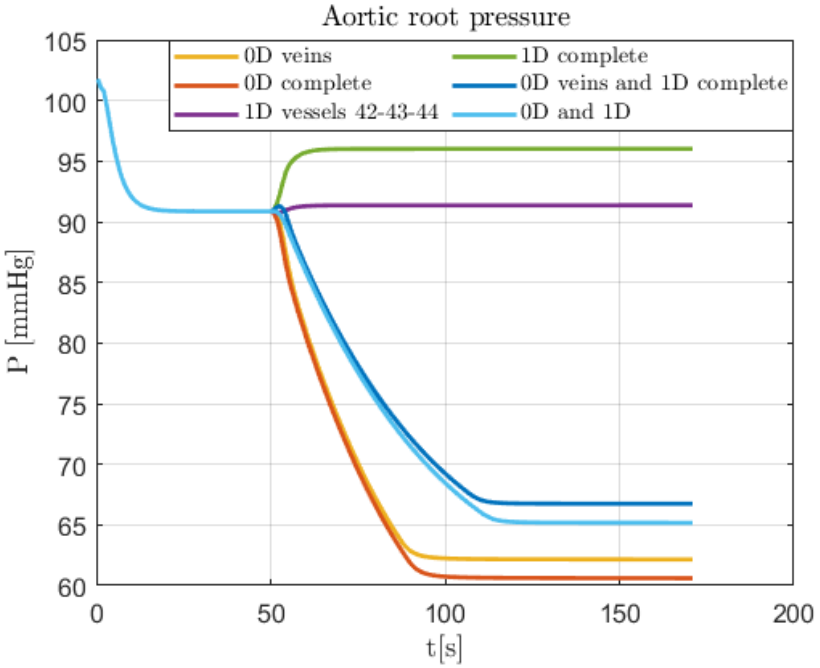

Figure 5.1: Aortic root pressure.

that observed at the aortic root, indicating that, as the subject is in a supine position and the device is applied only to the 0D section, the mean pressure in the 1D vessels of the legs remains consistent with central values. However, it is important to note that these central pressures are reduced compared to the baseline supine condition without the application on LBNP due to the suppression of regulatory mechanisms. This aspect will be further elaborated upon later. In cases where the device is applied to all vessels in the unidimensional section (green curve), a pressure reduction of 35 mmHg is observed. This outcome is attributable to the external pressure being lowered by 40 mmHg. Since the vessel walls possess a certain stiffness (which, as noted, increases along the arterial tree toward the extremities), only a fraction of this external pressure is transmitted inside the vessel. We expect that this pressure reduction will be maintained across all 1D vessels of the legs, extending to the tibial arteries, given that the subject remains in a supine position and p_{LBNP} is applied to the entire arterial tree of the lower limbs. Proceeding towards the lower extremities of the organism, let us focus on the femoral artery 46 (Fig. 5.3). It becomes immediately evident that, in the zero-dimensional model (both in the simulation involving only the veins and in the full simulation), there is consistently a 31% reduction in mean pressure compared to the supine baseline value in the absence of LBNP. This confirms the result previously observed for the iliac artery.

The simulation results for the scenario where LBNP is applied to all 1D vessels in the legs show a further decrease in mean pressure compared to the iliac artery. In fact, a reduction of 35 mmHg was observed in vessel 42, consistent with the depression applied by the device, but this pressure drop should ideally persist in the downstream vessels of the legs (supine subject). Conversely, in the femoral artery, the mean pressure dropped to 41 mmHg, experiencing a reduction of approximately -50 mmHg compared to the baseline configuration, significantly greater than that observed in the preceding vessel.

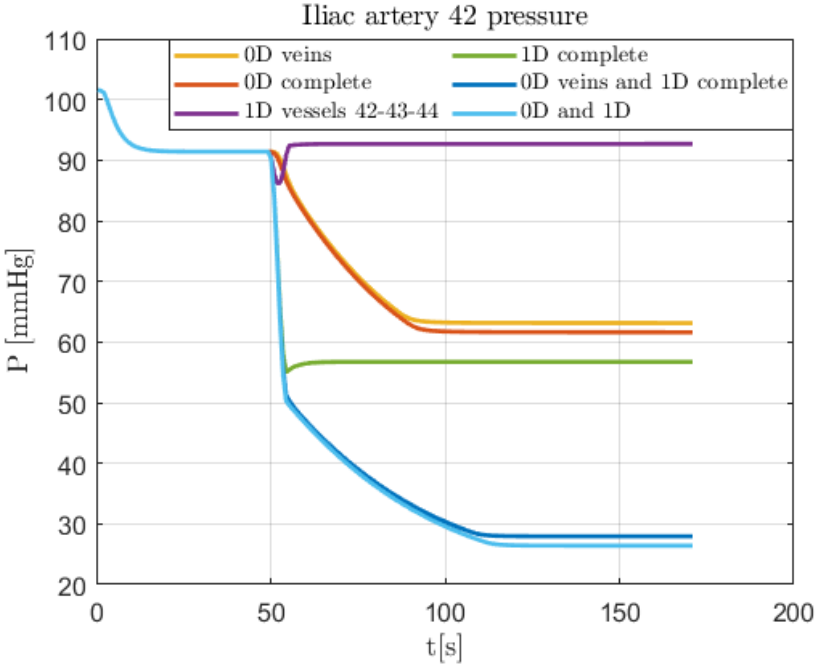

Figure 5.2: Iliac artery 42 pressure.

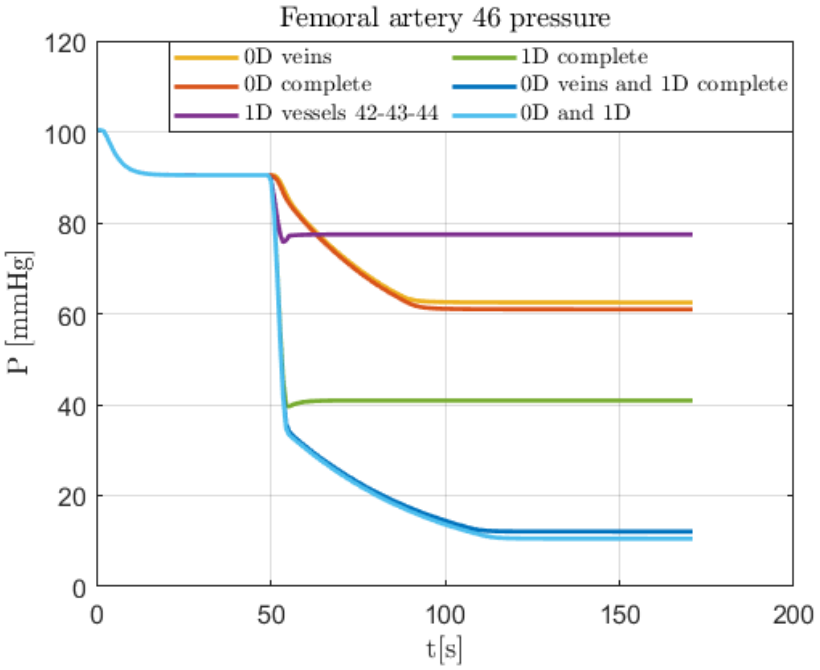

Figure 5.3: Femoral artery 46 pressure.

In the case where LBNP acts only on the common iliac artery and its two daughter vessels (purple curve), the mean pressure decreases by 14% compared to the baseline value, which is considerably less than in the complete 1D simulation. It should be noted that, in this case, the external depression is applied only to vessels 42, 43, and 44, while in the femoral artery 46, the

external pressure goes from the value present at the outlet of vessel 44 (i.e., p_{LBNP}) to zero. Moreover, this spatial gradient extends only along the initial segment of the vessel, resulting in a smaller reduction in intraluminal pressure, likely also influenced by the external depression applied to the upstream vessels.
We can also observe that the curves involving only the 0D model exhibit a more gradual reduction in intraluminal pressure, indicative of the high compliance of venous vessels, which can accommodate large blood volumes with minimal pressure changes, thereby causing a delayed response in pressure variations in 1D vessels like the femoral artery. In contrast, the 1D vessels are characterized by greater stiffness, leading to a more rapid variation in intraluminal pressure in response to changes in external pressure.
Finally, the two most comprehensive cases (blue and light blue curves) experience a substantial reduction in mean pressure (-87%), which appears to result from the combined effects of the 1D and 0D components.
Let us now focus on venous return, specifically on the pressure, volume, and flow dynamics in

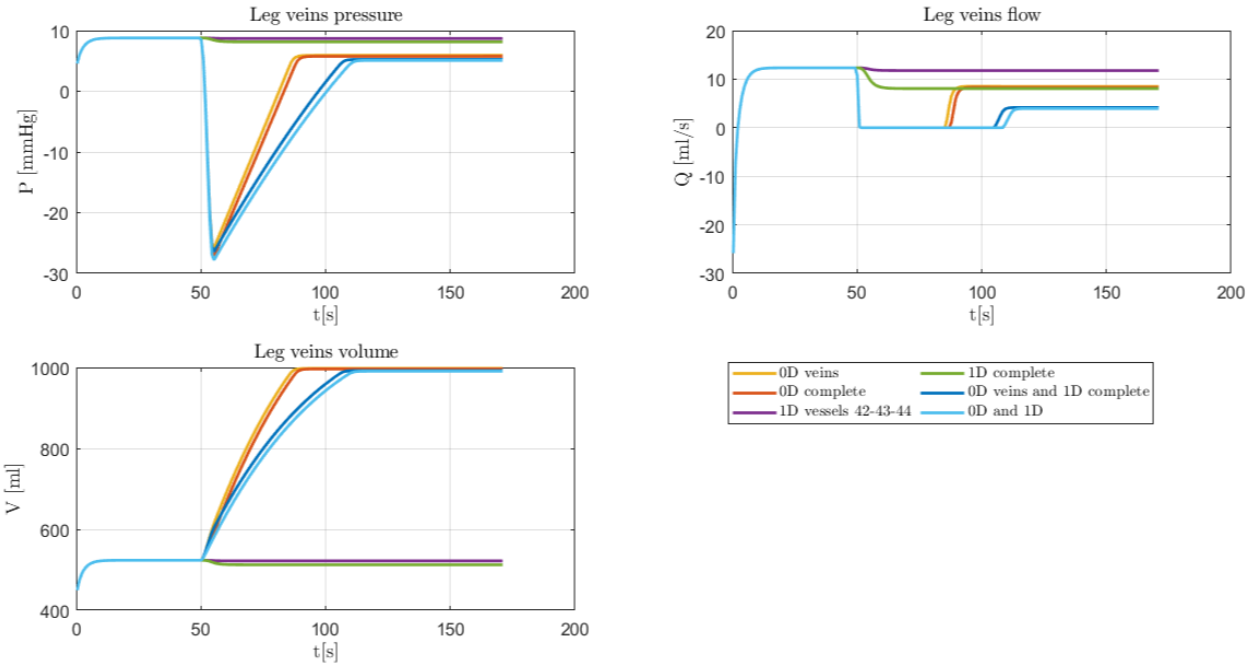

Figure 5.4: Leg veins pressure, flow and volume.

the veins of the legs (Fig. 5.4). Starting from the 0D simulations (yellow and orange curves), we observe that intraluminal pressure decreases from 50 s (the moment of LBNP application), dropping to a value of -27 mmHg, lower than the intraluminal pressure in the abdominal vena cava. Since the model includes valves between the venous compartment of the legs and the abdominal vena cava, and the operation of these regulators is governed by fluid dynamics, driven solely by the pressure gradient across the valve, a lower pressure in the upstream vessel compared to the downstream one results in valve closure to prevent blood backflow. This explains why, once the pressure reaches its minimum, the outflow from the veins ceases and remains zero for a certain period (35 s). During this interval, blood continues to flow within the veins, which

act as reservoirs, but does not exit until the pressure exceeds that in the abdominal vena cava. During this phase, the outflow remains null, the volume increases significantly, and the pressure rises accordingly, following the nonlinear relationship described by Eq. (4.10). Once the pressure becomes higher than that in the abdominal vena cava, the risk of backflow disappears, and the valve reopens: the outflow rises from 0 ml/s to 8.5 ml/s (and remains constant), while the contained volume stops increasing and stabilizes at approximately 1000 ml, a value markedly higher than the pre-LBNP volume (523 ml). This behavior highlights the capacity of the veins to store blood under stress conditions. These dynamics are absent in cases where LBNP is applied only to the 1D portion (whether to vessels 42, 43, and 44, or in a more comprehensive manner), as the pressure reduction in the leg veins is insufficient to cause valve closure.
The two most comprehensive cases (blue and light blue curves) exhibit the same trends observed in the simulations where LBNP is applied to the 0D model. However, the increase in volume and pressure when the valve is closed occurs more gradually, leading to a delayed valve reopening and a reduced outflow rate.

We now reach the end of the systemic circulation, focusing on the right atrium pressure,

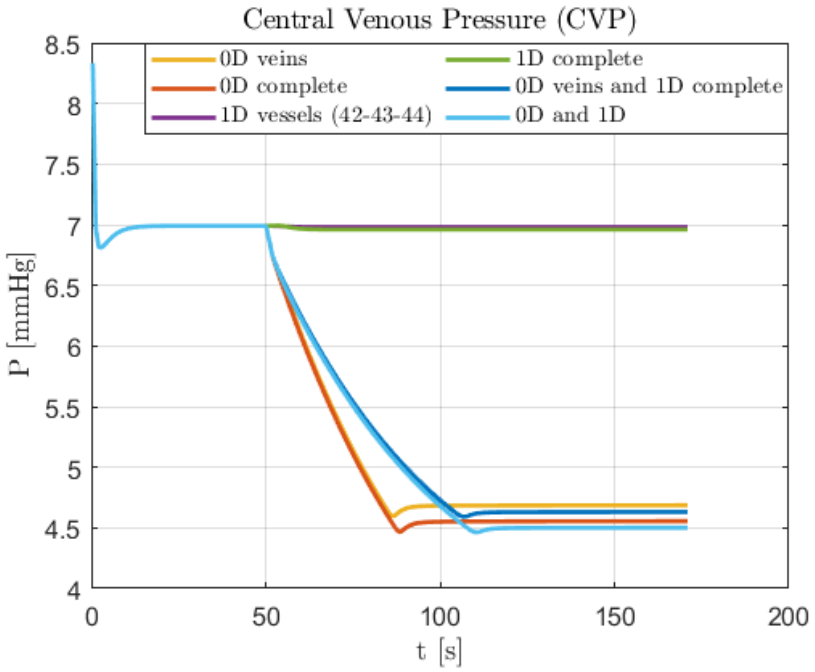

Figure 5.5: Central venous pressure.

i.e. the central venous pressure (CVP) (Fig. 5.5). A reduction in CVP is expected with the application of LBNP, as it induces stress on the lower limbs, discouraging venous return and consequently lowering pressure in the right atrium. If this parameter drops below a certain threshold, cardiopulmonary receptors are triggered. However, the simulations performed so far do not include regulatory mechanisms, so we expect a reduction, more or less pronounced, in CVP without any compensatory responses. It is immediately evident that the application of LBNP to the unidimensional portion has virtually no effect on CVP. As observed in the veins, applying the device solely to the unidimensional model does not significantly inhibit venous return and, therefore, does not lower pressure in the right atrium. In contrast, when the device

is applied to the 0D portion, the accumulation of blood in the lower limbs and the reduction in flow result in a 33% decrease in CVP.

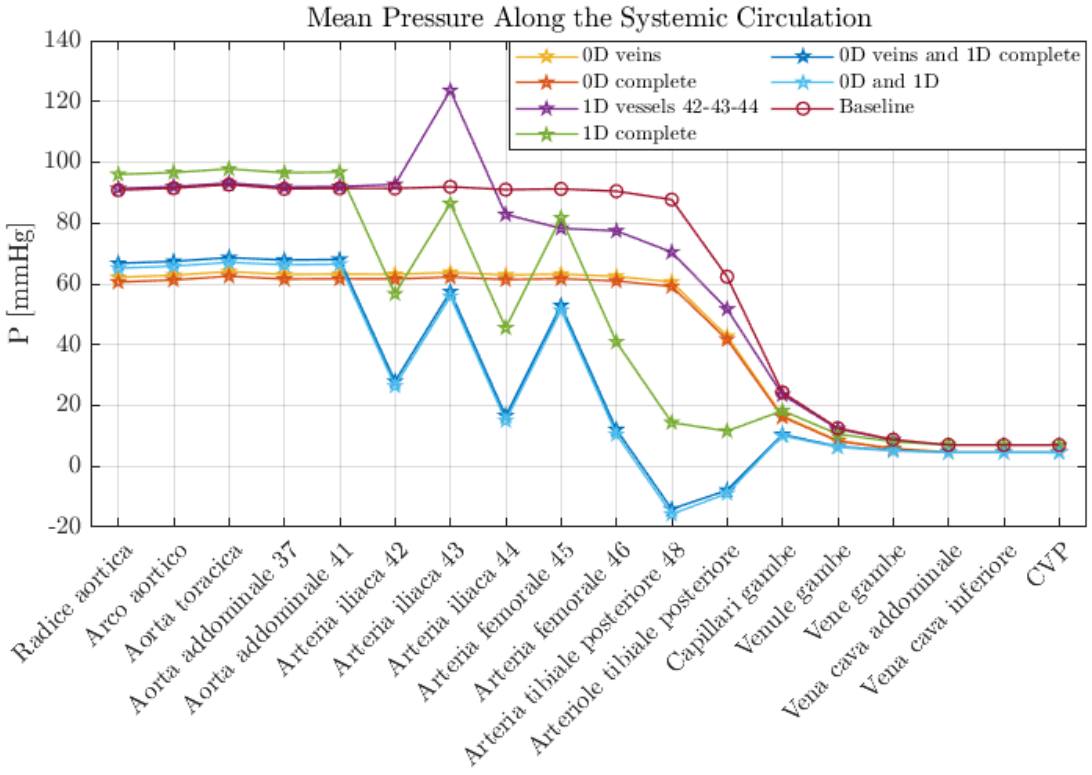

Figure 5.6: Mean pressure along the systemic circulation.

Let us now examine the average intraluminal pressures at key sites along the systemic circulation of the lower limbs (Fig. 5.6). We compare the results obtained from six simulations, at the end of the transient phase following the device application, with the baseline configuration, in which the subject is in supine position and no LBNP is applied. In this latter case, the mean arterial pressure (91 mmHg) is maintained across all 1D arteries due to the absence of a hydrostatic gradient in the supine position. The high resistance of the arterioles causes a significant pressure drop to 63 mmHg at the arterioles and 25 mmHg at the capillaries. Moving to the venous return, we observe very low pressures (below 10 mmHg), while still maintaining a gradient between successive sections, sufficient to ensure positive blood flow and prevent reflux.

In cases where LBNP is applied only to the zero-dimensional compartments (yellow and orange curve), the mean arterial pressure remains constant, consistent with the subject being in a supine position, but is significantly reduced (-33%) compared to the baseline case due to the LBNP application and the deactivation of regulatory mechanisms. Additionally, since in these simulations the external suction induced by the device is applied only to the 0D compartments there is no variation in intravascular pressure along the 1D vessels of the legs, and the same pressure value is maintained down to the tibial artery. At the arterioles, there is a consistent reduction in mean pressure due to their high resistance. Pressure values in the venous return (venules, veins, and vena cava) are reduced compared to the baseline, indicating that in these numerical simulations, the LBNP actually affects these compartments.

Next, we consider the numerical test where the device is applied to the entire arterial tree of the legs (green curve). This scenario shows a slight increase in central arterial pressure (6%) compared to baseline values, contrary to expectations given that regulatory mechanisms are disabled. A substantial pressure drop is observed (from 97 mmHg to 57 mmHg) from the abdominal aorta to the common iliac artery, consistent with the application of $p_{LBNP} = -40$ mmHg starting from this vessel. Since the subject is supine and the device acts on all 1D vessels, this pressure value (57 mmHg) is expected to persist down to the tibial artery. However, a progressive reduction in mean pressure is observed along the path toward the extremities. Considering only vessels without 0D terminations (iliac arteries 42 and 44 and femoral artery 46) the mean intraluminal pressure continues to decrease, reaching 12 mmHg in the posterior tibial artery. This is followed by a pressure increase at the capillaries, which then aligns with venous return pressure values, remaining consistent with the baseline scenario (as the device applied only to the 1D domain does not significantly affect venous return).
In addition to the mean pressure reduction along the arterial tree of the legs, another unclear aspect is the mean pressure behavior at interfaces with the 0D compartments. For example, we observe a sharp pressure increase at the iliac artery 43 and the femoral artery 45. This suggests a numerical issue related to the boundary conditions at the interface between the 1D arterial tree model and the 0D terminations. This hypothesis is further supported by the pressure trends in the scenario where LBNP is applied only to iliac arteries 42, 43, and 44 (purple curve). An anomalous pressure increase is observed in artery 43, while in vessel 45, where the external pressure is nonzero only in the proximal segment (transitioning from p_{LBNP} at the outlet of vessel 44 to 0 mmHg), the pressure trend remains nearly constant relative to the upstream value (iliac artery 44). At the outlet of vessel 45, i.e. at the interface with the 0D terminations of the femoral arterioles, the external pressure becomes zero, avoiding the numerical oscillations observed in vessel 43.
The pressure trends in the two most comprehensive cases, where the device is applied to both the 0D and 1D components, result from the combined effects of both domains. In these cases, central arterial pressure (up to the abdominal aorta) is reduced by 26% compared to the baseline but is slightly higher than in the scenarios where LBNP acts only on the 0D domain. From the iliac artery to the arterioles, the influence of the 1D domain becomes more pronounced: oscillations related to the interface with the 0D terminations consistently appear, and pressure decreases progressively toward the lower extremities. Intraluminal pressures even reach negative values before rising again and aligning with the capillary and venous return pressures. This peculiar behavior may be attributed to the fact that the pressure at the posterior tibial arterioles is represented, followed by the subsequent capillaries, which are 0D compartments receiving blood from all arteriolar terminations in the legs. Consequently, capillary intraluminal pressure depends not only on the conditions at the tibial level but also on the values in the iliac and femoral arterioles, resulting in higher pressure compared to the tibial arterioles.

5.2 Selection of the numerical strategy

To summarize, six numerical simulations were performed, considering the following configurations:

1. LBNP exclusively applied to the entire zero-dimensional model;

2. LBNP exclusively applied to the entire one-dimensional model;
3. LBNP applied only to a section of the arterial tree in the legs, specifically to the common iliac artery (vessel 42) and its two daughter vessels (vessels 43 and 44);
4. LBNP applied solely to the venous compartment of the zero-dimensional leg model;
5. LBNP applied to the entire arterial tree of the legs (vessels 42, 43, 44, 45, 46, 47, and 48) as well as to all the 0D compartments of the lower limbs (veins, venules, capillaries, and arterioles);
6. LBNP is applied to the entire arterial tree of the legs (vessels 42, 43, 44, 45, 46, 47, and 48) as well as to the 0D venous compartments of the lower limbs.

Having analyzed the results of the various configurations, we now determine which modeling strategy among those presented is the most suitable for implementing Lower Body Negative Pressure within our multiscale cardiovascular system model.
From the analysis of the results, it has emerged that the implementation of LBNP on the one-dimensional portion of the model leads to numerical interface issues with the zero-dimensional terminations. The significant pressure variations observed at the external boundaries persist whether the device is applied solely to the 1D segment or to both the 1D and 0D counterparts, but they disappear when the device acts exclusively on the zero-dimensional compartments.
Furthermore, applying LBNP to all the 1D vessels in the legs resulted in a progressively decreasing intraluminal pressure along the arterial tree as it approaches the feet, despite the subject being in a supine position. This outcome may be attributed to the fact that, in reality, arterial vessel walls possess specific mechanical properties that cause only a fraction of the external pressure to be transmitted internally. However, it remains unclear what proportion of this external pressure is perceived intraluminally. A more extensive investigation would be required to implement such mechanisms in our model, but such detailed analysis falls outside the scope of this thesis.
It is also important to note that as the vessels extend further from the heart toward the extremities, they become increasingly rigid, and compliance decreases. This leads to the effect of LBNP on the large arteries of the lower limbs being significantly attenuated by their high stiffness. Conversely, the 0D compartments (arterioles, venules, and veins) in the legs are characterized by greater compliance and deformability, making them more susceptible to the action of the device. This assertion is also supported by the study conducted by Peterson et al. [22], where, in their multiscale model, the application of the hydrostatic gradient and Lower Body Negative Pressure was limited to the zero-dimensional compartments and excluded the arteries, which were considered too rigid to accommodate significant fluid shift. Specifically, in their analysis, LBNP was applied solely to the venous compartments of the caudal region, as veins, due to their high compliance, are ideal candidates for accommodating large blood volumes during stress phases.
It also emerges that cases where the device is applied to both counterparts (0D and 1D) produce results that are a combination of the two individual tests. Consequently, the issues associated with the one-dimensional component persist.
In light of these considerations and observing that the results of simulations (2) and (4), where the device is applied exclusively to the 0D compartments, are highly similar, demonstrating

good numerical strength, it was decided to proceed by considering the effect of LBNP only on the 0D components, namely, arterioles, capillaries, venules, and veins (test (2)), or solely on the veins (simulation (4)). In particular, even if results of test (2) and (4) are similar, simulation (2) has been considered more coherent and nearer to the real impact of LBNP, since the device is applied to all vessels of the leg. From now on, the numerical strategy adopted in simulation (2) will be used to model the effects of LBNP on the cardiovascular system.
To support this choice, it is worth noting that in literature, for example, in the models [19], [20], and [21] analyzed in Chapter 4.3, the cardiovascular system has been simulated using only zero-dimensional models, therefore LBNP has been implemented on the 0D compartments.

Chapter 6

Model response

After selecting the modeling approach, we proceed to analyze the results obtained under different intensities of Lower Body Negative Pressure (LBNP) application. These data will be compared with values reported in the literature to validate both the model and the numerical strategy adopted. In the second section, the response of the cardiovascular system to LBNP application will be compared with that observed following a Head-Up Tilt (HUT) test. This comparison aims to assess whether the device can be used in microgravity to effectively simulate the fluid distribution in the body when standing on Earth, and thus mitigate the cardiovascular deconditioning experienced by astronauts.

6.1 Results under different levels of LBNP intensity

We analyze the results obtained by applying three different levels of LBNP (-20 mmHg, -40 mmHg and -60 mmHg) to all 0D compartments of the legs in the numerical model. The response both with regulatory mechanisms turned off, highlighting the pure fluid dynamics effects, and with them turned on have been considered. We expect different responses to different LBNP levels, since the stimuli change.

6.1.1 Central hemodynamic parameters

Let us start with the central parameters: in Figure 6.1 Heart Rate (HR), Cardiac Output (CO), Stroke Volume (SV), and Central Venous Pressure (CVP) are shown at different levels of Lower Body Negative Pressure. The results can be observed both with baroreceptors deactivated and activated and are reported in Tab. 6.1.

It should be noted that, as the intensity of the negative pressure exerted on the legs increases, the heart must contend with a migration of blood toward the lower limbs. This results in reduced cardiac filling pressure, reduced left ventricular end-diastolic volume (LVED), and consequently a decrease in stroke volume (SV). The heart now pumps a smaller volume of blood with each beat (reduced SV); therefore, to maintain efficiency, it compensates by increasing heart rate (HR). For this reason, in the configuration with regulatory mechanisms active, there is a 8.6% reduction in SV when $p_{LBNP} = -20$ mmHg compared to the baseline supine configuration. As the intensity of the device increases, SV continues to decrease, albeit at a slower rate, dropping from 76.39 ml to 61.85 ml at $p_{LBNP} = -60$ mmHg. Heart rate increases to

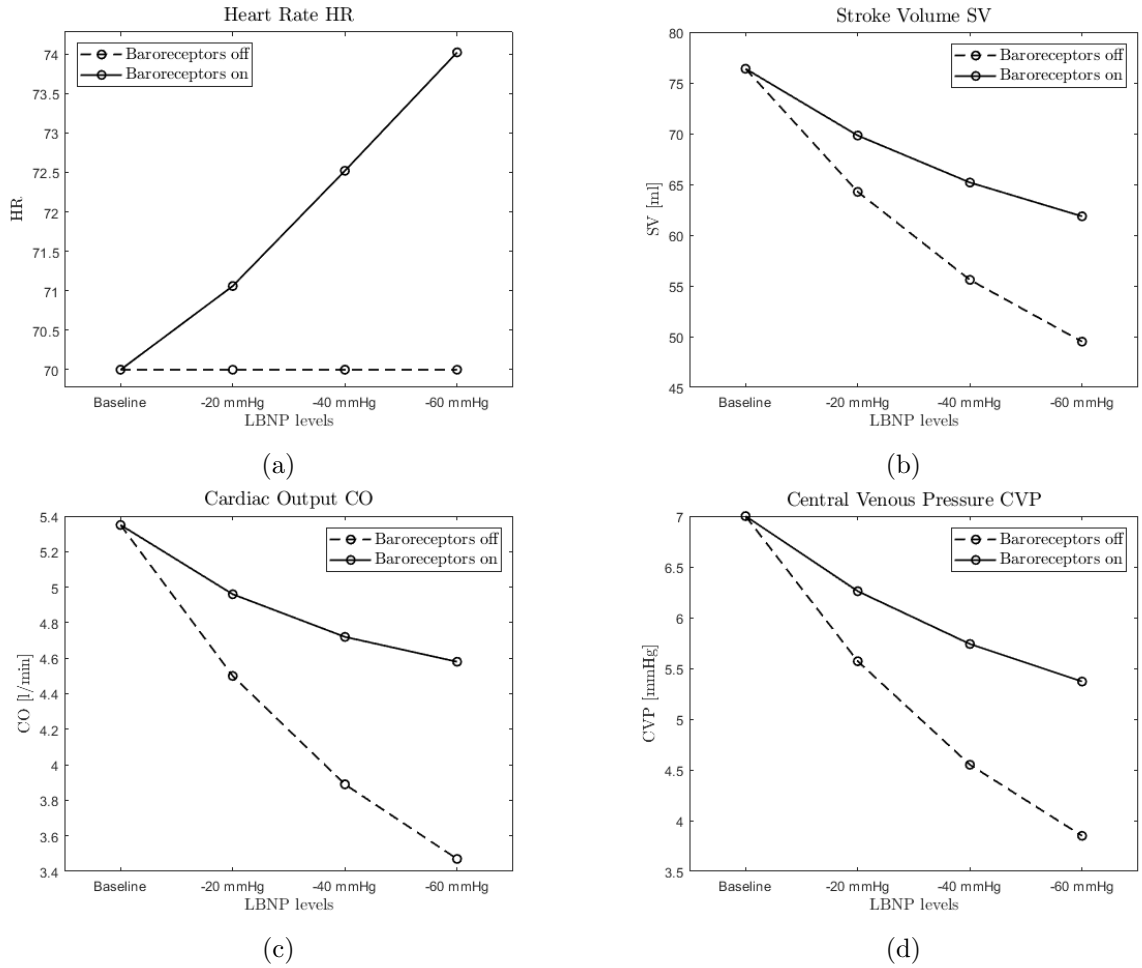

Figure 6.1: Central hemodynamic parameters: heart rate (a), stroke volume (b), cardiac output (c) and central venous pressure (d).

compensate this reduction: over the first 20 mmHg, the increase is minor, while for the two highest levels of Lower Body Negative Pressure, HR rises by approximately 1.5 bpm for every 20 mmHg of negative pressure increase.
Cardiac output (CO), defined as the product of SV and HR, decreases as the intensity of the device increases. This indicates that, despite the increase in heart rate, the heart cannot fully compensate for the reduction in SV caused by Lower Body Negative Pressure, and consequently, the volume of blood pumped by the heart diminishes. In particular, there is a sharper decline (from 5.35 to 4.96 l/min) over the first 20 mmHg of LBNP, during which HR increases less, followed by a more gradual decrease to 4.58 l/min at $p_{LBNP} = -60$ mmHg. These results are confirmed by [23], where an experimental session observed a CO decrease with increasing LBNP intensity, reaching approximately 4 l/min at -60 mmHg of pressure reduction. Although there is no complete overlap in reference values, the decreasing trend and the final values appear to reasonably validate the mathematical model's results with an acceptable degree of uncertainty.
Examining the results obtained with baroreceptors deactivated reveals that the absence of regulatory mechanisms (such as increased peripheral resistance and reduced compliance) causes a

	HR [bpm]	SV [ml]	CO [l/min]	CVP [mmHg]
Baseline	70.00	76.39	5.35	7.00
LBNP -20 mmHg	71.06	69.81	4.96	6.26
LBNP -40 mmHg	72.52	65.18	4.72	5.74
LBNP -60 mmHg	74.02	61.85	4.58	5.37

Table 6.1: Values of HR, SV, CO and CVP with regulatory mechanisms turned on obtained for different levels of Lower Body Negative Pressure.

greater reduction in SV (a loss of 12 ml over the first 20 mmHg of negative pressure, followed by a slower decline at subsequent LBNP levels). This reduction is not offset by any increase in heart rate, ultimately leading to a 1.9 l/min decrease in cardiac output between the baseline configuration and the highest tested level of LBNP.
Thus, it can be observed that the application of the device with regulatory mechanisms deactivated places significant strain on the heart, substantially reducing its efficiency and the amount of blood ejected per beat. Conversely, the activation of baroreceptors mitigates these effects, partially compensating for the reduction in cardiac output and stroke volume. In this context, it is important to note that the use of Lower Body Negative Pressure (LBNP) during a space mission elicits different physiological responses depending on the timing and regularity of its application. If LBNP is used only in the final weeks before reentry, the baroreceptors and cardiopulmonary receptors will have undergone such significant deconditioning that they can no longer adequately compensate for pressure reductions. Consequently, the physiological response may closely resemble that predicted by the present mathematical model under the assumption that regulatory mechanisms are inactive. Conversely, regular use of the device throughout the mission, following a well-structured protocol, can help maintain receptor activity and prevent deconditioning. In this scenario, the body's response would be different and more comparable to the condition where baroreceptors remain functional.
To confirm the observed trends, reference can be made to [24], where a study was conducted on a group of young individuals and a group of elderly individuals to compare their respective responses to the application of different levels of LBNP (-17.5 mmHg, -30 mmHg, and -50 mmHg). Considering the results obtained for the young participants (as the mathematical model is also calibrated for a healthy young individual), it can be observed that, despite the baseline heart rate in the supine position (61.3 bpm) being lower than the value adopted in the mathematical model (70 bpm), heart rate increases with decreasing pressure, reaching values close to those obtained in our study: 67 bpm at -35 mmHg and 75.7 bpm at -50 mmHg. Therefore, although the percentage variations relative to the reference are not directly comparable, a correspondence can still be observed in the growth trend and the values reached.
The Lower Body Negative Pressure operates by causing blood to accumulate in the veins of the lower limbs, thereby discouraging venous return. This effect is reflected in the central venous pressure (CVP), which decreases as the intensity of the Lower Body Negative Pressure increases. It is worth noting that a reduction of CVP below a certain threshold activates regulatory mechanisms induced by cardiopulmonary receptors, such as changes in peripheral

resistance and compliance, aimed at restoring an adequate central venous pressure. In the absence of such regulatory mechanisms, CVP drops significantly with the application of Lower Body Negative Pressure, with a more pronounced decline at the first intensity level (a decrease of 1.4 mmHg for $p_{LBNP} = -20$ mmHg), followed by a more controlled reduction (-1 mmHg between 20 and 40 mmHg of Lower Body Negative Pressure, and finally -0.7 mmHg at the highest level). On average, a reduction of 0.53 mmHg is observed for every 10 mmHg increase in the intensity of Lower Body Negative Pressure.
When the regulatory mechanisms are active, the rate of decline becomes less severe. Peripheral vasoconstriction, reduced vascular tone, and increased heart rate contribute to improving venous return, leading to a smaller reduction in CVP. In this case, CVP decreases by an average of only 0.27 mmHg for every 10 mmHg increase in device intensity, with the most significant drop still occurring at the first intensity level of Lower Body Negative Pressure.
In [24], the recorded reduction in central venous pressure during a test is more pronounced (from 4.8 mmHg in the baseline condition to -0.6 mmHg at a pressure decrease of -50 mmHg) compared to our numerical results. However, in both cases, a steeper decline is observed at the first LBNP level, followed by a more gradual decrease with subsequent increments.
Overall, the growth and decay trends obtained with the present mathematical model for central hemodynamic parameters closely reflect those observed in various experimental tests ([23] [24]). However, the variations obtained relative to the reference values (considering the regulatory mechanisms active) are generally less pronounced than those reported in the literature. Therefore, while we can consider the agreement between our results and the expected outcomes to be fairly satisfactory, further improving the accuracy of the mathematical model could benefit from optimizing the parameters governing the response of baroreceptors and cardiopulmonary receptors, as these two play a key role in triggering the body's reaction to LBNP application.

6.1.2 Systemic circulation hemodynamics

Let us now shift our focus to the lower limbs by examining Fig. 6.2, which illustrates the mean pressure at key sites along the systemic circulation for three different intensity levels of the device, considering both configurations: with baroreceptors active and inactive. We first analyze the case in which the regulatory mechanisms are inactive to assess the purely fluid dynamic effect. It can be observed that the application of increasing negative pressure to the lower limbs leads to a reduction in central pressure, with a more pronounced drop at the first LBNP intensity level (from 91 to 73 mmHg, -19.6%), followed by smaller decrements with the subsequent increases in negative pressure (-12.4 mmHg and -8 mmHg, respectively). Pressure values are maintained up to the arterial level but then decrease at the transition to the arterioles. This behavior clearly deviates from real physiological conditions. In this mathematical model, the external negative pressure induced by LBNP is applied exclusively to the 0D compartments of the legs — namely, arterioles, capillaries, venules, and veins — but not to the arteries. As a result, the mean pressure values in the leg arteries remain equal to those recorded in the central circulation. In contrast, experimental measurements show a pressure reduction starting at the point where the device is applied (iliac region).
Nonetheless, it is important to note that LBNP induces a significant pressure reduction throughout the systemic circulation, particularly at the level of venous return (venules, veins, and venae cavae). The external negative pressure hinders venous return, ultimately leading to a decrease

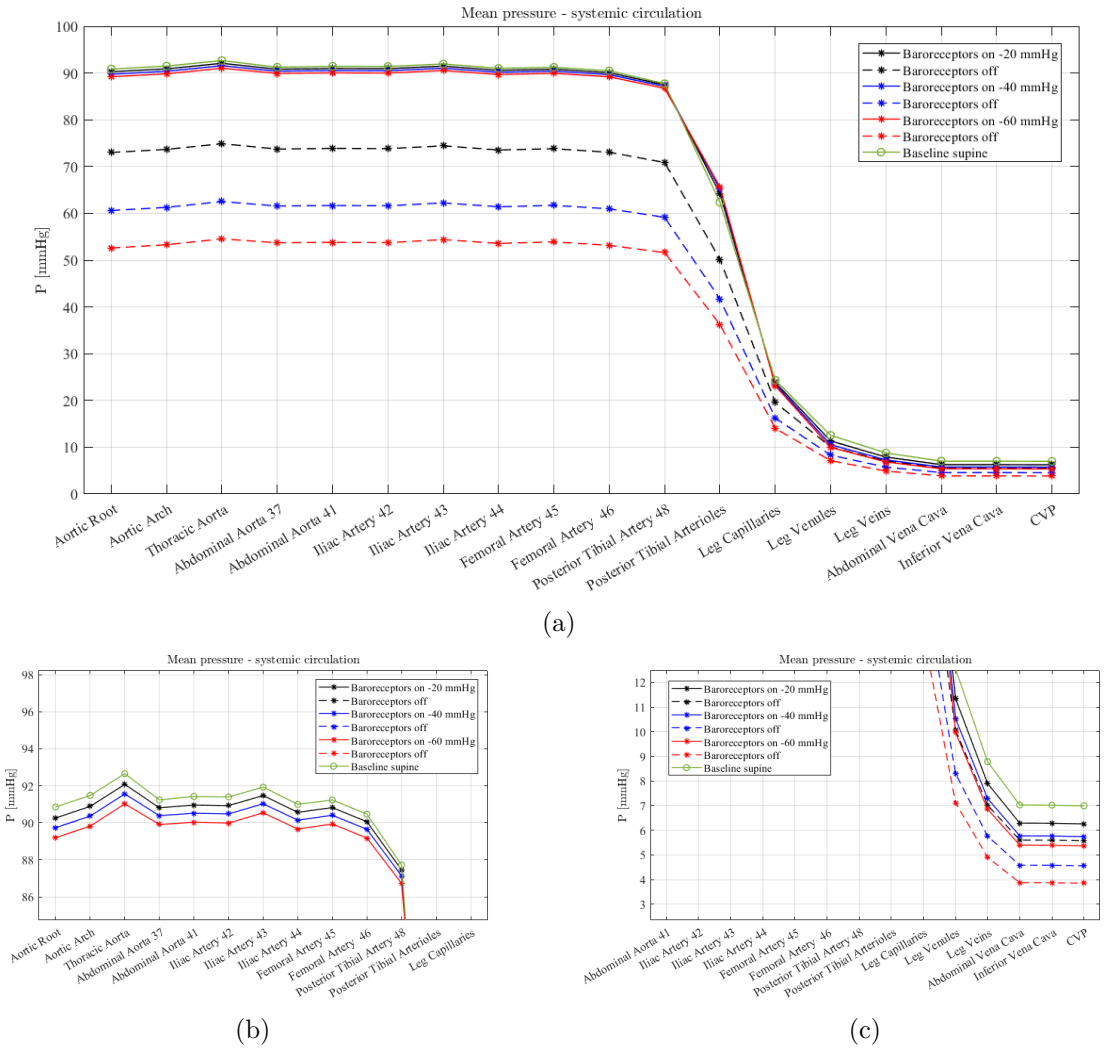

Figure 6.2: Mean pressure along the systemic circulation (a) with zoom on the artery system (b) and zoom on the venous return (c).

in central venous pressure, which in turn triggers the cardiopulmonary reflex response. However, a sufficient pressure gradient is still maintained to ensure proper blood flow direction. Activating the regulatory mechanisms compensates for pressure drops, particularly at the central level, ensuring the maintenance of adequate mean pressure at the aortic arch and carotid sinus, where baroreceptors are located. Meanwhile, venous return still experiences a pressure reduction, albeit less pronounced than in the absence of regulatory mechanisms. Experimental studies [24], [25], and [26], conducted on different groups of individuals, confirm the findings of this model, namely, the maintenance of a stable central mean arterial pressure despite increasing LBNP intensity.
Let us now analyze the details of flow rate and volume in the leg veins as a function of LBNP intensity, as shown in Fig. 6.3. The effect of venous valves is immediately evident from the flow rate diagram. Specifically, starting from the supine condition, activation of the device causes a

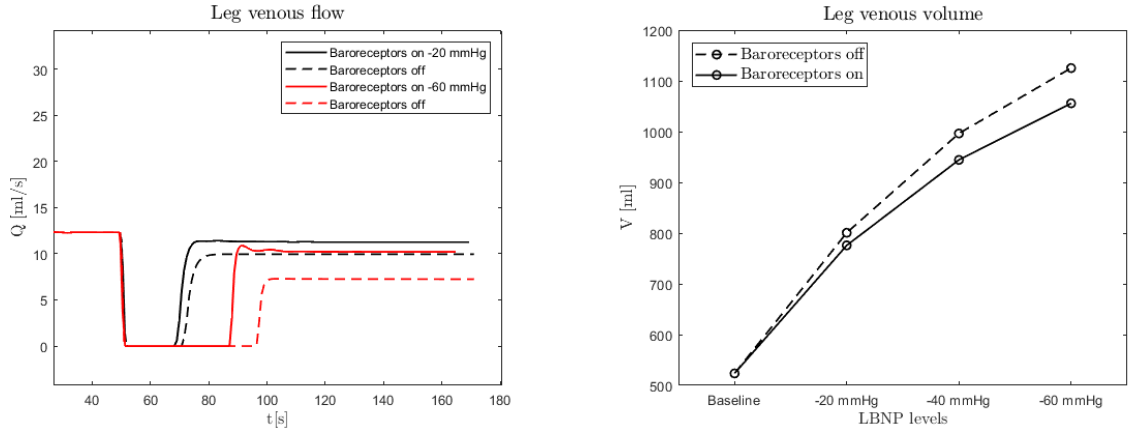

(a) (b)

Figure 6.3: Flow and volume in leg venous compartment.

sudden pressure drop within the leg veins, strong enough to fall below the pressure level in the abdominal vena cava (the subsequent compartment). This leads to valve closure, preventing blood backflow toward the feet. For both LBNP levels reported in Fig. 6.3, we observe an outflow from the veins that drops to zero, only to resume once the internal pressure, having increased due to blood accumulation (with the valve closed), again exceeds the pressure in the abdominal vena cava. This threshold is reached sooner when the induced negative pressure is lower (-20 mmHg) compared to the more intense case. Upon valve reopening, the outflow stabilizes at a lower value than in the supine baseline condition, with a greater reduction at higher LBNP intensities.

The venous volume increases significantly due to valve closure and the subsequent establishment of a lower outflow rate compared to the baseline value. When regulatory mechanisms are inactive, venous compliance remains unchanged, allowing these vessels to accommodate a greater volume of blood (from 523 ml in the baseline condition to 1125 ml at $p_{LBNP} = -60$ mmHg) compared to the case with active mechanisms (1055 ml at $p_{LBNP} = -60$ mmHg). In the latter case, baroreceptors and cardiopulmonary receptors respond by increasing peripheral resistance and reducing compliance, thereby discouraging blood pooling in the veins and promoting venous return.

The review by Goswami et al. [12] presents findings from several experimental studies, all of which report an increase in venous blood volume in the legs of approximately 450 ml at $p_{LBNP} = -40$ mmHg, with a doubling of venous blood volume observed at even higher LBNP levels. Fig. 6.3 shows that the numerically obtained results align well with these experimental trends.

From the diagrams presented so far, it is evident that the most significant variations in the different parameters occur at the first LBNP application level, when $p_{LBNP} = -20$ mmHg. At subsequent levels, the increasing or decreasing trends of the various variables persist, but the rates of change are slightly lower. This suggests that as negative pressure increases, the physiological system is progressively challenged and approaches a limit condition, responding with progressively smaller variations.

We shall now analyze the different responses of venules and capillaries in the legs in terms of

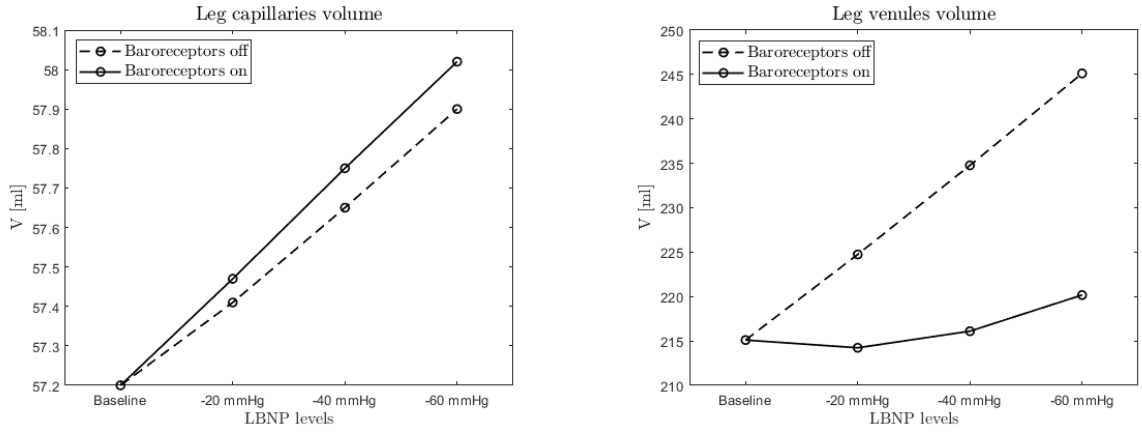

(a) (b)

Figure 6.4: Blood volume in leg capillaries and venules.

blood volume (Fig. 6.4). Capillaries are highly rigid and have minimal musculature, meaning they can only weakly dilate or constrict. As a result, although an increase in volume is observed with higher LBNP intensity, the variation remains extremely limited, ranging from 57.2 to 58 ml in the most stressful condition for the body ($p_{LBNP} = -60$ mmHg with baroreceptors inactive). A significantly different behavior is observed in venules. Due to their high compliance, venules allow substantial volume variations in response to minimal pressure changes. This effect is particularly evident when regulatory mechanisms are inactive: at $p_{LBNP} = -60$ mmHg venous volume exhibits a considerable increase, rising from 215 ml to 245 ml, corresponding to a 14% increase.
Conversely, when regulatory mechanisms are active, the resulting increase in peripheral resistance (vasoconstriction) leads to a smaller volume increase in capillaries and a reduction in venular compliance, promoting venous return. In this case, venules become less distensible, meaning they are less capable of accommodating additional blood without altering their pressure. Consequently, venular volume remains nearly constant up to $p_{LBNP} = -20$ mmHg, after which it begins to increase, albeit much more weakly than in the absence of baroreceptor activation.This phenomenon can be attributed to the fact that the subsequent venous compartment accommodates a large amount of blood (venous volume doubles at $p_{LBNP} = -60$ mmHg). As a result, venules assist the veins in handling this significant fluid accumulation.

6.1.3 Cerebral circulation

Let us now shift our focus to cerebral circulation. Figure 6.5 presents intraocular pressure (IOP), intracranial pressure (ICP), cerebral blood flow (CBF), and the translaminar pressure gradient (IOP - ICP). As discussed in Chapter 2.3, understanding how these variables change with the application of LBNP can be highly beneficial in developing countermeasure protocols to mitigate Spaceflight-Associated Neuro-ocular Syndrome (SANS).
When considering the results obtained with regulatory mechanisms deactivated, it is evident that the fluid shift toward the lower limbs leads to a reduction in cranial blood flow: CBF

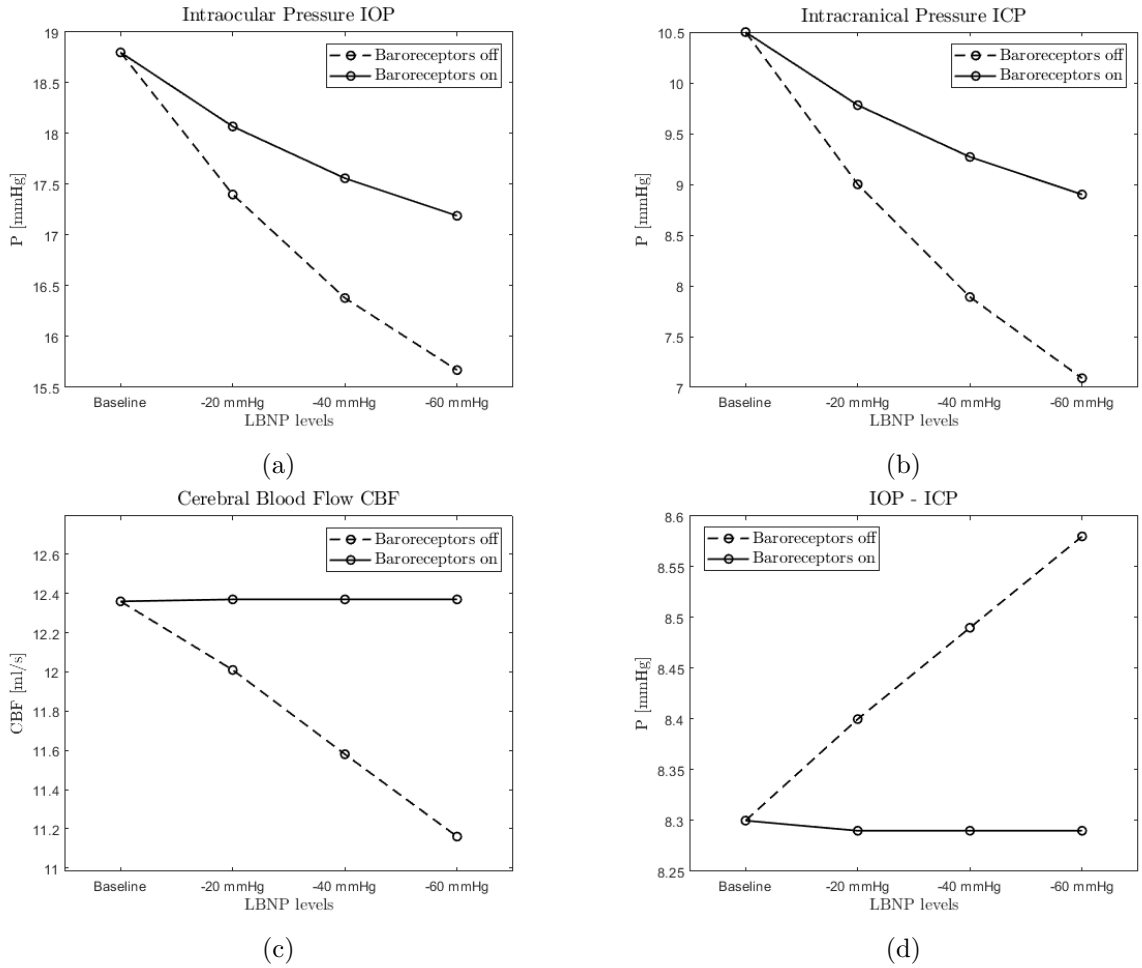

Figure 6.5: Cerebral hemodynamic parameters: intraocular pressure (IOP) (a), intracranical pressure (ICP) (b), cerebral blood flow (CBF) (c) and ocular translaminar pressure (IOP - ICP) (d).

decreases almost linearly from 12.37 ml/s to 11.6 ml/s with a depression of -60 mmHg. This also results in a lower cerebral pressure load, with ICP decreasing from 10.5 mmHg at baseline to 7.1 mmHg at $p_{LBNP} = -60$ mmHg, with the most significant reduction occurring at the first LBNP level. A similar trend is observed for IOP, which decreases from 18.8 mmHg to 15.7 mmHg. However, the translaminar pressure gradient (IOP - ICP) exhibits a notable increase. A study conducted by Harris et al. [9] identified an increase in translaminar pressure as a potential contributing factor to SANS. This increased pressure acts against the lamina cribrosa of the eye, leading to the flattening of the ocular globe. Our results suggest that, in the absence of regulatory mechanisms and considering only the pure hemodynamic effect, the application of increasing LBNP levels would exacerbate this differential pressure. Conversely, the activation of baroreceptors and cardiopulmonary receptors helps maintain the IOP - ICP difference relatively stable, thereby reducing stress on the ocular globe and preventing its deformation.
With regulatory mechanisms active, both ICP and IOP continue to decrease, though to a lesser extent compared to the case where these mechanisms are inactive. Furthermore, cerebral blood

flow (CBF) appears to remain constant when baroreceptors and cardiopulmonary receptors are engaged. While this does not entirely prevent cranial unloading, the reduction in IOP and ICP could still contribute significantly to mitigating SANS. Further research is required in this area, first to deepen our understanding of the underlying causes of this condition and then to refine effective countermeasures and develop appropriate intervention protocols.

6.2 Comparison between LBNP and HUT

Several studies [12] have reported that applying a Lower Body Negative Pressure (LBNP) of $p_{LBNP} = -40$ mmHg to the lower body results in a blood distribution similar to that observed during a Head-Up Tilt (HUT) test. This finding explains why LBNP has been proposed as an effective countermeasure against cardiovascular deconditioning during spaceflight: by shifting blood towards the lower extremities, it stimulates the baroreflex and cardiopulmonary reflex, keeping them active and thereby mitigating the deconditioning experienced by astronauts.
In this section, the cardiovascular response to LBNP ($p_{LBNP} = -40$ mmHg with regulatory mechanisms turned on) will be compared with that observed during an HUT test from 0° to 90° to evaluate whether this technique can effectively simulate, in microgravity, the fluid distribution that occurs when standing on Earth. This assessment aims to determine its potential for mitigating cardiovascular deconditioning in astronauts.

6.2.1 Central hemodynamic parameters

Beginning with the central parameters, Fig. 6.6 reports heart rate (a), stroke volume (b), cardiac output (c) and central venous pressure (d) during an HUT test (blue) and following a LBNP application of $p_{LBNP} = -40$ mmHg, starting from a baseline supine configuration. It is evident that the two responses follow the same trend but exhibit different magnitudes of variation. It would seem that LBNP underestimates the effects of HUT, leading to a weaker change, particularly in HR and CVP, while a better agreement is observed for SV and CO. We recall that CVP is the control parameter for the cardiopulmonary reflex, so a smaller variation in CVP, like that observed during LBNP (from 7 to 5.74 mmHg) leads to smaller variation in venous tone and vascular compliances than those observed during HUT. Remembering that increases/decreases in HR are attributable to variation in the mean aortic-carotid sinus pressure (Chapter 3.3), due to baroreflexes action, the stronger the change in central arterial pressure the higher the variation in HR. Therefore, we can conclude that during HUT the decrease in mean aortic-carotid sinus pressure is more accentuated than that during LBNP application, causing a stronger response in terms of HR. This result does not find strong correspondence in the literature, where it is instead emphasized that applying a negative pressure of 40 mmHg induces an increase in HR similar to that observed during an HUT test.
As mentioned in the previous section, the variations observed with our mathematical model for LBNP slightly underestimate those reported in various studies. To address this issue, a recalibration of the parameters (α, β, and γ) governing the response of the regulatory mechanisms would be necessary, making them more or less sensitive to changes in mean aortic-carotid sinus pressure and CVP. It should also be noted that the negative pressure applied to the lower limbs in our model affects only the arterioles, capillaries, venules, and veins of the legs, exclud-

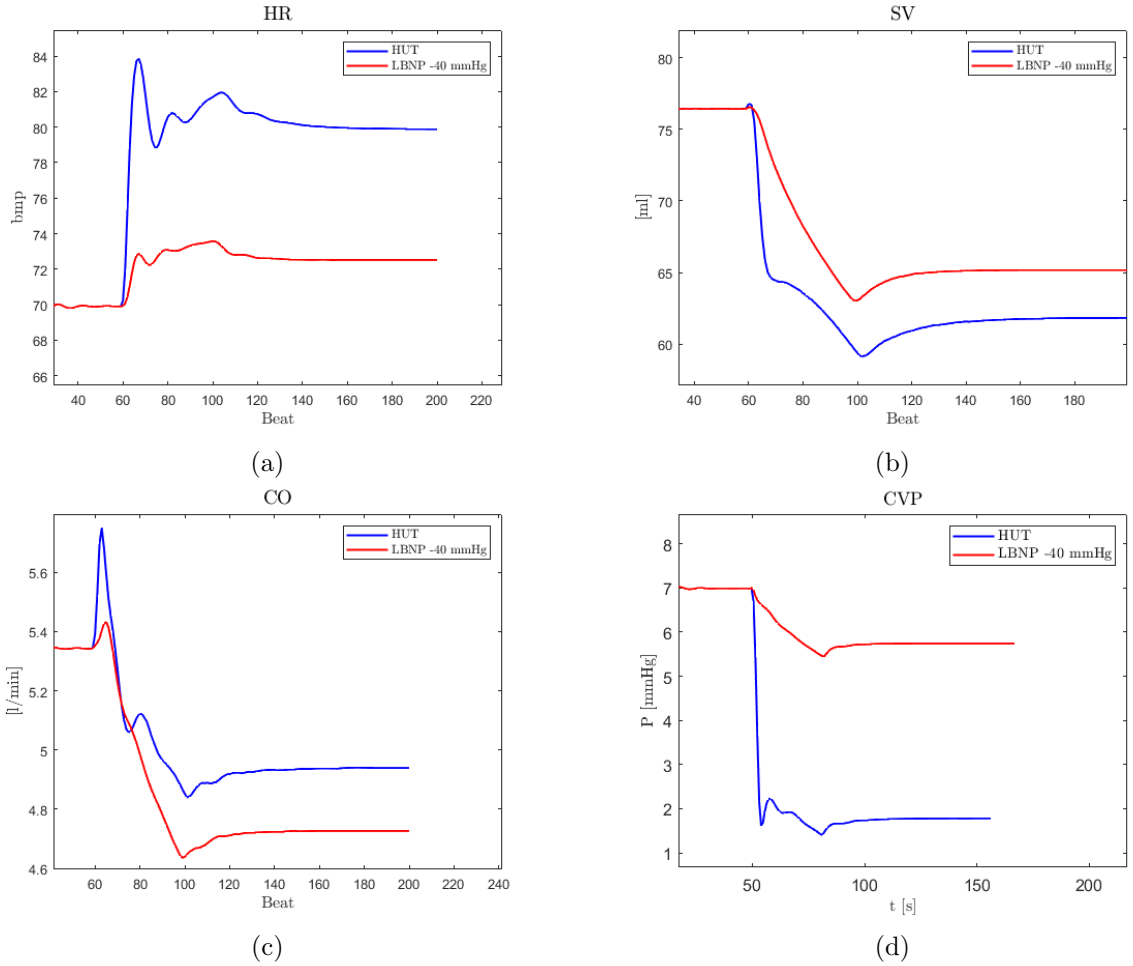

Figure 6.6: Central hemodynamic parameters: heart rate (a), stroke volume (b), cardiac output (c) and central venous pressure (d).

ing the splanchnic region and, consequently, the abdominal vena cava. This choice was made considering that real LBNP devices typically have a sealing joint at the iliac region, leaving the abdomen outside the chamber. However, in the study [27], the negative pressure was also applied to the splanchnic region, leading to stronger physiological responses. This approach could provide a solution to achieve an HR increase more consistent with the values reported in the literature. We will explore this direction and analyze the results in Chapter 6.2.4.

6.2.2 Systemic circulation hemodynamics

Let us now shift our attention to the lower region of the body. Fig. 6.7 presents the mean pressure at key sites along the systemic circulation, highlighting one of the most significant differences between HUT and LBNP—namely, the pattern of the hydrostatic pressure gradient along the body axis. Standing causes a shift of blood toward the legs due to the gravitational effect, leading to a gradual increase in intraluminal pressure that starts in the abdominal region

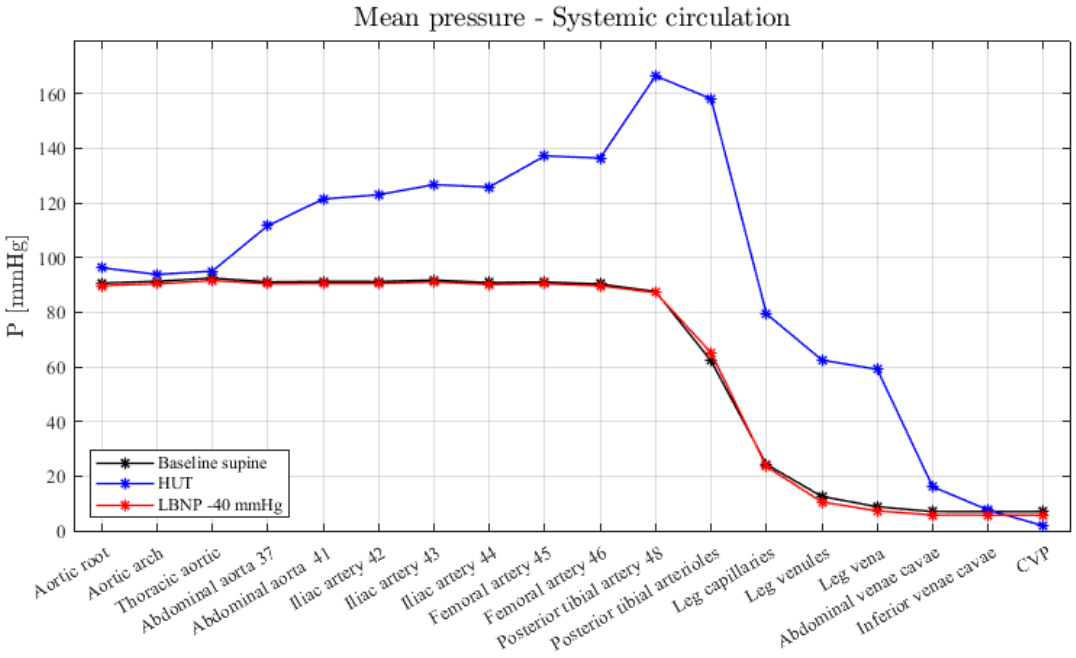

Figure 6.7: Mean pressure along systemic circulation: results of a baseline supine simulation (black), an HUT from 0° to 90° simulation (blue) and a LBNP of $p_{LBNP} = -40$ mmHg simulation (red) have been reported.

and reaches its maximum at the foot level. In contrast, LBNP induces a reduction in intraluminal pressure as a consequence of the decrease in external pressure. This reduction occurs as a single pressure step at the seal area, which in our case is located at the iliac region, and remains constant across all leg sites, as the subject is in a supine position.
Results from our model confirm this behavior only partially. While, in the HUT case, intraluminal pressure progressively increases toward the foot, in the LBNP test, the pressure in the 1D arteries of the legs (iliac, femoral, and tibial) does not decrease until reaching the arterioles, and subsequently, the capillaries, venules, and veins. This is due to the fact that we have considered the effect of the device only on 0D compartments (Chapter 5.2).
Finally, it is important to once again highlight the mismatch in CVP between HUT and LBNP, that leads to different cardiopulmonary reflex stimulation and thus to different venous tone and vascular compliance changes.
In Fig. 6.8, the blood volumes at key 0D sites along the systemic circulation are reported. The most relevant aspect to consider is the agreement between the HUT and LBNP test results: at the arteriolar, capillary, venular, and venous levels, the results confirm the similarity between the two configurations, underling the effectiveness of LBNP in simulating the blood distribution observed when standing on Earth during spaceflight. Fig. 6.9 further supports this conclusion by illustrating the blood volume and flow rate in the leg veins. There appears to be a perfect concordance in both the outflow level from the venous compartment reached after the test and the timing of venous valve reopening. Moreover, in the LBNP test, the increase in leg vein volume closely resembles that observed in the HUT test, highlighting the reservoir function of the leg veins when standing or under the influence of lower body negative pressure. Flow rate

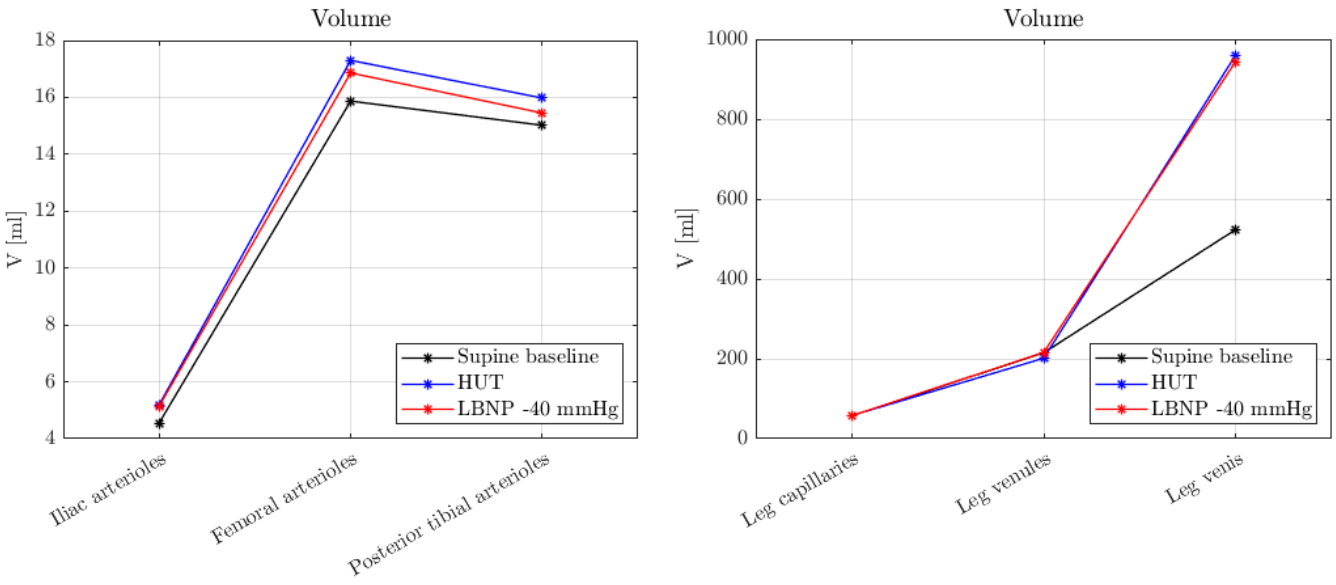

Figure 6.8: Volume along 0D systemic circulation

(Fig 6.10) also shows good agreement between the two conditions: the pooling of blood in the lower region of the body is accompanied by a slight decrease in the outflow rate from the capillary, venular, and venous compartments compared to the baseline supine configuration. This decrease is more pronounced in the case of LBNP, likely due to the constant negative external pressure, which discourages venous return and thus limits the flow rate toward the heart.
At the arteriolar level, a clear trend is not evident. The results from LBNP appear to more closely follow those of the supine baseline posture, showing only a slight decrease, whereas HUT exhibits a lower outflow at the iliac and femoral arterioles, followed by an increase at the posterior tibial arterioles. It appears that as we move toward the extremities (from the iliac to the femoral and then to the tibial arterioles), the two configurations yield progressively closer results in terms of blood outflow (Fig 6.10), while the differences in blood volume become more pronounced (Fig. 6.8). This phenomenon can be explained by considering that, while standing, gravitational force acts gradually across the entire body, creating different pressure gradients at varying distances from the heart. In contrast, LBNP imposes a uniform stress on the lower limbs, from the iliac region to the feet. Therefore, when stating that an LBNP of $p_{LBNP} = -40$ mmHg induces a response similar to passive standing (HUT), it is important to acknowledge that there is likely a specific point where the two responses are most similar. Moving away from this point, an increasing divergence between the two configurations can be observed, since the stress the two test imposed on the body is different.

6.2.3 Cerebral circulation

Let's move to the head region: Fig. 6.11 shows the trend of intracranial pressure (a), intraocular pressure (b), and cerebral blood flow (c) over a cardiac cycle for the baseline supine condition, the HUT maneuver (0° - 90°), and the application of LBNP ($p_{LBNP} = -40$ mmHg), always

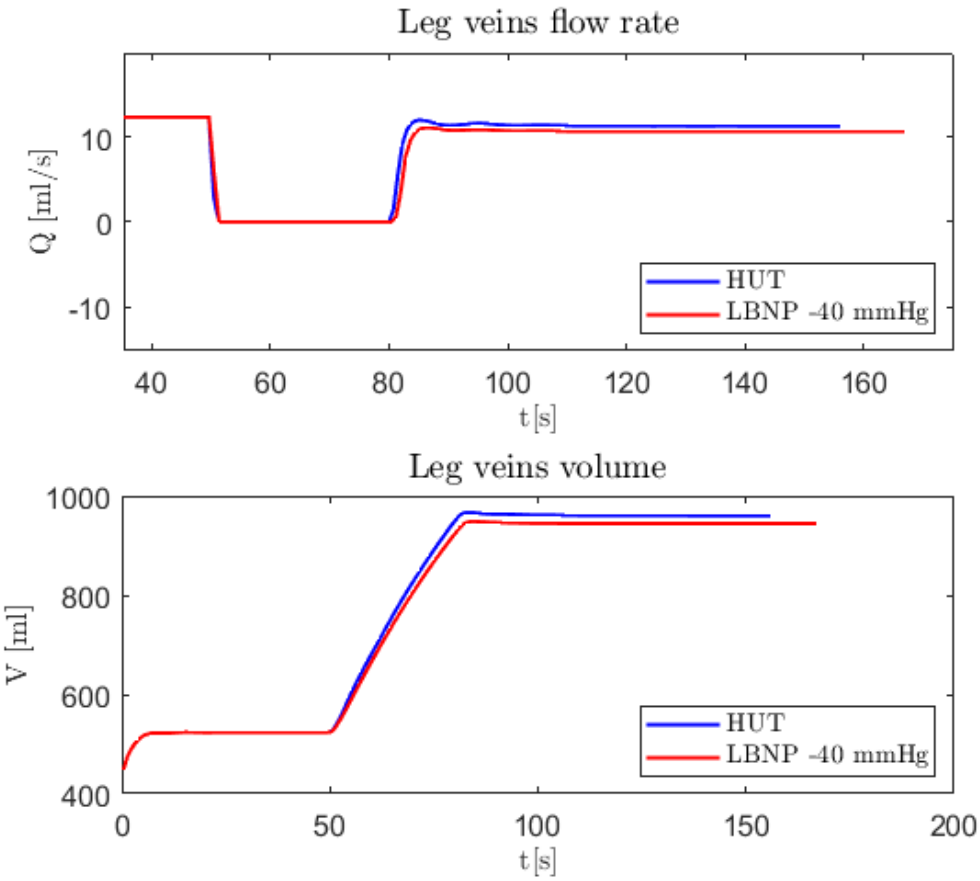

Figure 6.9: Flow and volume in leg veins.

starting from the iliac region. Both the mean values (in bold) and the instantaneous trend are reported. Analyzing ICP and IOP, it is immediately evident that while the application of LBNP leads to a reduction in these pressures, consistent with the variation induced by passive standing (HUT test), the effect is significantly underestimated. Specifically, ICP decreases by 11.7% with LBNP compared to the baseline configuration, whereas HUT results in a reduction of -91%. Similarly, IOP decreases by -6.6% with LBNP and -27.5% with HUT. Regarding the cerebral blood flow (CBF) outflow, the combined action of regulatory mechanisms (baroreceptors, cardiopulmonary receptors, and cerebral autoregulation) ensures that the effect of LBNP remains almost negligible compared to the supine condition. Conversely, standing up reduces CBF by 16%, significantly unloading the cerebral region. This different behavior is likely attributable to the distinct ways in which LBNP and HUT stimulate the body. As previously mentioned, HUT applies a pressure gradient across the entire body (from head to feet) due to gravitational forces, whereas LBNP acts only on the lower body with a constant stimulus. This difference could lead to a reduced physiological response to LBNP compared to HUT.
It is also important to note that in Fig. 6.11, the results for the application of $p_{LBNP} = -40$ mmHg were obtained considering the regulatory mechanisms as active. However, considering that one of the effects of prolonged stay in microgravity on the cardiovascular system is the deconditioning of the receptors responsible for triggering regulatory responses, we can hypothesize

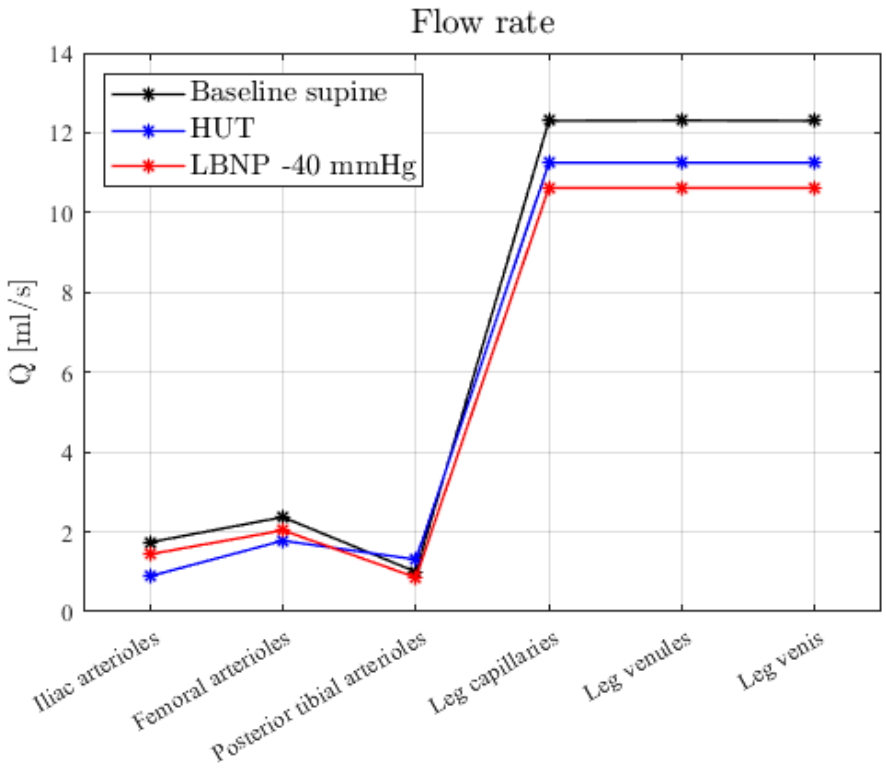

Figure 6.10: Flow rate along 0D systemic circulation: results of a baseline supine simulation (black), an HUT from 0° to 90° simulation (blue) and a LBNP of $p_{LBNP} = -40$ mmHg simulation (red) have been reported.

that applying LBNP only in the final phases of a mission (a few days before return), when these mechanisms are already deactivated, will induce more pronounced reductions in IOP, ICP, and CBF compared to the case reported here. These reductions would likely be closer to the results analyzed in Section 6.1.3, where the outcomes were reported with baroreceptors deactivated. In this scenario, LBNP would still slightly underestimate the effect of passive standing but to a significantly lesser extent than when regulatory mechanisms are active. Based on the results obtained, we expect that if Lower Body Negative Pressure is regularly used during a long-duration mission following a well-structured application protocol, it will periodically stimulate the receptors (as central pressure decreases, triggering their activation), thereby limiting their deconditioning. However, this would also result in a smaller reduction in cerebral load and, as previously discussed, a less effective countermeasure against SANS. Conversely, if LBNP is used only at the end of the mission, when baroreceptors are already deactivated, an opposite condition occurs: on the one hand, there will be greater cardiovascular deconditioning and a higher likelihood of developing orthostatic intolerance upon return, but on the other hand, there will be a greater unloading in terms of pressure and flow in the head region, a positive scenario in order to counteract SANS.

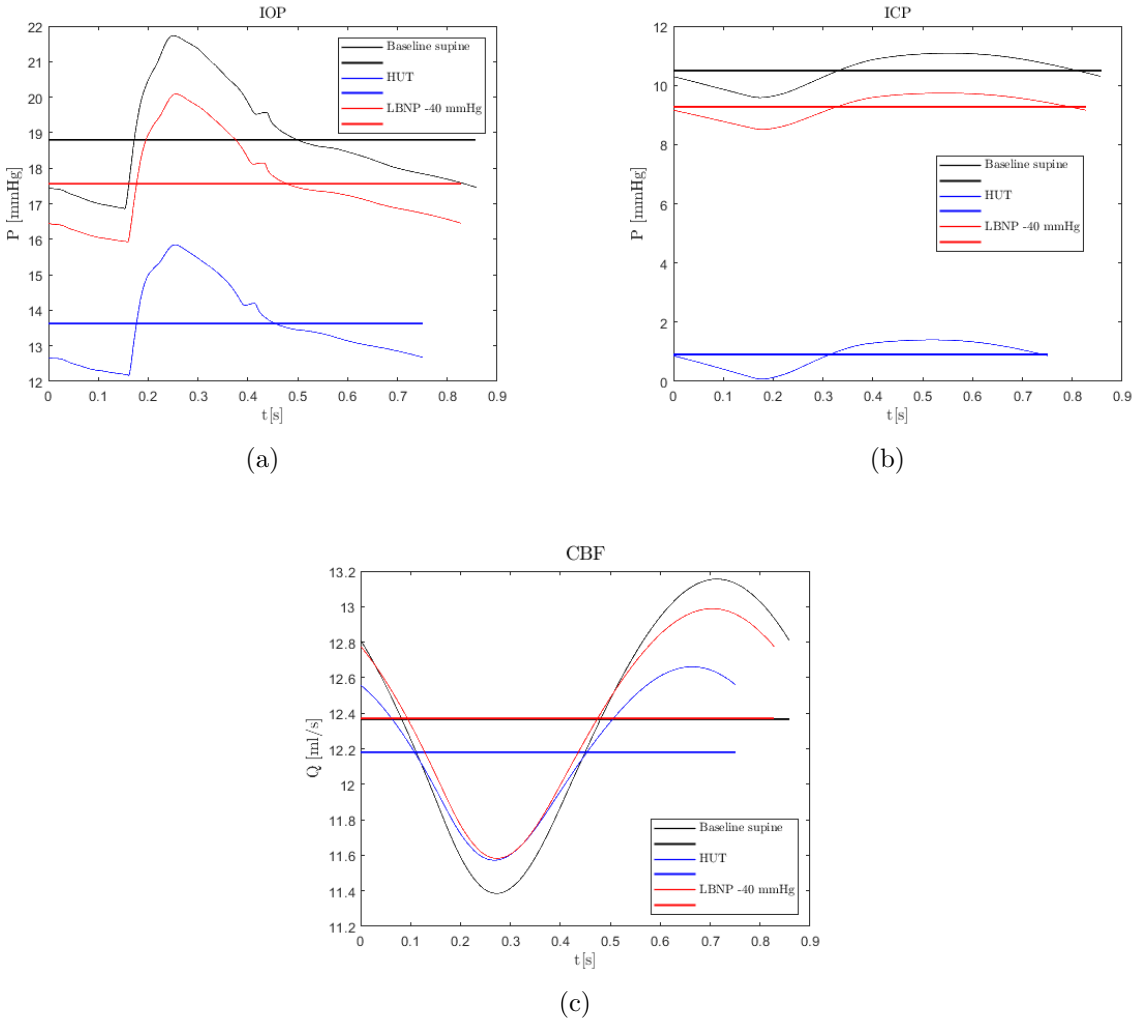

Figure 6.11: Cerebral hemodynamic parameters: intraocular pressure (IOP) (a), intracranical pressure (ICP) (b) and cerebral blood flow (CBF) (c). Instantaneous values and mean value (bold style) on a cardiac cycle are represented.

6.2.4 Discussion

As previously demonstrated, the application of $p_{LBNP} = -40$ mmHg to the lower limbs causes variations in heart rate (HR) and central venous pressure (CVP) in the same direction as those observed after a head-up tilt (HUT) test, though with a smaller magnitude. This underestimation could be mitigated by modifying the parameters of the baroreceptors and cardiopulmonary reflexes, as well as by expanding the area of LBNP application. In this regard, the effect of the device could be considered not only on the arterioles, capillaries, venules, and veins of the legs, but also on the abdominal vena cava. This approach was pursued by [27], in a study where negative pressure was also applied to the splanchnic region, resulting in stronger physiological responses. In light of these considerations, an additional simulation was conducted, incorporating the abdominal vena cava among the sites subjected to external pressure. Figure 6.12 presents the central hemodynamic parameters obtained with this new configuration. It is evident that the inclusion of the abdominal vena cava brings the heart rate (HR) and cen-

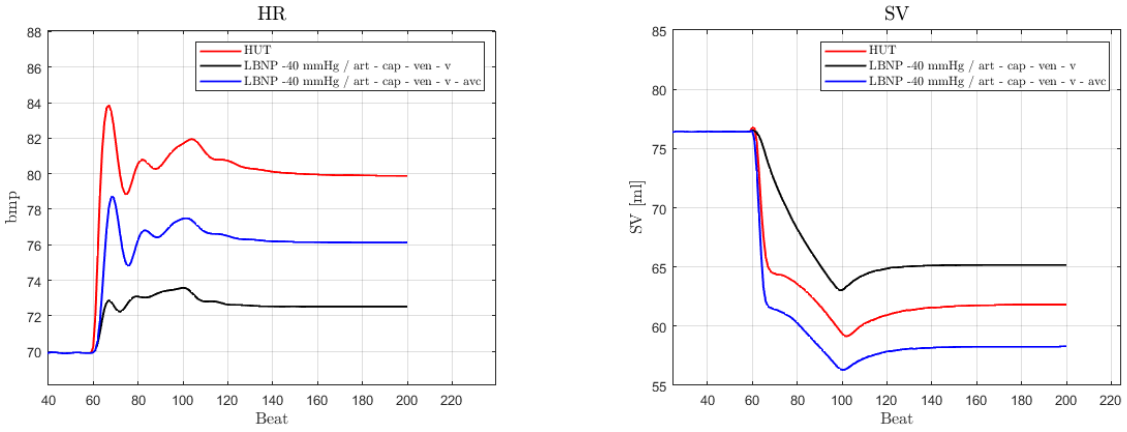

(a) (b)

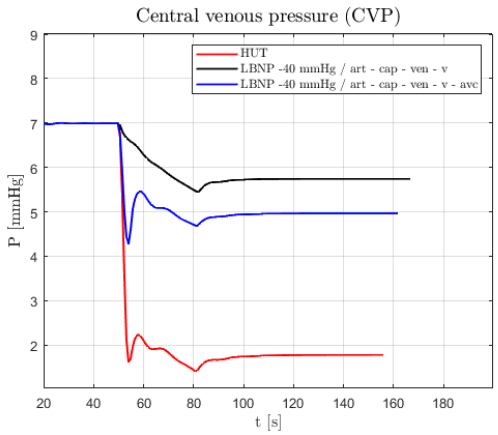

(c)

Figure 6.12: Central hemodynamic parameters: heart rate (HR) (a), stroke volume (SV) (b) and central venous pressure (CVP) (c). Comparison between a Head-Up Tilt (HUT) test, an LBNP test ($p_{LBNP} = -40$ mmHg) with the device applied only to arterioles, capillaries, venules, and leg veins, and an LBNP test ($p_{LBNP} = -40$ mmHg) with the device also applied to the abdominal vena cava.

tral venous pressure (CVP) trends closer to the results of the HUT test simulation, although some underestimation still persists. On the other hand, stroke volume experiences a more pronounced reduction compared to the passive standing case. This response raises questions regarding future improvements to the present model. Further analysis in this direction, perhaps with a combined recalibration of baroreceptor parameters, could help bridge the gap between our model's response and the HUT test configuration.

Conclusions

The present study aims to introduce the effects generated by the application of Lower Body Negative Pressure (LBNP) on the human body within a validated multiscale numerical model of the cardiovascular system. In the preceding chapters, various numerical strategies for simulating these effects were examined, ultimately selecting the most appropriate computational solution. This selection was based on both numerical approaches previously adopted in the literature and the consistency between the obtained numerical results and expected outcomes derived from experiments and tests. After extending the mathematical model to incorporate LBNP, the final part of the analysis assessed the effects of different device intensities on the human body, with a particular focus on variations in central parameters, cerebral circulation, and circulation in the lower limbs. Finally, the study presents a comparison between an LBNP session in the supine position, simulating the device's application in microgravity, and a passive head-up tilt (HUT) test, to determine whether the two conditions trigger similar physiological mechanisms. This comparison aims to evaluate whether the device could effectively be used in microgravity to counteract cardiovascular deconditioning.
The findings presented in the previous chapters can be summarized as follows:

1. Within the present mathematical model, the application of LBNP to the 1D blood vessels of the legs leads to numerical instabilities at the 0D-1D interfaces, as well as a progressive decrease in mean pressure moving toward the lower extremities. This effect, which does not correspond to physiological reality, has been attributed to the specific mechanical properties of the vessel walls and the partial and not yet fully understood transmission of external pressure within the intraluminal space. Future developments of the numerical analysis could focus on a more in-depth investigation of these mechanisms to incorporate them into the model, thereby enabling the application of the device not only to the zero-dimensional part but also to the one-dimensional counterpart;

2. Analyzing the results obtained for different levels of LBNP intensity, it emerged that, at the central level, the model's response follows the expected direction of variation. However, a slight underestimation of these variations was observed, particularly in terms of heart rate (HR). Potential improvements to the model could include further recalibration of baroreceptor parameters to achieve a more pronounced response to the application of the device;

3. By analyzing the results with both active and inactive baroreceptors, two distinct (and almost opposing) frameworks for LBNP application in microgravity have been highlighted. On one hand, the regular and structured use of the device during missions can lead to continuous baroreceptor stimulation, preventing their deactivation and resulting in a

response closer to that observed with active baroreceptors. This approach helps mitigate orthostatic stress upon return to Earth. However, it also limits the reduction of intraocular pressure (IOP), intracranial pressure (ICP), and cerebral blood flow (CBF), elevated levels of which are believed to contribute to Spaceflight Associated Neuro-ocular Syndrome (SANS). On the other hand, using the device intermittently, only in the final phases of missions or when regulatory mechanisms are already deconditioned, does not effectively counteract orthostatic intolerance. However, this approach elicits a stronger cerebral response, leading to greater reductions in pressures and blood flow toward the head, thereby offering a more effective countermeasure against SANS;

4. Regarding the comparison with a passive head-up tilt (HUT) test, it was observed that, due to the different nature of the two stimuli, the two conditions trigger distinct responses in terms of mean pressure at key sites in the lower extremities. However, significant similarities were found between the two configurations in terms of blood flow and venous blood volume, supporting the idea that LBNP can effectively be used in microgravity to simulate the blood distribution observed in the upright position on Earth. At the central level (HR, SV, CO, and CVP) and the cerebral level (IOP, ICP, and CBF), a pressure reduction of -40 mmHg appears to induce variations in the same direction as the HUT test, but of lower magnitude. This results in a weaker activation of baroreceptors and cardiopulmonary receptors and in a less effective countermeasure against SANS. Given that the literature suggests a stronger alignment between central and cerebral parameters following -40 mmHg of LBNP and those observed during HUT, an additional simulation was performed in which LBNP was also applied to the abdominal vena cava. This led to more pronounced variations, although still lower than those induced by HUT. Future analyses could further explore this aspect by combining the effect of including the abdominal vena cava with a recalibration of the regulatory mechanism parameters (α, β e γ) to achieve better agreement with literature-reported values, thereby further validating the model.

These points immediately highlight how the current mathematical modeling of the cardiovascular system serves as a powerful computational tool capable of providing data and variables that are difficult to measure and monitor during a space mission (such as central venous pressure CVP). The numerical integration of the LBNP device within the model represents a valuable opportunity to assess its effectiveness as a countermeasure and to evaluate the optimal combination of activities to mitigate deconditioning, ultimately enabling the development of a well-structured protocol of countermeasures. However, the analysis has also revealed certain challenges in the mathematical implementation of LBNP. These difficulties could be overcome in the future through a better understanding of the physiological mechanisms occurring in microgravity and an increasingly detailed mathematical translation of these mechanisms. In this regard, conducting additional experiments during medium-duration space missions will be essential to fully comprehend the physiological adaptations of the human body in microgravity and to build a comprehensive database of values and parameters. Such a database would facilitate the validation of mathematical models like the present one. These mathematical models play a crucial role in efficiently simulating the physiological changes experienced by astronauts in terms of cost, resources, and time. Ultimately, they pave the way for long-term space missions, preventing the onset of irreversible health conditions.

Appendix

A.1

Geometric features of the 1D arterial tree: l vessel length, D_{in} vessel inlet diameter, D_{out} vessel outlet diameter, h_{wall} vessel wall thickness, γ vessel orientation with respect to the frontal transverse body axis [10].

No.	Artery	l [mm]	D_{in} [mm]	D_{out} [mm]	h_{wall} [mm]	γ [°]	#e
1	Ascending Aorta I	10	29.40	29.30	1.63	-90	2
2	Aortic Arch I	20	24.10	24	1.32	0	4
3	Brachiocephalic Artery	34	19.40	18	0.86	-45	6
4/19	R/L Subclavian Artery I	34	12.90/11	9/8.5	0.67	-30/-45	6
5/15	R/L Common Carotid Artery	94/119	15.10/12.40	7/6	0.63	-90	10
6/20	R/L Vertebral Artery	149/148	4.10/3.80	2.80	0.45	-90	10
7/21	R/L Subclavian II, Axillary & Brachial Arteries	422	8.90/8.40	4.70	0.66	+90	10
8/22	R/L Radial Artery	235	3.70/3.30	3.10/2.80	0.43	+90	10
9/23	R/L Ulnar Artery I	67	3.70/4	3.40/4	0.49	+90	10
10/24	R/L Interosseous Artery	79	2.10/1.80	1.80	0.28	+90	10
11/25	R/L Ulnar Artery II	171	3.20/4.10	2.80/3.70	0.49	+90	10
12/16	R/L Internal Carotid Artery	178	5.70/5	4.30/4.30	0.39	-90	10
13/17	R/L External Carotid Artery	41	5/4.50	4.50/4.30	0.42	-90	6
14	Aortic Arch II	39	22	20.80	1.27	0	8
18	Thoracic Aorta I	52	20	18.90	1.20	+90	10
26	Intercostal Arteries	80	12.60	9.50	1.20	0	10
27	Thoracic Aorta II	104	16.50	12.90	1.16	+90	10
28	Abdominal Aorta I	53	12.20	12.20	1.08	+90	10
29	Celiac Artery I	20	7.80	6.90	0.64	0	4
30	Celiac Artery II	25	5.20	4.90	0.64	0	4
31	Hepatic Artery	66	5.40	4.40	0.49	0	10
32	Gastric Artery	71	3.20	3	0.45	-90	10
33	Splenic Artery	63	4.20	3.90	0.54	0	10
34	Superior Mesenteric Artery	59	7.90	7.10	0.69	+90	10
35	Abdominal Aorta II	20	11.50	11.30	0.8	+90	4
36/38	R/L Renal Artery	32	4.94	4.94/5.2	0.53	0	6
37	Abdominal Aorta III	20	11.20	11.20	0.8	+90	4
39	Abdominal Aorta IV	106	11	11	0.8	+90	10
40	Inferior Mesenteric Artery	50	4.70	3.20	0.43	+90	8
41	Abdominal Aorta V	20	10.80	10.40	0.8	+90	4
42	Common Iliac Artery	59	7.90	7	0.76	+45	10
43	Inner Iliac Artery	50	4	4	0.4	+45	8
44	External Iliac Artery	144	6.40	6.10	0.55	+90	10
45	Deep Femoral Artery	126	4	3.70	0.49	+90	10
46	Femoral Artery	443	5.20	3.80	0.5	+90	10
47	Anterior Tibial Artery	343	2.60	2.30	0.39	+90	10
48	Posterior Tibial Artery	321	3.10	2.80	0.45	+90	10
49	Left Main Coronary Artery	12	4.50	4.50	0.4	0	4
50	Left Anterior Descending Coronary Artery I	18	3.74	3.74	0.4	+60	4
51	Circumflex Coronary Artery I	32	3.60	3.60	0.4	+60	4
52	Marginal Coronary Artery	73	2.52	2.52	0.3	+90	6
53	Circumflex Coronary Artery II	43	3	3	0.2	+90	6
54	Diagonal Coronary Artery	65	2.40	2.40	0.3	+90	6
55	Left Anterior Descending Coronary Artery II	22	3.29	3.29	0.3	+90	6
56	Septal Coronary Artery II	45	2.39	2.39	0.2	0	6
57	Left Anterior Descending Coronary Artery III	100	2.72	2.72	0.3	+90	4
58	Right Coronary Artery I	50	4.05	4.05	0.4	+60	6
59	Acute Marginal Coronary Artery I	34	2.52	2.52	0.3	0	6
60	Right Coronary Artery II	48	3.55	3.55	0.4	+90	6
61	Acute Marginal Coronary Artery II	23	2.11	2.11	0.2	+60	6
62	Right Coronary Artery III (Posterior Descending Artery)	89	3.21	3.21	0.3	+60	8
63	Ascending Aorta II	30	29.3	28.8	1.63	-90	6

A.2

$$
\begin{aligned}
K_1 = Q_*^n - \lambda_2^n A^0 - \lambda_{2,*}^n \left(A_*^n - A_*^0\right) \\
+ \Delta t \Bigg(- \lambda_{1,*}^n \frac{\partial \lambda_{2,*}^n}{\partial x} \left(A_*^n - A_*^0\right) \\
- \left(\sum_{j=1}^{4} \frac{A_*^{j,n}}{\rho} \frac{dB_{j,*}}{dx} - N_{4,*} \frac{Q_*^n}{A_*^n} - A_*^n g^n \sin\gamma \sin\alpha^n \right. \\
\left. - \sum_{j=1}^{4} \frac{A_*^{j,0}}{\rho} \frac{dB_{j,*}}{dx} + N_{4,*} \frac{Q_*^0}{A_*^0} + A_*^0 g^0 \sin\gamma \sin\alpha^0 \right) \Bigg)
\end{aligned}
$$

$$
\begin{aligned}
K_2 = Q_*^n - \lambda_1^n A^0 - \lambda_{1,*}^n \left(A_*^n - A_*^0\right) \\
+ \Delta t \Bigg(- \lambda_{2,*}^n \frac{\partial \lambda_{1,*}^n}{\partial x} \left(A_*^n - A_*^0\right) \\
- \left(\sum_{j=1}^{4} \frac{A_*^{j,n}}{\rho} \frac{dB_{j,*}}{dx} - N_{4,*} \frac{Q_*^n}{A_*^n} - A_*^n g^n \sin\gamma \sin\alpha^n \right. \\
\left. - \sum_{j=1}^{4} \frac{A_*^{j,0}}{\rho} \frac{dB_{j,*}}{dx} + N_{4,*} \frac{Q_*^0}{A_*^0} + A_*^0 g^0 \sin\gamma \sin\alpha^0 \right) \Bigg)
\end{aligned}
$$

where asterisks denote variables taken at the foot of the wave (that is at distance $\lambda \Delta t$ from the considered boundary) at a given time, while superscript 0 refers to the initial condition.

Bibliography

[1] John E. Hall and Michael E. Hall. *Textbook of Medical Physiology, 12th Edition*. Elsevier Health Sciences, 2011. ISBN: 978-1-4160-4574-8.

[2] J. Gordon Betts and P. Desaix. *Anatomy and physiology, 2nd Edition*. XanEdu Publishing Inc, 2022. ISBN: 978-1-711494-06-7.

[3] Bruce M. Koeppen and Bruce A. Stanton. *Berne and levy physiology 7th Edition*. Elsevier Health Sciences, 2018. ISBN: 978-0-323-39394-2.

[4] Peter B. Raven Paul J. Fadel. "Human investigations into the arterial and cardiopulmonary baroreflexes during exercise". In: *Experimental Physiology* 97.1 (2012), pp. 39–50. DOI: 10.1113/expphysiol.2011.057554.

[5] V. Novak Lewis A. Lipsitz. *Primer on the Autonomic Nervous System (Third Edition)*. Academic Press, 2012. ISBN: 978-0-123-86525-0.

[6] H. C. Gunga et al. *Cardiovascular System, Red Blood Cells, and Oxygen Transport in Microgravity*. SpringerBriefs in Space Life Sciences. Springer, 2016. ISBN: 978-3-319-33224-6.

[7] S. Scarsoglio. "Material and slides provided in 'Biofluidodynamics and Space Medicine' couse". In: *Potecnico di Torino* (2023).

[8] M.D. Jay C. Buckey Jr. *Space Physiology*. OXFORD UNIVERSITY PRESS, 2006. ISBN: 13 978-0-19-513725-5.

[9] Lonnie G. Petersen Katie M. Harris and Tobias Weber. "Reviving lower body negative pressure as a countermeasure to prevent pathological vascular and ocular changes in microgravity". In: *npj Microgravity* 6.1 (2020). DOI: 10.1038/s41526-020-00127-3.

[10] Matteo Fois. "Impact of posture and gravity on the cardiovascular system: a validated multiscale modeling approach for ground-based and spaceflight applications". PhD thesis. Politecnico di Torino, 2024.

[11] Caterina Gallo. "A multiscale modelling of the cardiovascular fluid dynamics for clinical and space applications". PhD thesis. Politecnico di Torino, 2021.

[12] Helmut Hinghofer - Szalkay Nandu Goswami Andrew Philip Blaber and Victor A. Convertino. "Lower Body Negative Pressure: physiological effects, applications and implementation". In: *American Physiological Society* 99.1 (2018), pp. 807–851. DOI: 10.1152/physrev.00006.2018.

[13] Hopper NL Balldin UI Krock LP and Squires WG. "Cerebral artery blood flow velocity changes following rapid release of lower body negative pressure". In: *Aviat Space Environ Med* 67 (1996), pp. 19–22.

[14] Akers FM II Coast JR O'Kroy JA and Dahl T. "Effects of lower body pressure changes on pulmonary function". In: *Med Sci Sports Exerc* 30 (1998), pp. 1035–1040. DOI: 10.1097/00005768-199807000-00003.

[15] M. Zaar et al. "Early activation of the coagulation system during lower body negative pressure". In: *Clinical Physiology and Functional Imaging* 29 (2009), pp. 427–430. DOI: 10.1111/j.1475-097X.2009.00890.x.

[16] Eric A. Hall, Richard S. Whittle, and Ana Diaz-Artiles. "Ocular perfusion pressure is not reduced in response to lower body negative pressure". In: *npj Microgravity* 10.1 (2024). DOI: 10.1038/s41526-024-00404-5.

[17] Steven S. et al Marshall-Goebel Karina Laurie. "Assessment of Jugular Venous Blood Flow Stasis and Thrombosis during Spaceflight". In: *American Medical Association* 2.11 (2019). DOI: 10.1001/jamanetworkopen.2019.15011.

[18] A. R. Hargens et al. "Lower body negative pressure to provide load bearing in space". In: *Aviation, Space, and Environmental Medicine* 62.10 (1991), pp. 934–937.

[19] Roger D. Kamm T. Heldt Eun B. Shim and Roger G. Mark. "Computational modeling of cardiovascular response to orthostatic stress". In: *Journal of Applied Physiology* 92.3 (2002), pp. 1239–1254. DOI: 10.1152/japplphysiol.00241.2001.

[20] Yan Zhangb Benjamin Gerbera John-Luke Singhb and William Liouc. "A computer simulation of short-term adaptations of cardiovascular hemodynamics in microgravity". In: *Computers in Biology and Medicine* 102 (2018), pp. 86–94. DOI: 10.1016/j.compbiomed.2018.09.014.

[21] Martin Fink Franz Kappel and Jerry J. Batzel. "Aspects of control of the cardiovascular-respiratory system during orthostatic stress induced by lower body negative pressure". In: *Mathematical Biosciences* 206.2 (2007), pp. 273–308. DOI: 10.1016/j.mbs.2006.03.003.

[22] K. Peterson, Edwin T. Ozawa, and George M. Pantalosand M. Keith Sharp. "Numerical Simulation of the Influence of Gravity and Posture on Cardiac Performance". In: *Annals of Biomedical Engineering* 30.2 (2002), pp. 247–259. DOI: 10.1114/1.1451075.

[23] Convertino Victor A., David A. Ludwig, and William H. Cooke. "Stroke volume and sympathetic responses to lower-body negative pressure reveal new insight into circulatory shock in humans". In: *Autonomic Neuroscience: Basic and Clinical* 111.2 (2004), pp. 127–134. DOI: 10.1016/j.autneu.2004.02.007.

[24] Van Hoeyweghen R. et al. "Cardiovascular response to graded lower body negative pressure in young and elderly man". In: *Experimental Physiology* 86.3 (2001), pp. 427–435. DOI: 10.1113/eph8602153.

[25] Raymond H. et al. "Hemodynamic effects of graded hypovolemia and vasodepressor syncope induced by lower body negative pressure". In: *American Heart Journal* 76.6 (1968), pp. 799–811. DOI: https://doi.org/10.1016/0002-8703(68)90266-4.

[26] H. Lowell Stone C. Gunnar Blomqvist. *Handbook of physiology - Comprehensive Physiology Cardiovascular Adjustments to Gravitational Stress*. Vol. 3. Oxford University Press, 1988. ISBN: 0195206657.

[27] Hao W.Y. et al. "Simulation study of the effects of hypovolaemia on cardiovascular response to orthostatic stress". In: *Medical and Biological Engineering and Computing* 41.1 (2003), pp. 44–51. DOI: 10.1007/BF02343538.